Université de Toulouse

THÈSE

En vue de l'obtention du

DOCTORAT DE L'UNIVERSITÉ DE TOULOUSE

Délivré par :

Institut National Polytechnique de Toulouse (INP Toulouse)

Discipline ou spécialité :

Energétique et Transferts

Présentée et soutenue par :

M. CHRISTOPHE BARBOSA

le mercredi 7 décembre 2016

Titre :

Experimental and numerical study of the interaction of a bubble with an inclined wall

---

Ecole doctorale :

Mécanique, Energétique, Génie civil, Procédés (MEGeP)

Unité de recherche :

Institut de Mécanique des Fluides de Toulouse (I.M.F.T.)

Directeur(s) de Thèse :

M. DOMINIQUE LEGENDRE

M. JOSE ROBERTO ZENIT CAMACHO

Rapporteurs :

M. BENOIT HAUT, ECOLE POLYTECHNIQUE DE BRUXELLES

M. FRANCK PIGEONNEAU, SAINT GOBAIN RECHERCHE

Membre(s) du jury :

M. PASCAL GUIRAUD, INSA TOULOUSE, Président

M. ALFREDO SOLDATI, UNIVERSITE D'UDINE, Membre

M. DOMINIQUE LEGENDRE, INP TOULOUSE, Membre

M. JOSE ROBERTO ZENIT CAMACHO, UNIVERSITE NATIONALE AUTONOME DE MEXICO, Membre

Abstract

The objective of the thesis is to study the interaction of a high-Reynolds moderate-Weber number bubble with an inclined wall. For a given bubble-liquid combination, an increase of the inclination angle results in a transition from a steady sliding motion to periodic bouncing. An experimental device was designed and built to generate the collision of bubbles in terminal state conditions with an inclined wall, with inclination angles ranging from 5° to 80°. Experiments were conducted considering different liquids and bubble diameters. The bubble shape and position were recorded using a high speed camera whereas the wake was captured using a time-resolved Particle Image Velocimetry technique. In addition, the interaction process was also studied using a numerical code.

Considering a force balance on the sliding bubble, that takes into account the viscous or inertial nature of the drag force, the sliding and bouncing motions were well characterised and validated by the experimental results. The inertial sliding and bouncing motions were associated to a constant tangential Froude number. As for the viscous sliding motion, the corresponding drag coefficient was satisfactorily modelled through the additive effects of the potential-flow wall effect and the vorticity production at the wall. Through the same force balance projected along the normal axis, a set of relations were obtained for the transition from sliding to bouncing motions. The wake induced lift force results to be of major importance for the transition criteria.

The different phases that characterize the oblique collision were analyzed. Accordingly, the initial and final times for the process were chosen. On this basis, models for the normal and tangential coefficient of restitutions were proposed and numerically supported. The numerical simulations reproduced the different aspect of the bubble inclined wall interaction.

Keywords— Bubble, Wall, Inclination, Sliding, Bouncing, Coefficient of restitution, Wake

Résumé

Cette thèse a pour objet l'étude de l'interaction d'une bulle à grand nombre de Reynolds et nombre de Weber moyen avec une paroi inclinée. Pour une combinaison bulle-liquide donnée, une augmentation de l'angle d'inclinaison de la paroi entraîne une transition de régime de mouvement de la bulle qui passe d'un régime de glissement à la paroi à un régime de rebonds périodiques. Un dispositif expérimental a été conçu et construit afin de produire la collision entre une bulle en condition d'ascension terminale et une paroi inclinée, l'angle d'inclinaison variant entre 5° et 80°. Des campagnes de mesures ont été menées en utilisant de nombreux liquides et diamètres de bulles. La forme de la bulle de même que sa position ont été enregistrées, durant chaque expérience, avec une caméra rapide alors que le comportement du sillage a été observé grâce à la technique de Particule Image Vélocimétrie (PIV) à haute fréquence. En outre, le processus d'interaction a également été reproduit par simulation numérique.

En utilisant l'équilibre des forces qui caractérise le mouvement de glissement à la paroi de la bulle, prenant en compte la nature visqueuse ou inertielle de la force de frottement, les mouvements de glissement à la paroi et de rebonds périodiques sont bien décrits et sont validés par les résultats expérimentaux. Le régime de glissement inertiel ainsi que le régime de rebond à la paroi sont associés à un nombre de Froude tangentiel constant. En ce qui concerne le régime de glissement visqueux, l'évolution du coefficient de frottement est reproduit de manière satisfaisante en prenant en compte les effets additifs de la présence d'un mur sur les écoulements potentiels et de la production de vorticité au niveau de la paroi. À partir de ce même équilibre des forces mais projeté suivant l'axe normal à la paroi, un ensemble de relations a été établi pour représenter la transition du régime de glissement à la paroi au régime de rebonds. La force de portance induite par les effets du sillage demeure d'importance majeure pour le critère de transition.

Les différentes phases qui caractérisent la collision entre la bulle et la paroi inclinée sont analysées. Des modèles pour le coefficient de restitution normal et le coefficient de restitution tangentiel sont proposés et validés numériquement. Les simulations numériques reproduisent, entre autres, les différents aspects de la physique de l'interaction.

Mots-Clés — Bulle, Paroi, Inclinaison, Glissement, Rebond, Coefficient de restitution, Sillage

Resumen

El objetivo de la tésis fué estudiar la interaccíon entre una burbuja a gran número de Reynolds y número de Weber moderado y una pared inclinada. Considerando una combinación de burbuja y liquido, un incremento del ángulo de inclinación provoca una transición de regimén de movimiento de la burbuja, cambiando de deslizamiento junto a la pared a un rebote periódico. Un dispositivo experimental fué diseñado y construido para generar la colisión entre una burbuja en condición de ascenso terminal y una pared inclinada. El ángulo de inclinación varió entre 5° y 80°. Series de mediciones fueron realizadas usando diferentes líquidos y tamaños de burbujas. La forma de la burbuja y su posición fueron registradas durante cada experimento con una cámara de alta velocidad, mientras que el comportamiento de la estela fué observado mediante la técnica PIV de alta frecuencia. Adicionalmente, el proceso de interacción se estudió también por medio de simulaciones numéricas.

A partir del balance de fuerzas sobre una burbuja que desliza contra una pared, considerando por separando la fuerza de arrastre de naturaleza viscosa y de naturaleza inercial, la dinámica del deslizamiento y de los rebotes periódicos se ha descrito de manera coherente con los resultados experimentales. El régimen de deslizamiento inercial y el régimen de rebote se asocian a un número de Froude tangencial constante. En cuanto al régimen de deslizamiento viscoso, la evaluación del coeficiente de fricción se obtuvo de forma satisfactoria tomando en cuenta los efectos aditivos de la presencia de la pared sobre los flujos potenciales y la producción de vorticidad contra la pared. Considerando el mismo balance de fuerzas proyectado sobre el eje perpendicular a la pared, un conjunto de relaciones fué establecido para la transición de régimen. La fuerza de empuje inducida por los efectos de la estela resultó de mayor importancia para el criterio de transición.

Las diferentes fases que caracterizan el choque entre una burbuja y una pared inclinada fueron analizadas a detalle, gracias a lo cual se obtuvieron módelos para el coeficiente de

restitución normal y el coeficiente de restitución tangencial, los cuales fueron validados por los resultados numéricos. Las simulaciones numéricas reproducen los diferentes aspectos de la física de la interacción.

Palabras Claves— Burbuja, Pared, Inclinación, Deslizamiento, Rebote, Coeficiente de restitución, Estela

Remerciements

Avec aujourd'hui un recul conséquent (que mes tuteurs pourraient logiquement qualifier d'éternel), je suis dans la meilleure position pour remercier à sa juste valeur toutes les personnes qui ont contribué de près ou de loin à la finalisation de cette belle étape de ma vie avec la publication de ce manuscrit.

Il est donc naturel que je commence par remercier mes deux directeurs de thèse, Roberto et Dominique, pour le partage de leur connaissances et de l'amour pour la science de la mécanique des fluides ainsi que pour l'enseignement de l'analyse chirurgicale des phénomènes. Je les remercie également pour leur justesse dans la direction de ma thèse, leur soutien dans la difficulté et leur patience sans limite. Grâce à leur tutorat, j'ai pu développer un savoir faire, une curiosité, une autonomie, une rigueur et une exigence que je n'aurais jamais pu développer autrement. Je vous en suis profondément reconnaissant.

Je remercie spécialement les membres de mon jury de thèse, Pr Pascal Guiraud, Pr Alfredo Soldati, Dr Franck Pigeonneau et Pr Benoit Haut pour avoir apporté des corrections si précises et constructives tant à mon manuscrit qu'à mon projet. J'ai pris un grand plaisir á enrichir mon manuscrit de leurs corrections et commentaires pour finaliser le document le plus abouti qu'il m'ait été donné de produire.

Je tiens également à remercier les membres de mon comité tuteur à l'UNAM, Dr Francisco Javier Solorio Ordaz et Dr Gabriel ascanio Gasca qui par leur suivi et leur critique ont permis d'ajouter leur savoir-faire et leur analyse à mon projet.

Je remercie sincèrement et en premier lieu le CONACYT puis la SRE pour leur soutien économique que ce soit pour la manutention, le matériel, les congrés ou les voyages entre Toulouse et Mexico. Sans aucun doute ce projet n'aurait jamais vu le jour ni atteint les objectifs fixés sans leur contribution, leur soutien et leur générosité.

Dans une même idée, je remercie tous le service administratif du Posgrado de Ciencia e Ingenieria de los Materiales de l'UNAM, particulièrement Dr Heriberto Pfeiffer, Diana Elizabeth Arias Calzadilla, Lic. María Esther Carrillo Espinosa, María Luisa Resendiz Barrera et María

Isabel Gómez Romero pour leur flexibilité, leur accessibilité et leur soutien pour mettre en place et conclure ce projet international pionier qui espérons le sera suivi par d'autres aventuriers.

Je remercie trés chaleureusement l'équipe de Fluid Mechanics and Rheology laboratory où j'ai croisé la route de personnes de grande valeur humaine et académique. J'ai appris à leur côté (Ernest, Dante, Carlos, Lamberto, Paco, Rodrigo, Oscar, Saul, ...) la productivité à travers la solidarité, l'amour de la science, l'accueil chaleureux spécifique à la culture Mexicaine, le respect et tant d'autres valeurs qui m'ont permis de sortir grandi et ouvert de cette aventure. Je remercie principalement Ernesto et Dante pour les leçons de vie et d'humanité qu'ils ont pu inconsciemment m'enseigner. Je ferai en sorte que nos routes se recroisent. De même je suis très reconnaissant envers les membres du groupe INTERFACE de l'IMFT pour m'avoir si bien acueilli pendant mes séjours dans la bonne ambiance. J'ai pu renforcer des liens avec des personnes aussi douées qu'inspiratrices avec René et Esli. Je tire également mon chapeau aux professeurs comme Frédéric Risso, Catherine Colin, Patricia Ern ou Jacques Magnaudet pour avoir su établir des relations amicales et constructives avec les étudiants du groupe. Malgrè mes courts passages à l'IMFT, j'ai apprécié à sa juste valeur l'organisation structurée et le bon fonctionnement du laboratoire.

Je n'oublierai pas non plus de remercier Gérald Debenest et Baptiste Déjean qui, à l'heure de le lancer dans cette folle aventure d'organiser de A à Z la cotutelle internationnale, m'ont guidé et aidé dès le début. Ils font partie intégrante de ce projet.

Je remercie sur une dimension toute autre ma famille, maman, papa, David et Cédric les frérots pour leur soutien inconditionnel dans mes décisions et l'apport innégalable de leur amour. Au même titre, je remercie du fond du coeur, l'accueil et le respect que m'a offert ma famille Mexicaine.

Enfin, Gaby Chula, toi qui a été la seule raison justifiée de cette aventure et de prendre un virage à 90° dans ma vie, il est difficile pour moi d'exprimer en peu de mots l'importance du rôle que tu as joué tout au long de mon doctorat. Parce que tu as toujours été là dans les

moments difficiles et de doute pour me remettre dans le droit chemin au travers de ton amour inconditionnel. Parceque ta force, ta volonté et ton intégrité sont autant de source de motivation que d'admiration depuis que je t'ai rencontré et qu'elles m'ont été particulièrement utile pour ce projet. Parcequ'au delà de mon bonheur et de ma fierté d'avoir accompli ce défi à tes côtés, je me sens honnorés d'avoir pu le conclure en tant qu'époux et maintenant père de nuestra hermosa Meztli. Merci d'être jour après jour ma source d'inspiration et de faire de ma vie ce petit paradis sur terre.

Contents

Chapter 1

Introduction

1.1 Motivation

Multiphase flows are present and are of major importance in a large variety of fields from engineering to medicine. In mineral processes, for instance, a common technique consists in injecting bubbles to carry sulphide particles and extract them from the gangue. The control of the bubble-particle interaction is crucial for this froth flotation mechanism (Zawala et al. (2007), Krasowska and Malysa (2007)). In nuclear engineering, the energy efficiency of a reactor depends strongly on the steam generator performance. Because of the high multiphase flow rates at stake during the production, a precise knowledge of the energy and momentum transfer between the different phases and with the containing walls is required to define the conditions that optimize the cost. Besides these concrete examples, multiphase flow is also present in particle transport in blood, oil extraction, fluidized beds and sewage treatment to mention just a few. Given the large number of existing configurations of multiphase flows, fundamental science can produce realistic models that can be applied to each singular case. This thesis focuses on the interaction of a single bubble with a rigid wall.

To understand the effect of the presence of a wall on the dynamic of a particle, three main lines of investigations have been followed. The first one consists in modelling the collision of

a particle against the wall by a coefficient of restitution $\epsilon = \frac{V_{rebound}}{V_{contact}}$, with $V_{rebound}$ the velocity of the particle after the impact and $V_{contact}$ before the contact. When a spherical solid particle impacts a vertical wall (Joseph et al. (2001)), this parameter depends on the Stokes number ($St = \frac{\rho_s V_{contact} d_{eq}}{9\mu}$). A simple analytical model developed by Barnocky and Davis (1988) provides the correct trend of this dependence for the large variety of experimental conditions considered. In the case of a drop impacting a horizontal wall, a large contact time is considered due to the drop shape deformation (Legendre et al. (2005)). This process is well reproduced by a simple mass-spring model considering a dynamics equation with coefficients corresponding to the physical parameters of the problem. Based on this model, a more appropriate definition of the Stokes number ($St^* = \frac{C_{AM}.\rho.d_{eq}.U_0}{9.\mu}$) is proposed for the case of deformable particles. Through this latest, both solid particles and drops collisions follow the same trend ($\epsilon \sim exp(-\frac{\beta}{St^*_C})$). Finally, ellipsoidal bubbles colliding with a horizontal wall (Zenit and Legendre (2009)) behave differently because the nature of the drainage of the liquid film during the bubble approach is inertial rather than viscous. A revised version of the previous mass-spring system reveals that in this case the coefficient of restitution scales rather as $\epsilon \sim exp\left(-K\,(\frac{Ca}{St})^{1/2}\right)$.

The second line of investigation of the effect of the wall on the particle dynamics also rely on the impact of the particle on the wall but through the increased pressure in the liquid film as the particle approaches the wall. The resulting force applied by this film on the particle is obtained from the lubrication theory and the Laplace equation and introduced in a simple model to resolve the bubble motion. This model fits both the amplitude and the period of the bounces following the collision of a wide variety of drops and high Reynolds and moderate Weber number bubbles with a horizontal (Klaseboer et al. (2001)) and an inclined wall (Podvin et al. (2008)). The theory has also been extended to describe the formation of the three phase contact (Krasowska and Malysa (2007)) for the case of a bubble impacting the wall. Indeed when the contact lasts long enough so the liquid film thickness achieves a critical value the liquid film ruptures and the bubble coalesces with the wall. The rate of

thinning of the liquid film as well as its critical thickness result to depend on the hydrophilic, surface roughness or heterogeneity properties of the solid wall (Jeong and Hyungmin (2015)). As a general rule, the lubrication force provides a good representation of the dynamic of the bubble motion in the direction normal to the wall but fail to represent the tangential motion of the particle when the wall is inclined.

A third line of investigations considers asymptotic expansions of the different forces acting on the bubble with respect to the dimensionless distance between the wall and the bubble are developed. The motion of the bubble in the presence of the wall is then solved. For the low Reynolds case, an adaptation of the Vasseur and Cox (1977) theory is applied to the shear-free boundary condition case. Good approximation of the lift and drag wall induced forces in the Oseen region (Takemura and Magnaudet (2003)) are then obtained. The potential flow theory provides, in turn, the asymptotic expansions (Kok (1993)) of the different forces acting on high Reynolds spherical particles interacting with a vertical wall (Moctezuma et al. (2005)). The same drag coefficient corrections applied to the case of a bubble confined in a channel (Figueroa-Espinoza et al. (2008)) is consistent with experimental data. However this study revealed the leading part of the vortex formed at the wall in the dynamic of the bubble and the necessity to consider it. Finally, Magnaudet et al. (2003) considered the interaction of a drop with both a vertical and horizontal wall when the liquid is at rest at infinity, and when a linear shear flow rate exists. They proposed analytic expressions of the drag, lift and deformations induced by the presence of the wall in the two limit cases of a inviscid bubble and a rigid sphere. Results were assumed valid for a dimensionless distance higher than unity.

Most papers that deal with the interaction of a bubble and a wall are limited to either the vertical or the horizontal cases, leaving the understanding of a bubble colliding with an inclined wall modest. For the case of high Reynolds and low Weber numbers, Tsao and Koch (1997) reported the existence of two behaviors as the bubble can either bounces repeatedly with a constant amplitude and period or slides with a constant velocity. The transition between

these two motions can be obtained by only changing the inclination of the wall. Tsao and Koch (1997) proposed that the transition is related to a single critical Weber number but no explanation of the corresponding physics was proposed. To our knowledge, no experimental study of this phenomenon has been performed with liquids other than water. Regarding the sliding motion of the bubble, Maslyiah et al. (1994) observed the experimental rise velocity of small Weber number bubbles rising along an inclined wall. A good correspondence was obtained with the Hestroni et al. (1997) theory when the channel was vertical. For the inclined case, an empirical relation of the drag coefficient accounting for the modified Eotvos number to take into account the inclination of the wall and the Reynolds number corralated all the experimental data. Aussillous and Quéré (2002) developed scaling laws for the steady velocity of bubbles sliding against a wall. They considered the pancake regime (when the bubble is considerably flattened against the wall because of the action of gravity) as well as the spherical shape regime for which they obtained good results but for a limited range of inclination angle. Podvin et al. (2008) extended the lubrication force model developed by Klaseboer et al. (2001) to take into account the inclination of the wall. Based on the same experimental data as Tsao and Koch (1997), the model showed good results for the bounce amplitude and time-scale. However it failed to generate the tangential velocity variations because of the absence of the lift force in the model. Therefore it could not predict the transition observed experimentally between sliding and bouncing regime. However this transition has been obtained numerically through a level set method (Norman and Miksis (2005)) coupled with a finite difference solution of the Navier-Stokes equations for a bubble rising in a confined channel thanks to a variation of the Bond number, the Reynolds number and the inclination angle.

1.2 Outline

The purpose of the present thesis is to investigate experimentally and numerically the transition of behavior of a high Reynolds and moderate Weber numbers bubbles interacting with an inclined wall following Tsao and Koch (1997) original set up. However, the transition of regime is observed here for an extended range of physical properties, bubble diameters and inclination angles. Based on the experimental results, theories of the different approaches of the problem will be proposed, on one hand, and on the other hand the numerical code will be evaluated in view to produce original results.

The high speed camera and PIV apparatus setup are described in Chapter 2. Through the PIV data, the mutual influence of the bubble and its wake is explored and compared with the De Vries et al. (2002) results. In addition, the numerical code JADIM used to simulate bubble-inclined wall interactions is described in Chapter 3. In Chapter 4 the main differences of behavior between the sliding and the bouncing motions are emphasized. Through their dynamics evolutions as well as wake structures, a first approach of the physics of transition is presented. In Chapter 5, the physical mechanism of the transition is analysed more preciously. Therefore theoretical relations for the transition of behavior are proposed. Based on approaches of the problem developed by Aussillous and Quéré (2002) and Figueroa-Espinoza et al. (2008), the sliding motion is established in Chapter 6. The oblique collision process considering a bubble rising in its terminal state conditions is carried out in Chapter 7. Accordingly, models for the normal and tangential coefficient of restitutions are obtained. Finally, both steady motion and collision of a high Reynolds moderate Weber number bubbles are simulated in conditions equivalent to the experimental conditions with JADIM. Thus the capacity of the code to reproduce the physics of the interaction is evaluated. The main conclusions of the thesis are presented in Chapter 9. As well, the limit of the present thesis and possible orientations for the study of the phenomenon are also detailed.

Chapter 2

Experimental setup

An experimental arrangement, depicted in Figure 2.1, was built to generate single bubbles that interact with an inclined wall in a controlled manner.

Two tanks were built according to the liquid that was used. The heights, widths and lengths of the rectangular glass tanks are respectively 50, 10 and 40 cm for the first tank and 41, 10 and 31 cm for the second one. Within the tank, a glass plate upon which the rising bubble will bounce, is used as upper wall. The experimental setup allows to vary the inclination angle of the wall θ from 5° to 80° by interval of 5° controlled digitally ($\pm 0.1°$). Single air bubbles were generated from the bottom of the tank using a capillary tube and a syringe pump. The injection rate was small enough (3 ml/hour) to consider the liquid at rest when a bubble was released. The lower side of the wall was located far enough from the bottom of the tank (10 cm) so that before the collision happens, the bubble has already reached its terminal terminal velocity, V_{term}, and shape, $\chi_{term} = d_{ma}/d_{mi}$ where d_{ma} and d_{mi} are the major and the minor axis of the bubble. To generate a range of experimental conditions, seven different liquids and two capillary sizes were used. The physical parameters of the corresponding liquid as well as the terminal conditions generated are summarized in Table 2.1. The viscosity and surface tension of the different liquids were measured with a stress controlled (MCR101) Rheometer and a Wilhelmy balance with a DuNouy ring respectively.

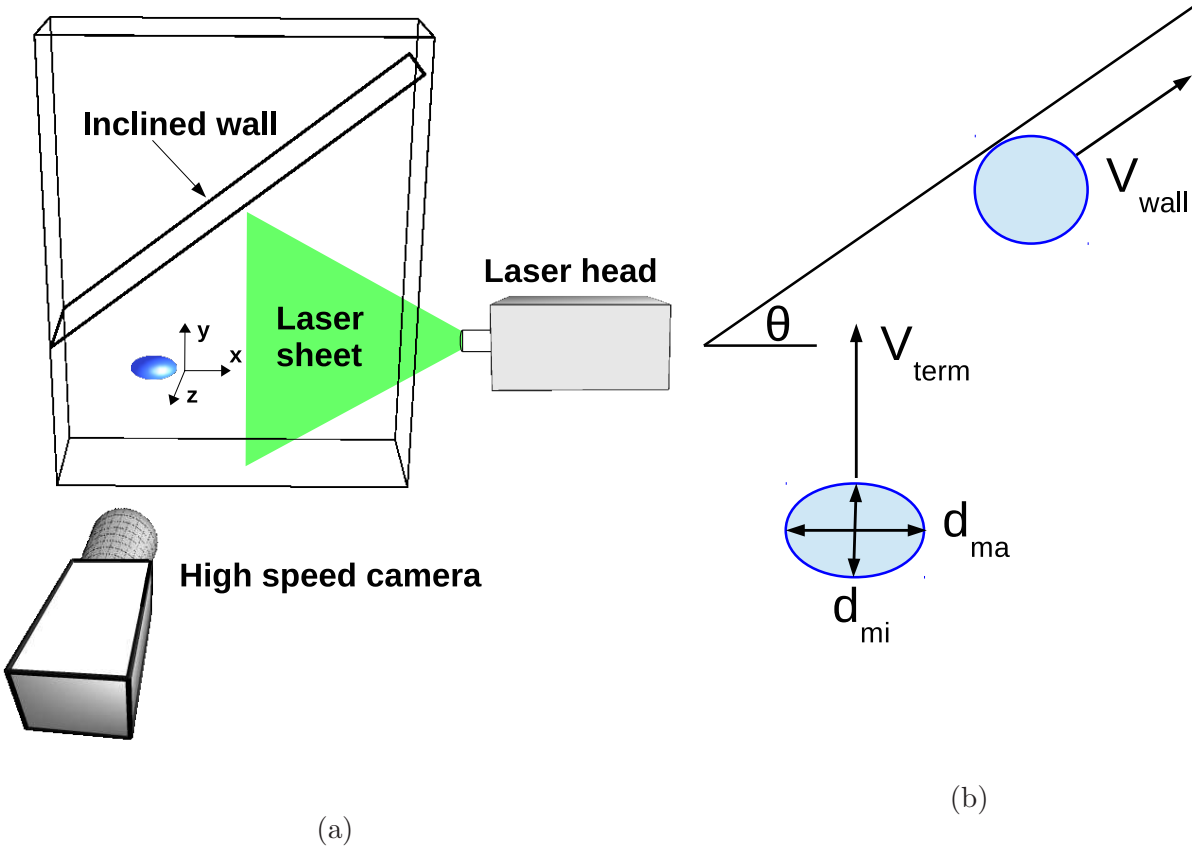

(a) (b)

Figure 2.1: (a) Scheme of the experimental apparatus for the interaction of a rising bubble with an inclined wall; (b) Parameters definition for a bubble rising away from the inclined wall and sliding on it

During the collision process, bubble shape and position were recorded with a high speed camera (Phantom) at a rate of at least 1000 frames per second with a 120 mm Nikkon lens. Given the resolution of the high speed camera (1632 $\times$ 1200 pixels) and a maximum work distance of 4 cm $\times$ 3 cm, a spatial precision of at least 110 $\mu m/$ pixel pitch was obtained. The bubbles were illuminated backwards with a LED panel array. In order to present valid mean and standard deviations values for the results, each experiment was repeated from 5 to 10 times. The dispersion of terminal velocity was always lower than 9%. For simplicity,the results presented in this study corresponds to the corresponding values averaged over the experiments repeated.

The bubble geometric centroid location as well as the wall position were identified for each

frame with MATLAB routines. This bubble center is then considered as the origin of the spherical coordinate system whose axis is the vertical axis. Considering this spherical coordinate system, a Legendre polynomial expansion of the radial position of the interface was processed for each bubble image up to the 20^{th} mode:

$$R(\psi, t) = \sum_{l=0}^{20} b_l(t) P_l(cos(\psi)) \tag{2.1}$$

where P_l represents the Legendre polynomial of degree l and b_l is the amplitude of the l^{th} mode of surface deformation. Considering the orthogonality of the Legendre polynomial, the coefficients b_l are determined with a discrete integration of equation (2.1) multiplied by $P_l(cos(\psi))$ over the interval $[0, \pi]$:

$$b_l(t) = \frac{2l+1}{2} \int_0^{\pi} R(\psi, t) P_l(cos(\psi)) d\psi \tag{2.2}$$

Based on the expression of R, the major axis and minor axis of the bubble are obtained. Assuming a symmetry along the minor axis, the equivalent diameter is then calculated as:

$$D_{eq} = (d_{ma}^2 \, d_{mi})^{1/3}, \tag{2.3}$$

where d_{ma} and d_{mi} are the major and minor axes, respectively.

The two components of the instantaneous velocity in the Cartesian coordinate system are calculated with a central difference scheme:

$$V_i(t) = \frac{x_i(t + n\Delta t) - x_i(t - n\Delta t)}{2n\Delta t}, \tag{2.4}$$

with Δt the time between frames and x_i the i^{th} Cartesian co-ordinates of the bubble center. n, which was 5 in our case, is the number of step times necessary to obtain accurate velocities.

Hence, the magnitude of the instantaneous velocity was obtained as:

$$V(t) = \sqrt{V_x^2(t) + V_y^2(t)} \tag{2.5}$$

We characterize each experiment (a combination of bubble size with the physical parameters of the liquid used) through the terminal Reynolds and Weber numbers:

$$Re_{term} = \frac{\rho V_{term} D_{eq}}{\mu},\ We_{term} = \frac{\rho V_{term}^2 D_{eq}}{\sigma} \tag{2.6}$$

where V_{term} is the velocity achieved by the bubble before colliding with the wall as illustrated in Figure 2.1. μ and σ are the liquid viscosity and surface tension with the air respectively. After the bubble collides with the wall, it experiences few transient bounces and then achieves a new time-average steady state. As reported by Tsao and Koch (1997), the bubble can either slide with a constant velocity or bounce periodically with a constant mean tangential velocity. To characterize this new steady state, wall Reynolds and wall Weber numbers are defined using this mean tangential velocity, V_{wall}:

$$Re_{wall} = \frac{\rho V_{wall} D_{eq}}{\mu},\ We_{wall} = \frac{\rho V_{wall}^2 D_{eq}}{\sigma} \tag{2.7}$$

The range of experimental data is shown in Figure 2.2a and Figure 2.2b where the terminal Reynolds number is plotted as a function of the corresponding terminal Weber number and inclination angle respectively. For all experiments corresponding with a nominal conditions a deviation of the terminal conditions is observed. This variability is the result of the change of the bubble size and contamination of the liquid used. Both acqueous and non-acqueous liquids were considered under ordinary laboratory conditions (not ultra-clean). In both figures, experiments that correspond to a sliding motion (conversely bouncing motion) are plotted with filled symbols (conversely empty symbols). The terminal Reynolds number extends from 100 to 1000 while the Weber number spans roughly from 1.5 to 5. For this range of

Experiment	Composition %	ρ kg/m^3	μ $mPas$	σ mN/m	D_{eq} mm	Re_{term}	We_{term}	χ_{term}	θ_{trans}
E1, ■ (R)	SO 100	855	1.280	18.0	1.1	138±3	1.8±0.05	1.31±0.02	80°
E2, ♦ (R)	SO 100	855	1.280	18.0	1.2	172±8	2.6±0.17	1.32±0.05	80°
E3, ● (O)	SO 100	855	1.280	18.0	2.2	313±7	4.7±0.23	2.06±0.04	45°
E4, ▶ (R)	W-G 80-20	1045	1.555	70.2	1.7	305±7	1.9±0.09	1.26±0.04	70°
E5, ◀ (O)	W-T 99.88-0.12	1001	1.529	61.3	2.8	250±9	2.0±0.11	1.16±0.02	70°
E6, ▲ (O)	W-G 85-15	1033	1.363	70.0	1.6	367±16	2.1±0.16	1.44±0.05	65°
E7, ▼ (O)	W-G 90-10	1021	1.165	70.6	1.6	469±14	2.5±0.15	1.63±0.08	60°
E8, ■ (O)	W-G 95-5	1009	1.038	70.8	1.7	536±21	2.6±0.20	1.58±0.07	60°
E9, ♦ (O)	W-G 90-10	1021	1.165	70.6	2.9	640±77	2.6±0.5	1.69±0.28	50°
E10, ● (O)	W 100	998	0.955	72.6	1.6	601±40	2.7±0.3	1.78±0.10	50°
E11, ★ (O)	W 100	998	0.955	72.6	3.1	955±46	3.6±0.3	1.93±0.13	45°

Table 2.1: Physical properties for all the experiments conducted in this investigation. In all cases, the liquids were mixtures of water (W), glycerol (G) and Tri-ethanol amine (T); percentages in the second column are by weight. Three experiments were performed using Polydimethylsioxane, trimethylsiloxy silicon oil (SO). The type of trajectory for bubbles before reaching the wall is shown on the first column: rectilinear (R) or oscillatory (O).

terminal conditions, bubbles rise freely either rectilinearly or in zig-zag motion.

The velocity field of the flow generated during the wall interaction is obtained using a planar Particle Image Velocimetry system (PIV). The main components of the PIV system are a Nd: YLF Litron laser (527 nm, 10 mJ / 507 Hz), the same high speed camera as the one used for the bubble visualisation and a Dantec PIV software. Given the density of the liquids studied, we used neutrally buoyant silver-coated glass spheres with average-diameter of 10 μm as particle tracers. As depicted in Figure 2.1, the laser sheet illuminates the (x-y) plane containing the bubble center and perpendicular to the inclined wall; the camera is placed perpendicularly with respect to the laser sheet. In this way the path of the bubble is recorded as well as the liquid flow generated by it. The velocity field was obtained by processing adaptive-correlations area of 16 × 16 pixels with a 75 % overlap. Thus a total of 402 × 294 vectors were generated from an area of $42 \times 30\, mm^2$, equivalent to a spatial resolution of 112 μm.

When using the PIV techniques in multiphase flow configurations, new difficulties appear. First, as it is illustrated in Figure 2.3a, the laser plane reflects on the bubble interface. This

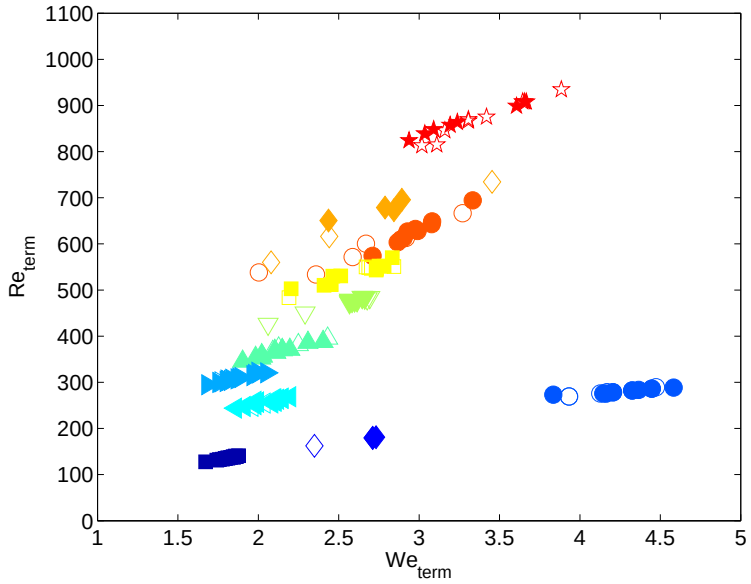

(a)

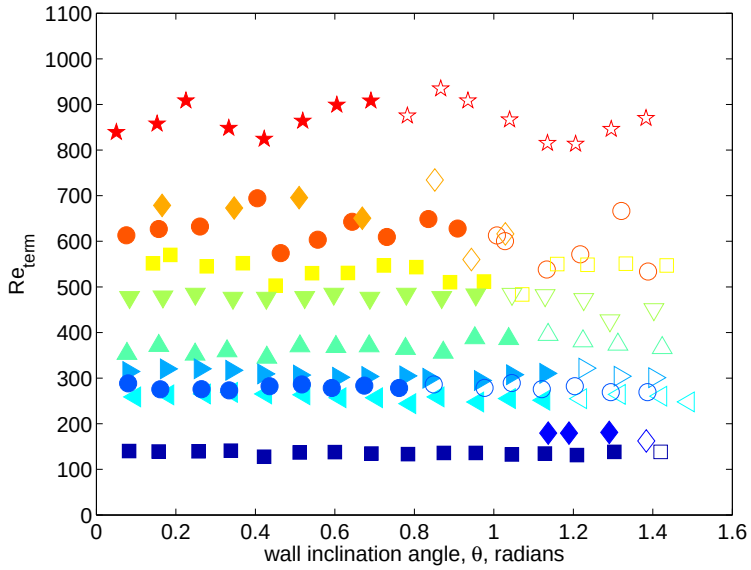

(b)

Figure 2.2: (a) Map of terminal Reynolds, Re_{term}, and Weber, We_{term}, numbers showing all the experiments conducted in this investigation; (b) terminal Reynolds number, Re_{term}, as a function of wall inclination angle, θ. The symbols are according to Table 2.1. In all cases, the filled and empty symbols show the experiments in which sliding or bouncing was observed, respectively.

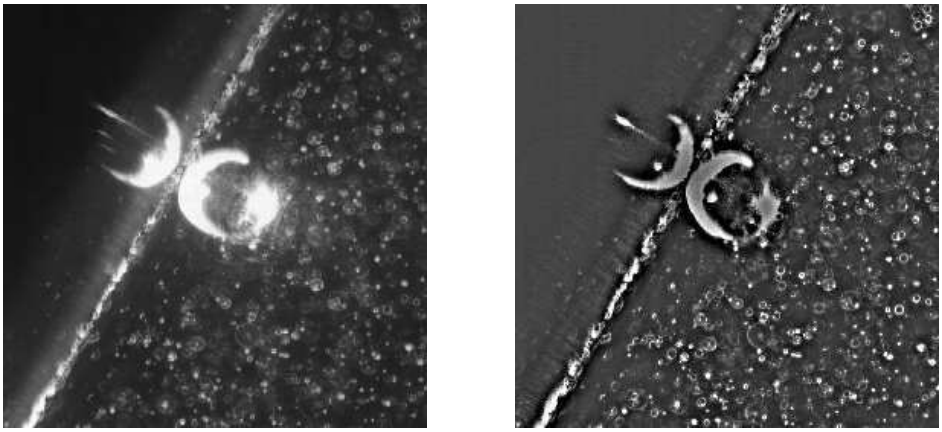

(a) (b)

Figure 2.3: Raw PIV image of the interaction of a 1.6 mm diameter bubble with a 65° inclined wall in water. The present image is a zoom of the original PIV image. The area of both images is the same. The image obtained (a) directly from the PIV technique and (b) with the intensity filter are presented.

reflection alters significantly the image of the flow field around the bubble. The illumination generated by the reflection on the bubble interface is higher than the illumination of the particles in the liquid. Therefore, we used a filter for the light intensity to deal with this limitation. Figure 2.3b shows the PIV images of Figure 2.3a corrected by the intensity filter. Hence the particles present in the liquid are still reflecting the laser light but not the bubble interface. High quality of particle images are then obtained considering the preprocessing of the images. The resulting images are then used to calculate the velocity fields. A second limitation of the PIV technique for the configuration considered here, resulted from the presence of the wall. Because of molecular interactions, particles close to the wall are repelled. As a consequence, the number of particle close to the wall was insufficient to generate precise velocity fields. To overcome this problem, the number of particle was considerably increased.

The high speed camera visualisation technique was used in Chapters 4, 5, 6, 6 , 7 and 8; whereas the PIV technique was used in Chapters 4, 5 and 8.

Chapter 3

Numerical Code

3.1 The JADIM code

3.1.1 Introduction

In the following paragraphs we present the numerical code JADIM, which was used in this work. The code was used to simulate a few cases, which match the experimental conditions. JADIM was initiated by Magnaudet and Rivero (Rivero (1991), Magnaudet et al. (1995)) and is continuously developed at the Institut de Mécanique des Fluides de Toulouse. The code solves Navier-Stokes equations for one-phase and two-phase flows configuration for unsteady as well as steady flows in two or three dimensions. It also offers the possibility to simulate the transport and diffusion of a passive scalar (temperature, concentration) or the dispersion of particles. For two-phase flow configurations, the evolution of the interface separating two or more phases can be simulated by a Lagrangian grid method thanks to an adaptive mesh procedure or by an Eulerian grid method with a fix system of orthogonal curvilinear mesh. In this work, the parallelized Level Set module of the JADIM code developed by Abadie (cf. Abadie et al. (2015)) has been chosen to simulate numerically the collision of a bubble with an inclined wall. Note that no new numerical method has been implemented to the JADIM code in this work. The numerical works consisted in generating a non-uniform Cartesian mesh

system that allowed to reproduce the steady motion of the bubble as well as the collision process with the same dimensionless numbers as in the experimental conditions. As it will be discussed in detail, results can be very sensitive to the grid refinement in the liquid film formed between the bubble and the wall.

First we will briefly describe the main components of the algorithm used in the JADIM code to simulate two-phase flows. Then, we will detail the methodology used to reproduce the interaction and detail the mesh refinement and validation test steps. The first results obtained in the case of the interaction of a bubble with an horizontal wall are presented in the following chapter.

3.1.2 Numerical schemes in JADIM

Spatial discretization

JADIM code is based on a finite volume method for the spatial discretization of the equation. This method consists in dividing the domain in elements of volume V delimited by closed areas S. The Navier-Stokes system of equations considered is:

$$\nabla.(\boldsymbol{V}) = 0 \tag{3.1}$$

$$\rho\frac{\partial(\boldsymbol{V})}{\partial t} + \rho\boldsymbol{V}.\nabla(\boldsymbol{V}) = -\nabla p + \nabla.\tau + \rho\boldsymbol{g} \tag{3.2}$$

with τ the viscous stress tensor, ∂ the partial derivative, ∇ the gradient operator, $\boldsymbol{V}$ the velocity vector, ρ the density, p the pressure field and $\boldsymbol{g}$ the gravity. The Navier-Stokes equations are integrated and discretized over each elementary volume. Volumic terms are taken as constant inside each volume whereas flow terms are taken constant over each face of the closed area S. This method has been chosen because of its good properties of conservation of the equations.

Integration of mass and momentum conservation equations over each elementary volume, is

written in orthogonal curvilinear system of coordinates:

$$\sum_j \int_S V_j n_j \, \mathrm{d}s = 0 \tag{3.3}$$

$$\begin{aligned} \int_V \rho \frac{\partial V_i}{\partial t} \, \mathrm{d}v = - \int_V \frac{\partial p}{\partial \xi_i} \, \mathrm{d}v + \int_S \sum_j (\tau_{ij} - \rho V_i V_j) n_j \, \mathrm{d}s + \int_V F_{ext_i} \, \mathrm{d}v \\ + \int_V \sum_j H_j^i (\rho V_j V_j - \tau_{jj}) - H_i^j (\rho V_j V_i - \tau_{ij}) \mathrm{d}v \end{aligned} \tag{3.4}$$

where ξ_i are the physical coordinates (homogeneous to distances) and H_j^i are the curvature terms as defined by Legendre (1996). They represent the relative variation along the coordinate ξ_j of the metric element calculated along the coordinate ξ_i, also known as curvature factor. And τ_{ij}, the viscous stress tensor, is written as:

$$\tau_{ij} = \mu \left[\frac{\partial V_i}{\partial \xi_j} + \frac{\partial V_j}{\partial \xi_i} - H_j^i \, V_j - H_i^j \, V_i + 2 \, H_i^k \, V_k \, \delta_{ij} \right] \tag{3.5}$$

In order to obtain directly the value of the flow terms and momentum at the edge of the elementary volume without interpolating them, the staggered mesh technique is applied to discretize the equations. With this method, developed by Harlow and Welch (1965), the pressure and more generally all the scalars are defined at the center of the elementary volume whereas the velocity components are defined on two adjacent sides of the volume as illustrated in Figure 3.1. As a consequence, for the non uniform Cartesian coordinate system used in the present study, the volume of integration may be different for each variable. The velocity points are located at the same distance of the two closest pressure points and calculated according to a centered difference schemes. Thanks to this definition, Velocity and pressure gradients as well as the derivatives in the tangential stress are interpolated linearly according to the midpoint rule involving only two points. In turn, the $\frac{\partial V_j}{\partial \xi_i}$ terms are

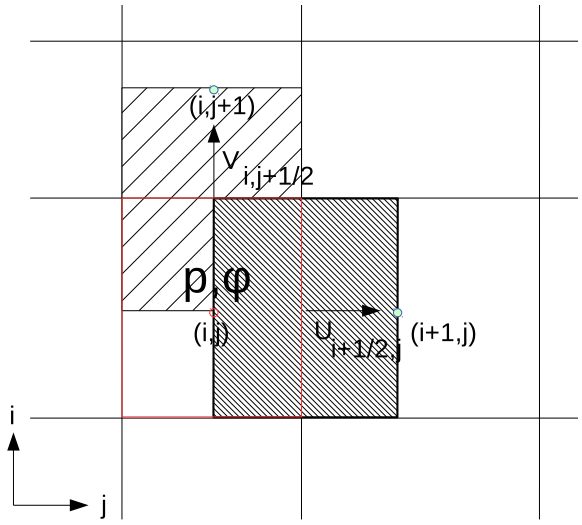

Figure 3.1: Staggered-mesh configuration, with the elementary volume used for the variables p, ϕ, and all the other scalars represented in red; the elementary volume used for the horizontal velocity represented in thin black diagonal stripes; the elementary volume used for the vertical velocity represented in large black diagonal stripes; All the data are then defined considering the coordinates (i,j) of the elementary volume.

interpolated with 4 points so none flow direction is favored and the second order accuracy is satisfied.

Without going into too much detail we illustrate the discretization method for the momentum equation. We define V_p as the volume of integration of the scalars, represented by a red contour in Figure 3.1 while V_u and V_v are the volume of integrations of the velocity components for the momentum equations, represented respectively by broad and narrow stripes in Figure 3.1. The discretized momentum equation for the U component of the velocity V (U,V,W) solved by JADIM in orthogonal curvilinear coordinate system becomes (here in 2D for simplicity):

$$\begin{aligned}\left(\rho\frac{\partial U}{\partial t}\right)_{i+\frac{1}{2},j} V_u + (\rho UUA_u)_{i+1,j} - (\rho UUA_u)_{i,j} + (\rho UVA_v)_{i+\frac{1}{2},j+\frac{1}{2}} - (\rho UVA_v)_{i+\frac{1}{2},j-\frac{1}{2}} \\ - \left\{(\tau_{\xi\xi}A_u)_{i+1,j} - (\tau_{\xi\xi}A_u)_{i,j} + (\tau_{\xi\eta}A_v)_{i+\frac{1}{2},j+\frac{1}{2}} - (\tau_{\xi\eta}A_v)_{i+\frac{1}{2},j-\frac{1}{2}}\right\} = \\ - \left(\frac{\partial P}{\partial \xi}\right)_{i,j} V_u + \left\{H_2^1(\rho VV - \tau_{\eta\eta}) - H_3^1\tau_{\Phi\Phi} - H_1^2(\rho VU - \tau_{\xi\eta})\right\}_{i,j} V_u\end{aligned} \quad (3.6)$$

Where the terms A_u and A_v refer to the value of the edge length in two dimensions (respectively the area in three dimensions) at the considered point whose normal vector is respectively aligned with axis **i** and **j**. The corresponding velocities are interpolated according to the scheme detailed before. For a more detailed explanation of the discretization method, we refer to Magnaudet et al. (1995), Calmet and Magnaudet (1997) and Rivero (1991).

Time advancement of the solution

To clarify the algorithm of resolution in time of the Navier-Stokes equations, we separate the terms of equation (3.3) and equation (3.4) in two families. On one hand, we consider the advection terms, curvilinear terms and the $\nabla_{.(j)}\nu\dfrac{\partial V_j}{\partial \xi_i}$ terms. They are solved explicitly by a three time steps Runge-Kutta scheme. On the other hand, the viscous terms are calculated semi-implicitly by a Crank-Nicholson scheme.

The three time steps Runge-Kutta method provides a third order temporal precision (Δt^3) and a stability conditions given by a CFL number (Courant Friedrichs Lewy) equal to $\sqrt{3}$ Canuto et al. (1988) for the advection terms. As for the semi-implicit Crank-Nicholson scheme, it is characterised by an unconditional stability of the viscous terms as well as a second order temporal precision (Δt^2). Details of both temporal schemes can be found in Calmet (1995). The Runge-Kutta/Crank-Nicholson scheme has been chosen because of its high stability. In addition, this scheme allows to obtain a temporal precision of the second order with a stability condition provided by the following CFL number:

$$CFL = max(\mid U \mid, \mid V \mid)\frac{\Delta t}{\Delta x} \leq \sqrt{3} \tag{3.7}$$

k	1	2	3
Δ_k	8/15 Δt	2/3 Δt	Δt
$\alpha_k = \beta_k$	4/15	1/15	1/6
γ_k	8/15	5/12	3/4
ξ_k	0	-17/60	-5/12

Table 3.1: Values of α_k, β_k, γ_k and ξ_k for the Runge-Kutta / Crank-Nicholson scheme used in JADIM

Accordingly, the velocity fields obtained with the three consecutive time steps Runge-Kutta /Crank-Nicholson scheme are calculated with the discrete equation:

$$\begin{aligned} \frac{V_i^{n,k} - V_i^{n,k-1}}{\Delta t} V_{ol} &= -(\alpha_k + \beta_k)\frac{1}{\rho}\nabla p_i^{n-1/2} V_{ol} \\ +\alpha_k \boldsymbol{L}\left[V_i^{n,k-1}\right] + \beta_k \boldsymbol{N}\left[V_i^{n,k}\right] &+ \gamma_k \boldsymbol{N}\left[V_i^{n,k-1}\right] + \zeta_k \boldsymbol{N}\left[V_i^{n,k-2}\right] \end{aligned} \tag{3.8}$$

Where $k = 1, 2, 3$, $V_i^{n,0} = V_i^n$ and the implicit and explicit operators, respectively $\mathbf{L}$ and $\mathbf{N}$, are expressed by:

$$\boldsymbol{L}(V_i) = \sum_j \frac{1}{\rho}\int_S \mu \frac{\partial V_i}{\partial \xi_j} \mathrm{d}S \tag{3.9}$$

$$\begin{aligned} \boldsymbol{N}(V_i) = \int_{\mathrm{V}} g_i \mathrm{d}v + \sum_j \frac{1}{\rho}\int_{\mathrm{S}} \mu \frac{\partial V_j}{\partial \xi_i} n_j \mathrm{d}S - \sum_j \int_{\mathrm{S}} V_i V_j n_j \mathrm{d}S \\ + \sum_j \frac{1}{\rho}\int_{\mathrm{S}} \mu \left[-H_j^i V_j - H_i^j V_i + 2H_i^k V_k \delta_{ij}\right] n_j \mathrm{d}S \\ + \sum_j \int_{\mathrm{V}} H_j^i (V_j V_j - \tau_{jj}) \mathrm{d}v - \sum_j \int_{\mathrm{V}} H_i^j (V_j V_i - \tau_{ij}) \mathrm{d}v \end{aligned} \tag{3.10}$$

Calmet (1995) determined the value of the coefficients γ_k and ξ_k, in such a way that the advection terms are achieved with a temporal precision of the third order at the time $t^{n+1/2}$. As well the same system of equations for $t^{n+1/2}$ gives the value of the corresponding three step time: $t + 8/15\delta t$, $t + 2/3\delta t$, $t + \delta t$. As for the coefficient α_k and β_k, they arise from of the second order approximation condition of the viscous terms at the time $t^{n+1/2}$ and respecting the semi-implicit scheme of Crank-Nicholson. The coefficients obtained by solving these system of equation are reported in the table 3.1.

The velocity fields obtained at the end of the third step time $V_i^{n,3}$ contains the whole vorticity of the new velocity fields V^{n+1} but is not divergence free. In order to generate a velocity field that satisfy the incompressibility assumption, the projection method is applied. Coming from the possibility of writing the velocity as the sum of a rotational part and a potential part, the projection method consists in writing the difference $V^{n+1} - V_i^{n,3}$ as the gradient of a potential function. This predictor velocity $V_i^{n,3}$ is, hence, projected on the divergence free sub-vector space through the introduction of the potential Φ^{n+1}, solution of the following Poisson equation:

$$\rho \frac{V^{n+1} - V^{n,3}}{\Delta t} = -\nabla \Phi^{n+1} \tag{3.11}$$

Given the divergence free property of $\boldsymbol{V^{n+1}}$, the divergence of equation (3.11) provides the final version of the Poisson equation:

$$\nabla \left(\frac{1}{\rho} \nabla \Phi^{n+1} \right) = \frac{1}{\Delta t} \nabla V^{n,3} \tag{3.12}$$

Following the resolution of the potential field Φ^{n+1}, we can deduce the final velocity field V_i^{n+1} from equation (3.11). Finally the pressure field is obtained according to the condition of second order time precision at time $t^{n+1/2}$ which gives:

$$P^{n+1/2} = P^{n-1/2} + \Phi^{n+1} \tag{3.13}$$

For the simulation of two-phase flows, the one fluid method detailed in the next section is based on the use of a non-uniform density. As a consequence, the resolution of equation (3.12) gets more complicated than for one phase flows. In particular, because the variations of ρ are important from liquid to air, the corresponding time-dependent matrix becomes poorly conditioned. Though a direct method based on the Cholesky algorithm can be used to solve the Poisson equation in 2D, iterative methods are necessary for 3D configurations.

3.1.3 Two phase flow system of equations

Navier-Stokes equations

The mass and momentum conservation equations are written in an absolute referential according to an Eulerian description of the motion. The two fluids considered are Newtonian, incompressible and no-miscible. The flow is isotherm, so the energy conservation equation is not considered here. The conservative form of the mass and momentum equations in each phase or fluid k is then given by:

$$\nabla.\boldsymbol{V_k} = 0 \tag{3.14}$$

$$\rho_k \frac{\partial \boldsymbol{V_k}}{\partial t} + \nabla.(\rho_k \boldsymbol{V_k}\, \boldsymbol{V_k} - \boldsymbol{\tau_k}) = \boldsymbol{F_{k,ext}} - \nabla p_k \tag{3.15}$$

With the corresponding notations:

- $\boldsymbol{V_k}$: the flow velocity,
- $\boldsymbol{\tau_k}$: the tensor of viscous stress,
- $\boldsymbol{F_{k,ext}}$ the density of external forces,
- p_k: the pressure field,
- ρ_k: fluid density,

In this form, the equations are valid for any system of curvilinear orthogonal coordinates.

Boundary condition at the interface

Essential for the two-phase flows behavior, the corresponding conditions of conservation are derived at the interface. We consider here a constant surface tension.
Considering that the two fluids are no miscible and that there is no mass transfer or phase change at the interface, the mass conservation at the interface is given by the continuity of

the velocity normal to the interface:

$$\boldsymbol{V_k.n = W.n} \tag{3.16}$$

where **W** is the interface velocity and $\boldsymbol{n}$ is the normal to the interface. Considering F(**x**,t)=0 the equation of the interface location, the normal component of the interface velocity can be obtained with the kinematic equation:

$$\frac{1}{\mid \nabla F \mid}\frac{\partial F}{\partial t} + \boldsymbol{W.n} = 0 \tag{3.17}$$

where the normal of the interface is defined by $\mathbf{n} = \nabla F / \mid\mid \nabla F \mid\mid$. Further conditions are still needed to solve completely the motion of the interface in the case of a deformable particle. They arise from the momentum balance at the interface, considering a uniform surface tension σ. The tangential and normal stress forces are balanced respectively as :

$$\boldsymbol{t}.(\boldsymbol{\tau_1} - \boldsymbol{\tau_2}).\boldsymbol{n} = 0 \tag{3.18}$$

$$-p_2 + p_1 + \boldsymbol{n}.[(\boldsymbol{\tau_2} - \boldsymbol{\tau_1}).\boldsymbol{n}] = \sigma\kappa \tag{3.19}$$

where $\kappa = \nabla.\boldsymbol{n}$ is the mean curvature, **t** is the vector tangent to the interface and $\boldsymbol{\tau_k}$ is the stress tensor: $\tau_k = \mu_k[\nabla V_k + \nabla^T V_k]$

3.1.4 One fluid model

The aim of this model is to solve a single set of equations for the whole two-phase flow despite the change of fluid properties on both sides of the interface. The one fluid system of equation is obtained by using the VOF function C defined as:

$$C(\tilde{x}, t) = \begin{cases} 1 & in\ phase\ 1 \\ 0 & in\ phase\ 2 \end{cases} \tag{3.20}$$

The one fluid variables V, p, ρ, μ are defined as:

$$\begin{aligned} \rho &= C\,\rho_1 + (1-C)\,\rho_2 \\ \mu &= C\,\mu_1 + (1-C)\,\mu_2 \end{aligned} \tag{3.21}$$

Considering equations (3.14) and (3.15) for each phase, the equation satisfied by the one fluid variables are in the absence of mass transfer at the interface:

$$\boldsymbol{\nabla . V} = 0 \tag{3.22}$$

$$\rho\frac{\partial \boldsymbol{V}}{\partial t} + \nabla(\rho \boldsymbol{V}\boldsymbol{V}) = -\boldsymbol{\nabla} P + \rho \boldsymbol{g} + \boldsymbol{\nabla}.\tau + \boldsymbol{F_{\sigma,S}} \tag{3.23}$$

where τ is the viscous stress tensor, $\mathbf{g}$ the gravity acceleration and $\boldsymbol{F_{\sigma,S}}$ the capillary contribution of the interface (see details in section (3.1.5)). The interface motion is described by the hyperbolic transport equation:

$$\frac{\partial C}{\partial t} + \boldsymbol{V}.\nabla C = 0 \tag{3.24}$$

A large number of methods to determine the location and motion of the interface at each step time has been developed. The one that we use in this study is the level set method. We will detail the corresponding algorithm and the advantages to use it in the next section. Basically, when the level set method is applied, the volume fraction in cells close to the interface is defined as an approximation of the Heavyside function of a signed distance function $\varphi(\boldsymbol{x}, t)$ representing the normal distance from the point $\mathbf{x}$ to the interface at time t:

$$C = \overline{H}(\varphi) = \begin{cases} 0 & if\ \varphi < -\epsilon\,, \\ 0.5\left(1 + \dfrac{\varphi}{\epsilon} + \dfrac{1}{\pi} sin\left(\dfrac{\pi\varphi}{\epsilon}\right)\right) & if\ \mid \varphi \mid \leq \epsilon\,, \\ 1 & if\ \varphi > \epsilon\,, \end{cases} \tag{3.25}$$

where $\epsilon = \sqrt{2}\Delta x$ represents half the numerical thickness of the interface. Given the $\mathbf{C}$ field, the equation (3.23) is spatially discretized and advanced in time according to the scheme exposed before. We present in the following the level set method, and the calculation of the capillary force $\boldsymbol{F_{\sigma,S}}$.

3.1.5 The Level Set method

A large number of Eulerian methods have been developed to reproduce the motion of interfaces in two-phase flows. They can be classified in two families: front tracking methods and volume tracking methods. Among the volume tracking methods, the level set method presents some advantages on the interface location determination and the associated forces that led us to choose it for the present study. On one hand, the continuity of the Level Set function predicts the location of the interface through a smooth transition from one fluid to the other that makes it transport easier. Most of all, this method is the most interesting for the present study because it conserves a constant thickness of the interface, so there is no memory of the numerical thickness when the interface is moving toward a refined region (The grid is here refined close to the wall). The level-Set method has been implemented in JADIM by Abadie (2013).

The smooth transition between the two phases provides a good precision of the normal direction and the curvature of the interface. For the liquid-gas system studied in this work, the level-set function is positive in the liquid, negative in the gas and zero at the interface, according to the following definition:

$$\varphi(\boldsymbol{x},t) = \begin{cases} +d & if\ \boldsymbol{x}\ is\ in\ the\ liquid, \\ -d & if\ \boldsymbol{x}\ is\ in\ the\ gas, \\ 0 & if\ \boldsymbol{x}\ is\ at\ the\ interface, \end{cases} \tag{3.26}$$

where d represents the normal distance between the point **x** and the interface. The evolution of this function is given by the advection equation:

$$\frac{\partial \varphi}{\partial t} + V.\nabla(\varphi) = 0 \tag{3.27}$$

The time advancement of the function φ is achieved according to a third order Runge-Kutta scheme while the advective term is discretized with a WENO5 scheme. The 0 level-set contour ($\varphi = 0$) which corresponds with the interface location is well advected with this method. However, the level-set function needs to be reinitialized after each time step in order to stay as close as possible of a distance function. Initiated with the same 0 level-set contour, the new distance function corresponds with the steady solution of the differential equation:

$$\frac{\partial \varphi}{\partial \tau} = sgn(\varphi)(1 - \mid \nabla \varphi \mid)) \tag{3.28}$$

This reinitialization step has been proposed by Sussman et al. (1994) as a solution to the problem of mass conservation. Finally, according to this new Level-Set function, the new volume fraction (C^{n+1}) is given by the equation (3.25) and the density and viscosity field (ρ^{n+1} and μ^{n+1}) can be calculated with equation (3.21). Then the new pressure and velocity fields can be calculated by solving equations (3.23). To solve the problem of mass loss generated by the reinitialization step, the mass is corrected by comparing the bubble mass between two time steps and reallocating it in the relevant isocontour around the interface Abadie (2013).

3.1.6 The capillary force

According to the one-fluid formulation of the Navier-Stokes equations the expression for the capillary force is given by:

$$\boldsymbol{F}_{\sigma,S} = -\sigma\,(\nabla.\boldsymbol{n}).\boldsymbol{n}\delta_I \tag{3.29}$$

where σ is the surface tension, $\mathbf{n}$ is the unit vector normal to the interface and δ_I is the delta function of the interface location. The Continuum Surface Force model proposed by Brackbill et al. (1992) transforms this expression into a volume force:

$$\boldsymbol{F}_{\sigma,V} = -\frac{\sigma}{V}\,\overline{\nabla C}\int_{\partial S}\left(\frac{\boldsymbol{\nabla}\varphi}{||\,\boldsymbol{\nabla}\varphi\,||}\right).\boldsymbol{n_{cell}}\,dS \tag{3.30}$$

where the delta Dirac function is approximated by the derivative of the Heavyside function (equation (3.25)): $\overline{\nabla C}$ defined here as the mean volumic value of the gradient of the volume fraction over the local cell. The term $\dfrac{\nabla\varphi}{||\,\nabla\varphi\,||}$ gives the normal direction and its flux integral over the cell surface gives the curvature.

3.1.7 Sum up of the algorithm

To provide a global view of the algorithm of resolution of the one fluid system of equations in JADIM, we summarize and order the different steps. Starting from the data of pressure, velocity and volume fraction fields of the previous time step n or the initial condition, the algorithm develops as:

1. Advection of the Level-Set function and determination of the new fields of C^{n+1}, ρ^{n+1}, μ^{n+1}.

2. Determination of the intermediate values : $C^{n+1/2}$, $\rho^{n+1/2}$, $\mu^{n+1/2}$.

3. Runge-Kutta / Crank Nicholson scheme for the determination of the rotational part of the velocity field $\boldsymbol{V}^{n,3}$.

4. Calcul of the Capillary force $\boldsymbol{F}_{\sigma,V}^{n+1}$.

5. Resolution of the Poisson equation which provide the new velocity and pression fields $\boldsymbol{V}^{n+1}$, P^{n+1}

3.2 Numerical configurations

The purpose of the numerical part of this project is to simulate with JADIM the 2D interaction between a bubble and an inclined wall in conditions similar to the experimental conditions. For this purpose we designed a rectangular domain inside which a bubble is introduced as shown in Figure 3.2. The bubble is initially at rest and is driven by the gravity toward the upper limit of the domain, conditioned as a wall. The inclination of the wall is implemented by the inclination of the gravity:

$$g_x = -g\,sin(\theta) \quad , \quad g_y = -g\,cos(\theta) \tag{3.31}$$

where θ is the inclination angle. The left and right limits of the domain are periodic. In this way, the dimensions of the domain can be maintained constant for the whole range of inclination angle considered ($0° \leq \theta \leq 85°$). Two types of simulations were generated during the numerical study. First, the initial distance between the bubble and the upper wall, y_0, is chosen to ensure that the bubble achieves its terminal velocity before it collides with the wall. Considering that both the liquid and the bubble are initially at rest, the terminal conditions of the bubble are entirely governed by the physical parameters of the liquid, the bubble and the interface. For the second case, the bubble was initially located close to the wall.

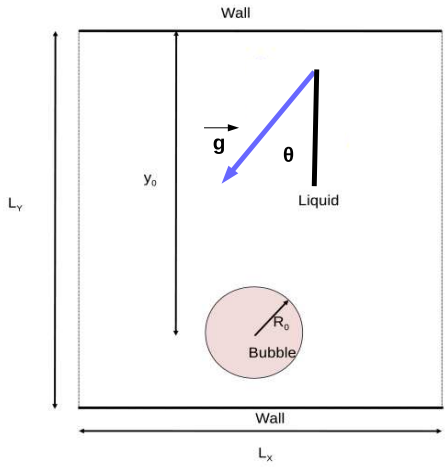

Figure 3.2: Geometry and boundary conditions for the numerical representation of the bubble inclined wall configuration

3.3 Mesh Study

3.3.1 Mesh description

When a bubble gets close to a wall a liquid film forms between the bubble and the wall and velocity gradients appear in the liquid film. Considering this flow characteristics, a non uniform mesh is generated in the rectangular domain in order to accurately mesh the lubrication film that forms between the bubble and the wall. The flow being parallel to the wall in this region, the vertical dimension of the meshes should decrease strongly close to the wall whereas the horizontal dimension of the meshes can be maintained constant in the whole domain. In addition, a significant number of cell meshes is needed along the interface in order to optimize the precision of the surface tension effects and shape evolution. As a consequence, the size of the meshes should be sufficiently small to reproduce all the momentum and energy transfers but large enough so that the time of simulation do not become extremely large.

Considering a constant horizontal size of the meshes, the vertical size of the meshes is constructed. First, a geometric progression is chosen in order to progressively refine the grid

close to the wall:

$$(\Delta y)_j = k\,(\Delta y)_{j-1} \tag{3.32}$$

where Δy_j is the vertical grid spacing of the j^{th} mesh counted vertically from the wall to the bottom of the domain. The geometric coefficient k is the same for all the cases. This relation is valid until the distance between the wall and the point y_j becomes larger than one diameter. Then the vertical size of the meshes is kept constant for the rest of the domain. The different characteristics of the meshes considered in this study are reported in table 3.2.

Mesh	Symbol	$\Delta y_{wall}(mm)$	Δy_{far}	Δx	N_{cells}	$\Delta t\,(s)$	$N_{step}\,(0.5sec)$	$T_{simulation}$ (days)
8	●	$1.0\,10^{-5}$	$2.77\,10^{-4}$	$2.77\,10^{-4}$	218×598	$1.9\,10^{-7}$	$2,577,319$	74
7	●	$1.5\,10^{-5}$	$2.81\,10^{-4}$	$2.81\,10^{-4}$	214×554	$3.6\,10^{-7}$	$1,396,648$	41
6	●	$2.0\,10^{-5}$	$2.84\,10^{-4}$	$2.84\,10^{-4}$	212×522	$5.6\,10^{-7}$	$892,860$	26
5	●	$2.5\,10^{-5}$	$2.92\,10^{-4}$	$2.92\,10^{-4}$	206×496	$7.7\,10^{-7}$	$651,041$	13
4	●	$3.0\,10^{-5}$	$2.99\,10^{-4}$	$2.99\,10^{-4}$	204×474	$1.0\,10^{-6}$	$500,000$	9
3	●	$3.3\,10^{-5}$	$3.00\,10^{-4}$	$3.00\,10^{-4}$	200×464	$1.2\,10^{-6}$	$423,728$	7
2	●	$6.7\,10^{-5}$	$2.64\,10^{-4}$	$2.64\,10^{-4}$	228×442	$3.3\,10^{-6}$	$149,700$	5
1	●	$9.9\,10^{-5}$	$3.01\,10^{-4}$	$3.01\,10^{-4}$	198×376	$1.0\,10^{-5}$	$50,000$	1

Table 3.2: Characteristics of the different 2D meshes tested for the interaction of a bubble with an horizontal wall: Δy_{wall} is the vertical grid spacing of the mesh close to the wall, Δy_{far} is the vertical dimension of the meshes located at a distance larger than one bubble diameter from the wall, Δx is the horizontal dimension of the meshes, $N_x \times N_y$ is the total number of cells, Δt is the time step of the simulation, N_{step} the number of time steps necessary to simulate 0.5 seconds, $T_{simulation}$ the corresponding time of simulation. The simulation were run on the MIZTLI supercomputer of the UNAM (118 TFlop/s, 5.312 cores of Intel E5-2670, 16 NVIDIA cards m2090 and 15.000 Gbytes of RAM) with the optimal number of cores.

3.3.2 Mesh comparison

To compare the different meshes (i.e. the different grid refinements close to the wall), the interaction of the bubble with the horizontal wall as presented in Figure (3.2) is simulated using the 8 meshes of Table 3.2 and considering the following parameters in Table 3.3:

$L_x \times L_y$ m^2	ρ_l kg/m^3	μ_l $Pa.s$	ρ_g kg/m^3	μ_g $Pa.s$	σ N/m	D_{eq} mm	g $m.s^{-2}$	Mo	Bo
0.06×0.1	1000	0.025	10	0.00025	3.44	20	9.81	10^{-10}	1.14

Table 3.3: Physical properties for the numerical simulations conducted for the mesh study for the bubble horizontal wall interaction. The subscript l refers to the liquid properties while the subscript g refers to the bubble properties.

Mo is the Morton number ($Mo = \frac{g\,\mu_l^4}{\rho_l\,\sigma^3}$) and Bo the Bond number ($Bo = \frac{\rho_l\,g\,D_{eq}^2}{\sigma}$). Accordingly, it should approximately correspond to the behavior of experimental conditions E9 of Table 2.1 for a 2.9 mm diameter bubble rising in water glycerol mixture of 90-10 % in mass that corresponds to the Morton number $Mo = 5.09 \times 10^{-11}$ and to the Bond number $Bo = 0.9225$.

The effects of the mesh-refinement on the time evolution of the position and vertical velocity of the bubble are presented in Figure (3.3). Although the terminal conditions achieved by the bubble before colliding is the same for all the mesh systems, a complete different behavior is observed for Mesh 1-2 and the other meshes. The amplitude of the first bounce is much smaller and the temporal velocity evolution changes drastically at $t = 0.24$ s. To clarify this specific behavior, the shape of the bubble for four characteristic times of the collision process is presented in Figure (3.4) for Mesh 1, Mesh 3 and Mesh 6:

- t_1: when the bubble achieves its terminal condition
- t_2: when the distance between the bubble and the wall is minimum
- t_3: when the tale of the bubble start to leave the wall
- t_4: when the distance between the bubble and the wall is maximum

As expected, the shape of the bubble during the free rise of the bubble (t_1 and the first part of the collision (t_2) is exactly the same for all the meshes. However we can see for time t_3 and t_4 that the bubble coalesces with the wall for the coarser mesh. In fact, the size of the meshes close to the wall is too large to capture the lubrication film formation and drainage.

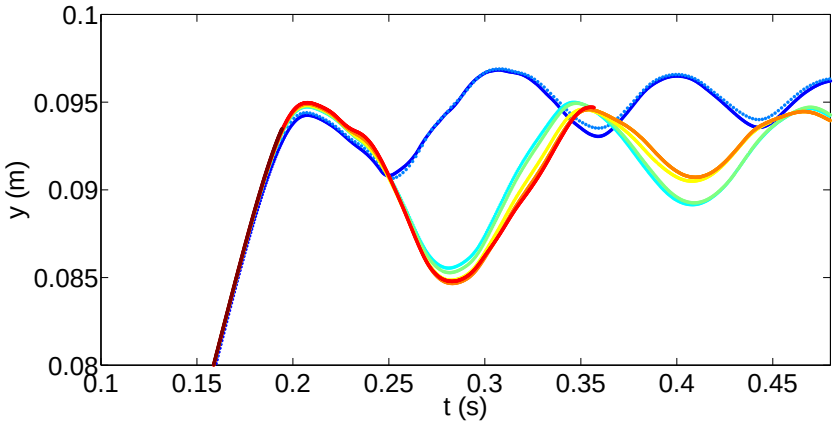

(a)

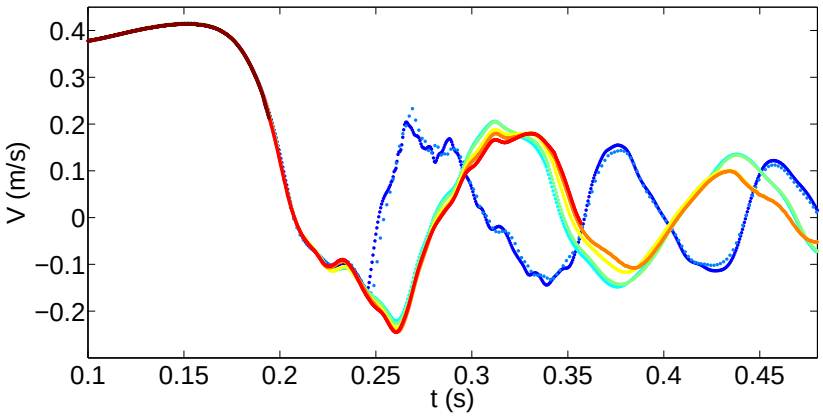

(b)

Figure 3.3: Time evolution of the position (a) and vertical velocity (b) of a 2D 20 mm diameter bubble in conditions similar to experiment E9 in table 2.1 colliding with an horizontal wall. The figure is color-coded according to the corresponding mesh system used as detailed in Table 3.2. The data plotted are color coded according to the mesh used: • $\Delta y_{wall}(mm) = 9.9 \times 10^{-5}$, • $\Delta y_{wall}(mm) = 6.7 \times 10^{-5}$, • $\Delta y_{wall}(mm) = 3.3 \times 10^{-5}$, • $\Delta y_{wall}(mm) = 3.0 \times 10^{-5}$, • $\Delta y_{wall}(mm) = 2.5 \times 10^{-5}$, • $\Delta y_{wall}(mm) = 2.0 \times 10^{-5}$, • $\Delta y_{wall}(mm) = 1.5 \times 10^{-5}$ and • $\Delta y_{wall}(mm) = 1.0 \times 10^{-5}$

On the other hand, different behaviors between Mesh 3-4 and the others can also be identified even if the differences are less significant. The dynamics of the bubble during the first bounce ($t = 0.2 - 0.34$ s) can be considered similar, but from the beginning of the second collision the bubble behaviors are different. Figure 3.4 clearly shows that the evolutions obtained with Mesh 3 and 6 are very close, demonstrating a good grid convergence.
Finally, in order to limit the time of the simulation, the Mesh 3 ($\Delta y_{wall} = 3.33 \times 10^{-5}$ mm) has been chosen for all the simulations reported in this work. Typically, the time of simulation necessary to describe a complete bubble wall interaction would be definitively too large (104 days for Mesh 3 against 164 days for Mesh 6 for 2 seconds of simulations). Furthermore, the grid convergence obtained with Mesh 3 appears to be satisfactory for the purpose of the study (steady state and collision).

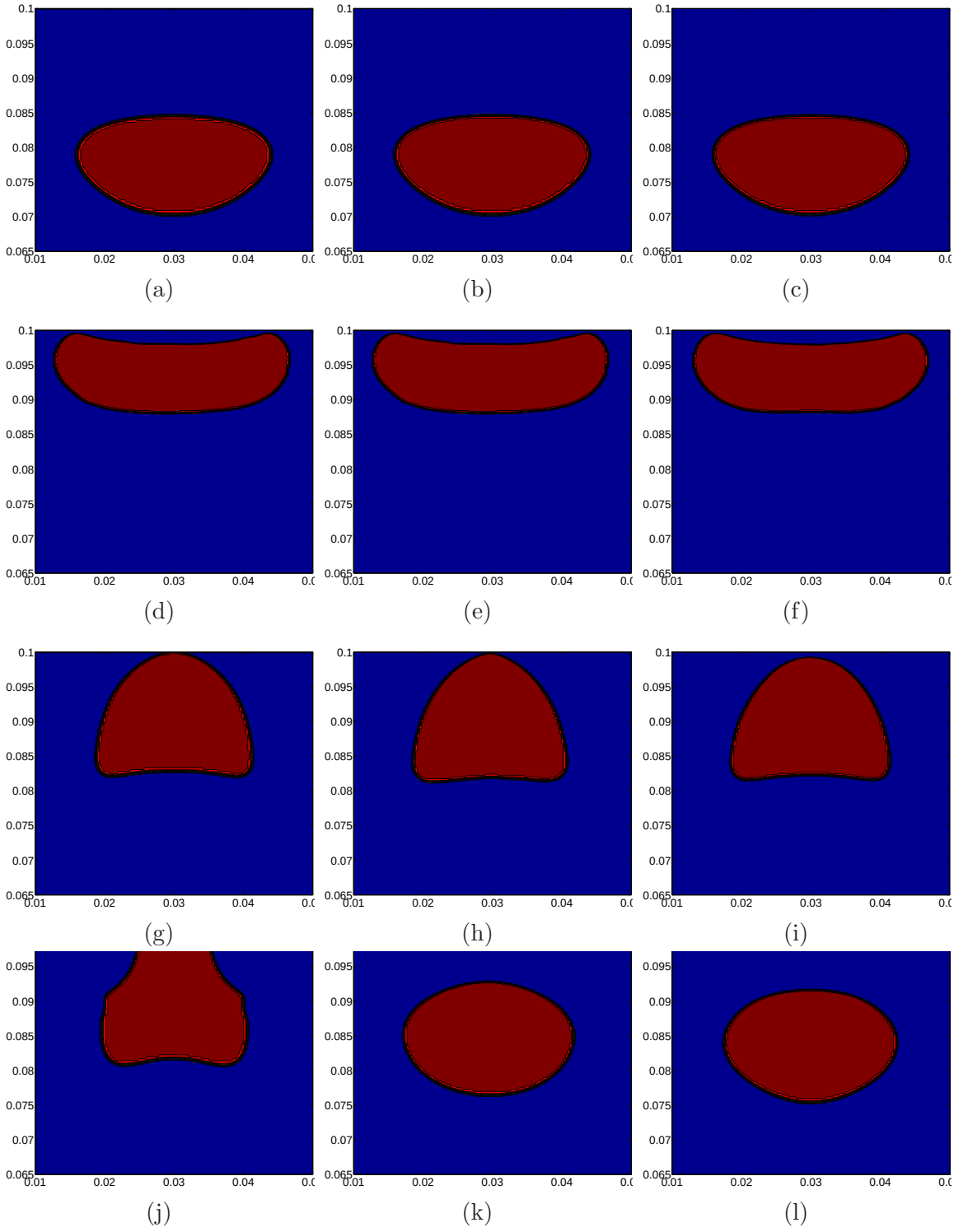

Figure 3.4: Map of the volume fraction $C(\tilde{x}, t)$ of a 2D bubble rising in conditions similar to experiments E9 and interacting with an horizontal wall is shown at characteristic times t_1, t_2, t_3 and t_4 (from top to bottom respectively). From left to right, results corresponding to Mesh 1,2 and 3 respectively are reported. The Map is color coded such that the red color corresponds to the bubble and the blue color to the liquid. Each image is plotted vertically and horizontally as a function of the position in mm.

3.4 Conclusion

The JADIM code used in this work has been introduced. The level set method will be used for the simulation of a 2D bubble impact on the wall. We have conducted a grid convergence study in order to select the best mesh for the simulation. The corresponding results are discussed in Chapter 8.

Chapter 4

Two types of steady bubble-wall interactions

4.1 Terminal conditions

In the present study, bubbles reach their terminal conditions before colliding with the inclined wall. Important information such as liquid contamination, bubble shape and wake structure can be deduced from the terminal conditions of the bubble. Such information is important since it affects the steady motion of the bubble.

The free rise of bubbles in the experimental conditions of Table 2.1 are observed with the experimental apparatus of Figure 2.1, without the presence of the upper wall. The terminal Reynolds and Bond numbers ranged from 140 to 1000 and from 0.3 to 2.5, respectively. Considering Clift et al. (1978) map, this dimensionless numbers correspond to ellipsoidal and wobbling bubbles. Images of typical shapes of free rising bubbles are shown in Figure 4.1. Considering the range of equivalent diameters used, $1 \leq D_{eq} \leq 3$ mm, rectilinear path as well as zig-zag and helical paths were observed. Legendre et al. (2012) proposed an expression for the evolution of the aspect ratio of bubbles rising freely in liquid at rest considering large

(a) E1 (b) E10 (c) E11

Figure 4.1: Images of typical shape of free rising bubbles, respectively an almost spherical bubble, an ellipsoidal bubble and a wobbling bubble. The subcaption numbers refer to the corresponding experimental conditions of Table 2.1 (a) Experiment 1: $Re_{term} = 144$, $We_{term} = 1.8$, $\chi_{term} = 1.31$ and $D_{eq} = 1.1$ mm; (b) Experiment 10: $Re_{term} = 614$, $We_{term} = 2.9$, $\chi_{term} = 1.78$ and $D_{eq} = 1.6$ mm, (c) Experiment 11: $Re_{term} = 950$, $We_{term} = 3.6$, $\chi_{term} = 1.93$ and $D_{eq} = 3.1$ mm. Images are shown at the same scale.

ranges of Weber and Morton numbers:

$$\chi_{term} = \frac{1}{1 - \frac{9}{64} We_{term} \left(1 + K(Mo)\, We_{term}\right)^{-1}}, \tag{4.1}$$

with $K(Mo) = 0.2\, Mo^{1/10}$. The experimental aspect ratio of the bubbles in this study are calculated from the Legendre polynomial expansion. As illustrated in Chapter 2, in a spherical coordinate system where the origin coincides with the bubble center, the Legendre polynomial expansion of the interface location is calculated. From the radial position expression, considering the largest bubble axis as the major axis and the minor axis as the axis orthogonal to it, the aspect ratio is calculated. The evolution of the terminal aspect ratio with the terminal Weber number for the entire range of experimental conditions considered in this investigation is presented in Figure 4.2. The prediction of equation (4.1) is plotted for Morton numbers 5×10^{-9}, 1×10^{-9} and 2×10^{-11} in blue line, cyan line and orange line respectively. The original expression proposed by Moore (1965) is plotted with a black line:

$$\chi_{term} = 1 + \frac{9}{64} We_{term} \tag{4.2}$$

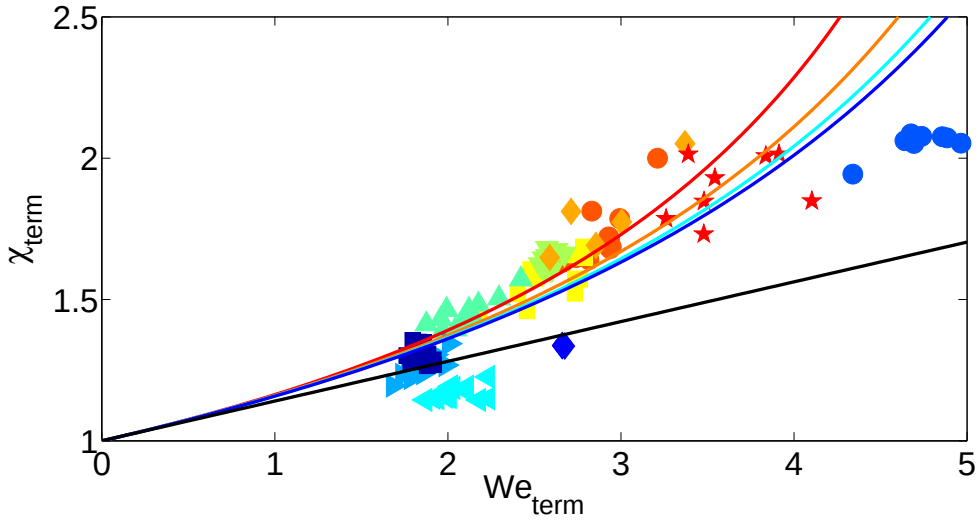

Figure 4.2: Map of terminal Weber numbers, We_{term}, and aspect ratio, χ_{term}, corresponding to the experimental conditions of Table 2.1 and plotted with the corresponding symbol codes. The continuous lines correspond to equation (4.1) plotted without the Morton term, with $Mo = 0$, $Mo = 5 \times 10^{-9}$, $Mo = 1 \times 10^{-9}$ and $Mo = 2 \times 10^{-11}$ in red, orange, cyan and blue lines respectively. The theoretical evolution of the aspect ratio proposed by Moore (1965) is plotted in black line.

A similar evolution of the aspect ratio with the Morton number is observed between experimental data and the correlation of Legendre et al. (2012). However for large values of Morton number, expression (4.1) overestimates the experimental values. Two interpretations are proposed for this observation. For low We_{term} numbers, E5 corresponds to a Ethylen-glycol and water mix that are, as we will see later, strongly contaminated. Therefore, the bubble interface may stiffen and the bubble would tend to retain a spherical shape. In other words, a smaller aspect ratio is obtained for some values corresponding to a more contaminated liquid. No special care was taken to eliminate completely the presence of impurities in the liquids used, so the terminal conditions may be affected by this effect. To limit this phenomenon, the liquid was replaced by a new one as soon as a significant change of the terminal shape of the bubble was detected. As a result, the contamination of the liquid may vary not only from one experimental condition to another but also within the same experimental conditions.

For large values of We_{term}, for E3, E9 and E11, wobbling bubbles are generated. A large

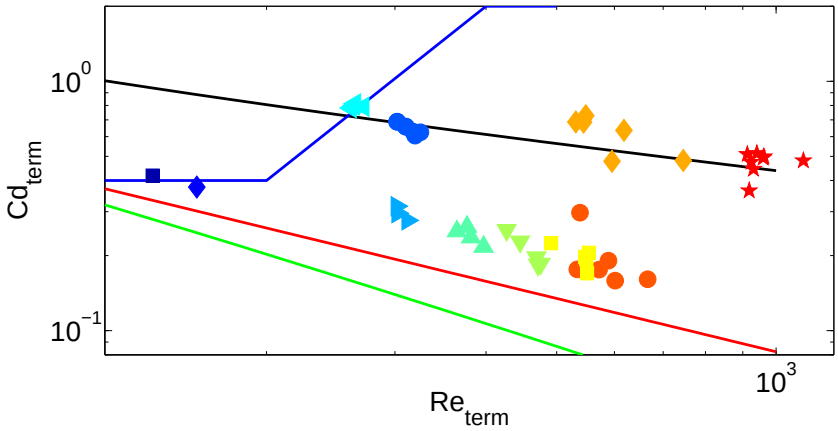

Figure 4.3: Map of terminal drag coefficient, Cd_{term}, and terminal Reynolds number, Re_{term}, calculated from equation (4.3) for the experimental conditions of Table 2.1 and plotted according to the corresponding symbol codes. The green red and black continuous lines correspond to Moore (1965), Maxworthy et al. (1996) and Schiller and Naumann (1933) expressions respectively. For the green line an aspect ratio of 1 is taken in the corresponding drag coefficient expression proposed by Moore (1965). The drag coefficient evolution, taking into account the shape evolution of the bubble given by Moore (1965) is shown in blue line for $Mo = 5 \times 10^{-9}$.

deformation is observed for these bubbles, in all the directions, and as a consequence an extended range of aspect ratio is measured. The area of observation was indeed too small to measure precisely the mean values of aspect ratio and terminal velocity that evolved continuously.

The combined effects of the bubble deformation and the presence of impurities on the bubble dynamics complicates the interpretation of the results. Both effects can be identified more clearly through the analysis of the terminal drag coefficient. The experimental steady drag coefficient is inferred indirectly from the balance between the buoyancy force and the drag force acting on the bubble in the vertical direction:

$$Cd_{term} = \frac{4}{3}\frac{D_{eq}g}{U_{term}^2} \tag{4.3}$$

Based on the boundary layer theory, Moore (1965) proposed an expression of the drag coefficient that accounts for the bubble shape evolution. With this expression, the increase of

the drag coefficient as the bubble shape and accordingly the flow regime around the bubble evolves when the Reynolds number increases is reproduced. The corresponding drag coefficient prediction is shown in Figure 4.3 for the Morton number associated to the silicon oil. The analytical results of Moore (1965) corresponding to a bubble with a spherical shape ($\chi_{term} = 1$) for the whole range of Reynolds number is plotted with the green line. Experimental data that deviation from this curve are provoked by either the interface contamination or the bubble distortion. Hence if the bubble is deformed its drag coefficient should deviate from the green line in agreement with the evolution of the blue line. As for the effect of the contamination of the interface, the drag coefficient given by the Schiller and Naumann (1933), obtained for a solid spherical particle is considered. Indeed, the no-slip boundary conditions of a solid particle is also generated for completely contaminated bubbles. Maxworthy et al. (1996) explored experimentally the evolution of the drag coefficient of bubbles rising in clean viscous liquids for a large range of Morton numbers. They proposed an empiric expression for the drag coefficient for bubbles with the maximum aspect ratio ($\chi_{term} \approx 1.1$) that reproduces the same result as spherical bubbles. In other words, it corresponds to the lower limit of the drag coefficient of a bubble poorly contaminated at high Reynolds numbers. The correlation from Maxworthy et al. (1996) and Schiller and Naumann (1933) are then associated to nearly spherical bubbles respectively clean and completely contaminated. To evaluate the possible contamination of the bubble interface, the red and black lines in Figure 4.3 are then considered. These data will be examined in detail later.

Considering the terminal conditions of all the experiments, four categories of terminal behaviors are observed. First, experiments E1 and E2 are classified in the category of clean bubble whereas E3 generates deformed bubbles. As for experiments E5, E9 and E11 whose drag coefficient is aligned with the Schiller and Naumann (1933) correlation, they are considered as completely contaminated. Finally, the remaining experiments, that are located between the Maxworthy et al. (1996) and Schiller and Naumann (1933) relations are considered both deformed and contaminated.

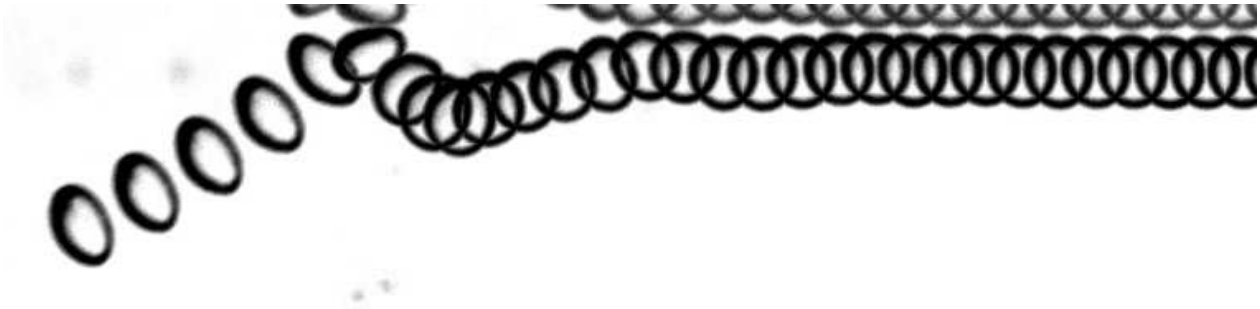

(a) Sliding motion: $\theta = 50°$

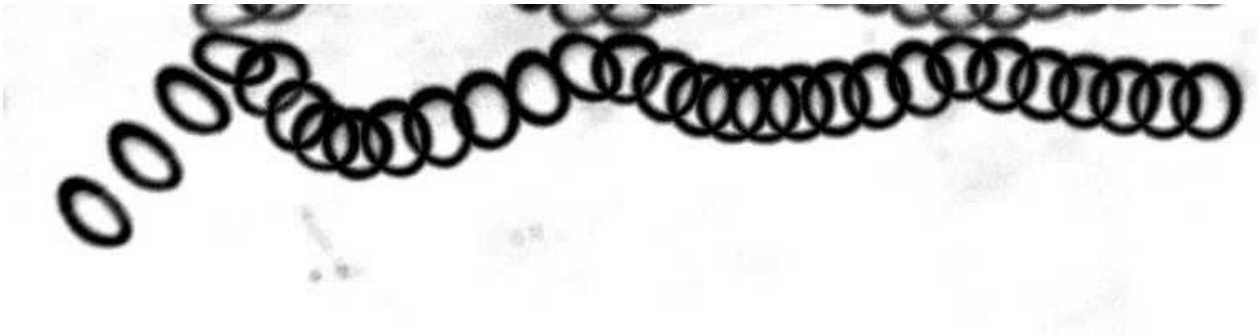

(b) Bouncing motion: $\theta = 60°$

Figure 4.4: Bubble motion for the two typical steady wall behaviors. In both cases $D_{eq} = 1.6$ mm, $Re_{term} = 500$ and $We_{term} = 2.3$, corresponding to experiment E7 conditions, from Table 2.1. The image is composed by superposing bubble positions at different instants with $\Delta t = 5$ ms. For both cases, the image was rotated to make the wall appears horizontal.

4.2 Bouncing and sliding bubbles dynamics

As reported by Tsao and Koch (1997), a change of bubble motion occurs as the inclination angle increases, in other words as the wall gets closer to the vertical alignment. The two types of bubble-wall interactions of an ellipsoidal bubble in the E3 conditions (see table 2.1 on page 10) are shown for inclination angles of 50° and 60°. For low inclination angles, Figure 4.4a, the bubble collides with the wall, observes a few bounces with a decreasing amplitude until it slides against the wall with a constant velocity. For inclination angles higher than the transition angle, θ_{trans} in Table 2.1, the motion of the bubble changes drastically, Figure 4.4b. The bouncing amplitude and period stabilize on constant non zero values with which the bubble bounces repeatedly all along the range of dimensions of the experiments ($L \sim 30$ cm). This transition was observed for the whole range of experimental conditions but with

a variant critical angle, as reported in Table 2.1. Tsao and Koch (1997) associated this transition to a critical tangential Weber number which means that the transition is influenced by the bubble deformation. However they only considered water and two bubble diameters in their study so the extent of the experimental parameters was narrow.

The bubble magnitude, tangential and normal velocity evolution with time is shown in Figure 4.5a, 4.5b and 4.5c respectively for the sliding and bouncing motion presented in Figure 4.4a and 4.4b. The time t=0 is defined as the moment when the normal velocity vanishes. Both velocity and time are plotted in dimensionless form considering V_{term} and D_{eq}/V_{term}. In agreement with Zenit and Legendre (2009), the collision of the bubble with the wall can be decomposed in successive phases. For $t^* \leq 1.5$, the magnitude velocity of the bubble is constant because the wall has not yet affected the bubble motion. Then as the bubble gets close to the wall, both normal and tangential velocity decrease. Zenit and Legendre (2009) provided a detailed description of the velocity evolution of ellipsoidal bubble rising in rectilinear path interacting with a horizontal wall. The normal velocity evolution is the same for both inclination angles. Instead, no study has been conducted for the tangential velocity evolution of an ellipsoidal bubble interacting with a wall. A detailed analysis of both tangential and normal velocity of the bubble during the collision with the inclined wall is presented in Chapter 7. Following the impact phase, for $t^* \geq 1.2$, the bubble is ejected and starts to bounce on the wall. From that time and until the end of the bounce, the wall effects on the bubble consist in the initial impulse transmitted to the bubble and the shape oscillation of the bubble. Out of this two effects, the bubble motion is the result of the balance between the buoyancy force, the drag force and the lift force. Once this transient process is completed, for about $t^* \geq 10$, the bubble motion reaches its new time-average steady state but according to the same scheme.

Clearly the inclination angle of the wall changes the bubble motion. Considering the uniqueness of the transition angle for a given experimental condition, the evolution of bubble paths for different inclination angles is shown in Figure 4.6a and 4.6b for experiments E10

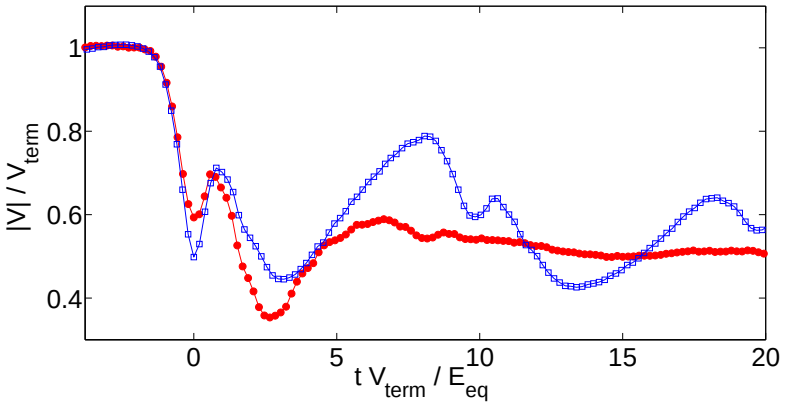

(a) Magnitude velocity

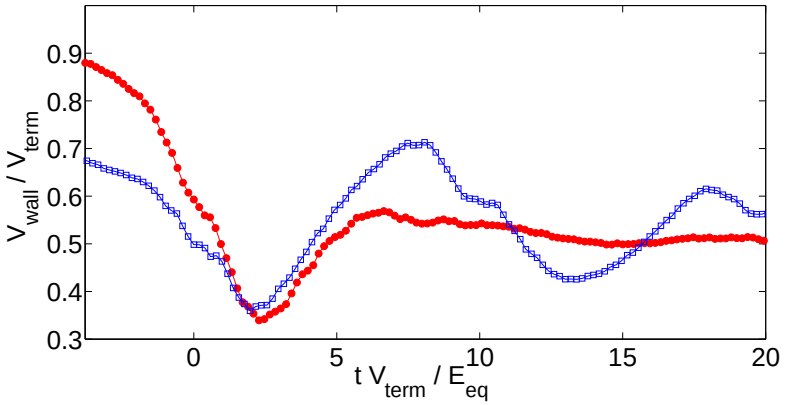

(b) Tangential velocity

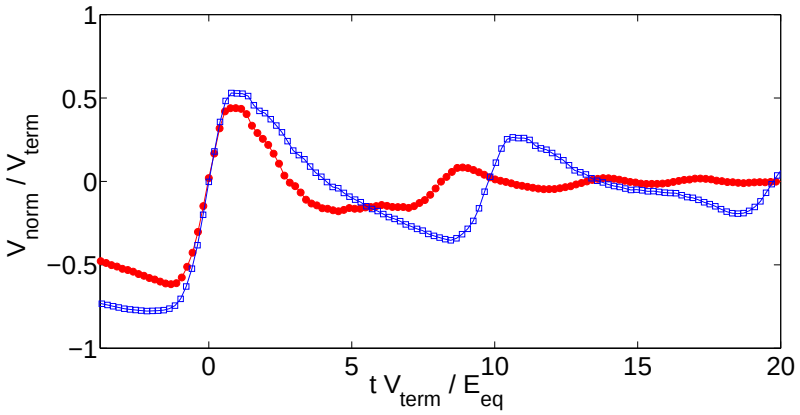

(c) Normal velocity

Figure 4.5: Evolution of the normalized magnitude (a) $|V|/V_{term}$, (b) tangential V_{wall}/V_{term} and normal (c) V_{norm}/V_{term} velocities, as a function of the normalized time tV_{term}/D_{eq}, for the experiments shown in Figure 4.4a and Figure 4.4b represented respectively by full and empty symbols.

.

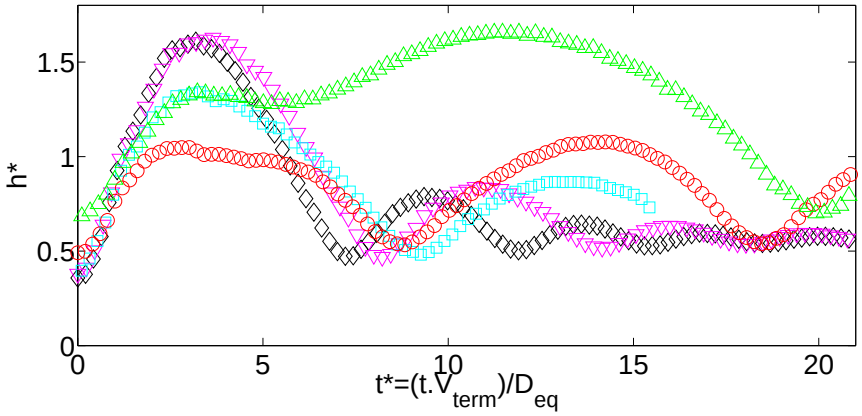

(a)

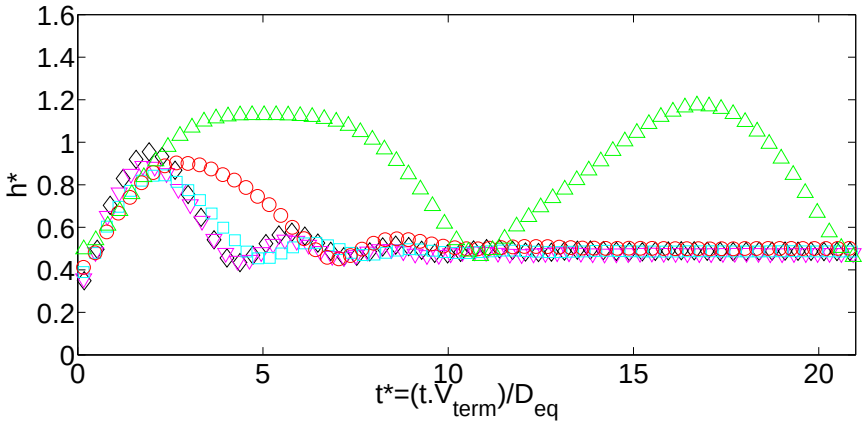

(b)

Figure 4.6: Evolution of the normalized bubble centroid-wall distance, h/D_{eq}, as a function of the normalized time, tV_{term}/D_{eq}, for (a) E10 and (b) E4. For both cases, the motion is colour and symbol-coded with respect to the corresponding inclination angle: $\theta = 15°$(◇), $\theta = 30°$(▽), $\theta = 45°$(□), $\theta = 60°$(○), $\theta = 75°$(△)

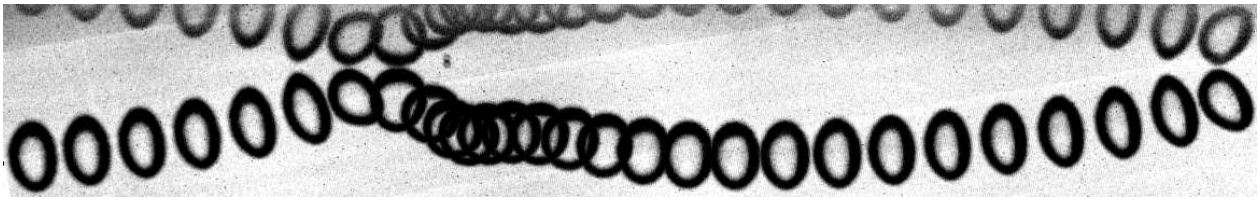

Figure 4.7: Composed bouncing bubble motion. The associated physical parameters are $D_{eq} = 1.7mm$, $Re_{term} = 510$, $We_{term} = 2.3$ and the inclination angle of the wall is 80°.

and E4 respectively (see Table 2.1, on page 10). The evolution of the normalized distance between the wall and the bubble center, h/D_{eq}, is plotted as a function of the normalized time, tV_{term}/D_{eq}. For both liquids, the bubble trajectories are colour-coded according to the inclination angle: 15° (◊), 30°(▽), 45°(□), 60°(○) and 75°(△). Based on the initial time $t^* = 0$, as defined previously, the mean temporal evolution of distance between the wall and the bubble centroid of each experiments is calculated. For the two liquids considered, different transition angles were observed as reported in Table 2.1. Because of the complex evolution of the normal and tangential components of the drag, lift and buoyancy forces on one hand, and the normal and tangential coefficient of restitutions on the other hand we do not observe a monotonic increase of the amplitude and period with the inclination angle. But a global decrease of the amplitude and period of the bounce is observed for experiment E4 which emphasize the inertial nature of the interaction. As a consequence a higher inclination angle is necessary to observe the transition of steady-wall motion (65° for E4 and 55° for E10).

If a certain inertia is achieved by the bubble after the first collision, as the 75° case in Figure 4.6a, a different bubble bouncing behavior is observed. Comparing with the 60° path of the bubble in experiment E10, an external force drives the bubble off the wall at time $t^* = 6$ instead of describing a regular bounce. De Vries et al. (2002) associated this peculiar behavior to the change of the wake structure as the bubble impact the wall. When the bubble inertia is high enough after the collision, the wake restructure into a vortex blob whose velocity field generate a force strong enough to change the bubble path. We will refer

to this bubble path as composed bouncing motion. An example of this case is reported in Figure 4.7, where the interaction of a 1.7 mm diameter bubble with a 70° inclined wall is represented. Though particularly interesting, this behavior was not studied in detail in this thesis.

4.3 Visualization of the wake

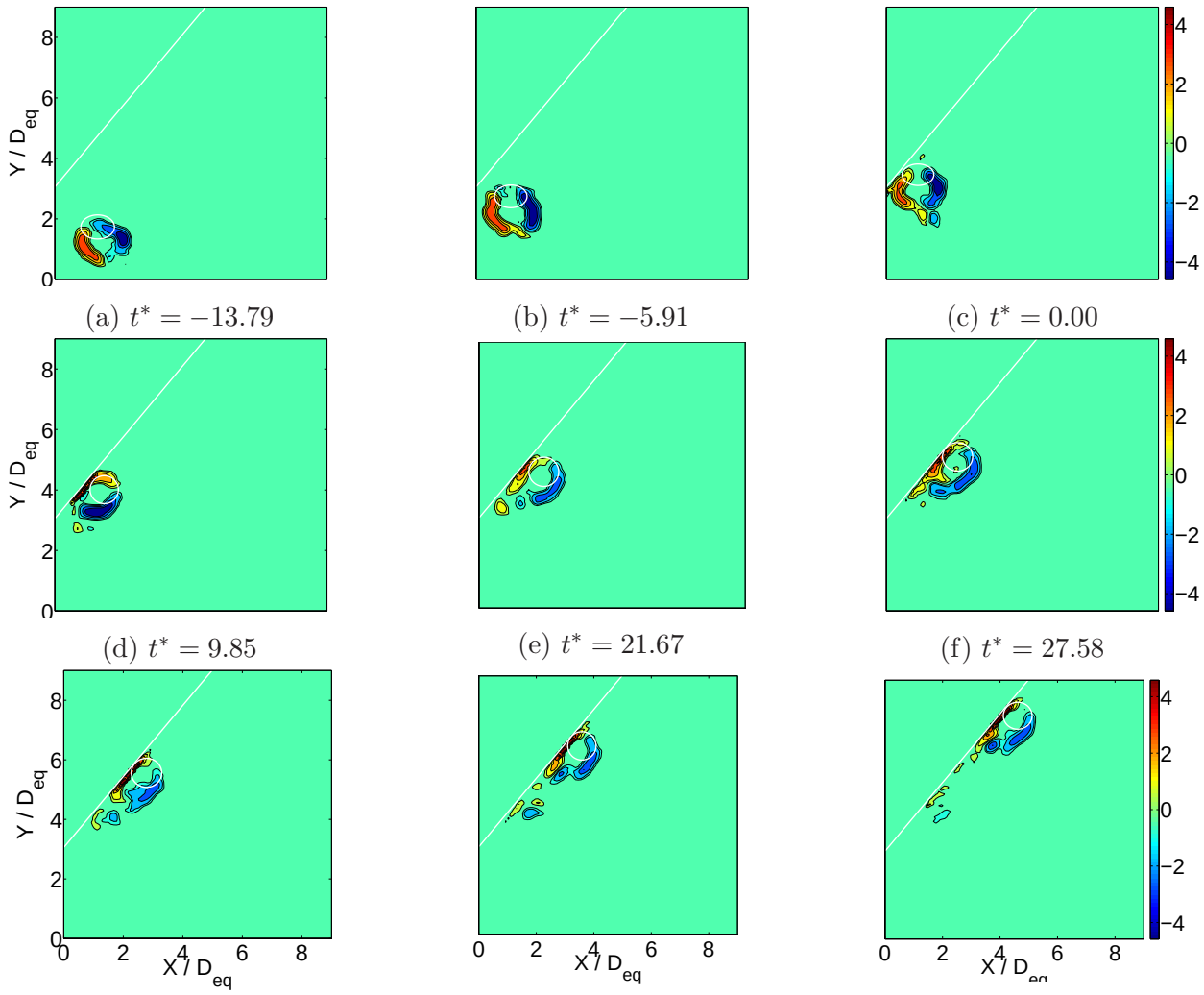

(a) $t^* = -13.79$ (b) $t^* = -5.91$ (c) $t^* = 0.00$

(d) $t^* = 9.85$ (e) $t^* = 21.67$ (f) $t^* = 27.58$

(g) $t^* = 35.46$ (h) $t^* = 51.22$ (i) $t^* = 70.92$

Figure 4.8: The temporal evolution of the dimensionless vorticity field, defined as $\omega^* = \dfrac{\omega D_{eq}}{U_{term}}$, and the approximate position and shape of a bubble rising in liquid 1 with $Re_{term} = 603$ and $We_{term} = 2.87$ are shown for an inclination angle of $\theta = 50°$. The corresponding time are reported in the top left corner of each map in terms of $t^* = \dfrac{tU_{term}}{D_{eq}}$.

Numerous authors have studied the influence of the wake velocity field, present along the bubble path, on the bubble shape and dynamics evolutions. Regarding free rising ellipsoidal bubbles, Ellingsen and Risso (2001) considered the onset of the transition between plane zig-zag path and helical path. This transition was indeed related to the wake structure evolution.

Vortices are generated at the rear of the bubble which develop along the bubble wake. These vortices produce a hydrodynamic force that is responsible for the bubble zig-zag and helical motion. Using the Schlieren technique, De Vries et al. (2002) visualized the double-threaded structure of the wake, composed of two counter rotating vortices. Hence, using an indirect approach De Vries et al. (2002) proposed an evaluation of this wake induced lift force. This expression was then introduced in a simple model of force balance that reproduced the different trajectories observed experimentally for a bubble interacting with a vertical wall.
In this section we study the wake structure, using the PIV technique, for the sliding and bouncing regimes of motion. For this purpose, the dimensionless vorticity field, $\omega^* = \omega D_{eq}/V_{term}$, around a 1.7 mm diameter bubble in water interacting with an inclined wall is shown before, $\theta = 50°$, and after, $\theta = 55°$, the transition in Figure 4.8 and Figure 4.9, respectively. For both figures the time evolution of the vorticity field is shown using different time steps. Due to the problem of laser reflection on the bubble interface as detailed in Chapter 2, the bubble shapes and positions reported here are only approximations of the actual interface location. Similarly the distance between the wall and the bubble is smaller than the spatial resolution of the technique, the results obtained provide a qualitative information of the wake structure evolution.

As the bubble rises freely, an asymmetric wake is generated following its zig-zag path. Two opposite vortices are generated from the bubble rear which expand along the bubble wake. Each time the bubble path changes its direction, a vortex is generated, see Figure 4.9c. Then, as the bubble impacts the wall, the vorticity present close to the bubble rear deforms asymmetrically. Progressively, the positive vorticity expands against the wall and intensify while the negative vorticity aligns with the wall direction but on the opposite side of the bubble and dissipates strongly. This vorticity configuration results from the combined effects of the strong bubble deceleration and the wake inertia. According to De Vries et al. (2002) as the bubble wake restructures into a vortex blob, the velocity field generated acts on the bubble. Hence, a strong bubble-wake interaction characterises the start of the bubble bounce.

However, unlike De Vries et al. (2002), we observe here that the bubble wake does not detach from the rear of the bubble as soon as the bounce begins but during the bounce, see Figure 4.9e, or long after the first bubble-wall interaction, see Figure 4.8g. For the bouncing motion case, $\theta = 55°$, this phenomenon is periodically reproduced each time the bubble bounces. The lifetime of this vortex blobs structures is significant. Therefore, considering a bubbly flow, the motion of the near-wall bubbles is very likely to be affected by the wake flow and the presence of these vortex blobs. Together with the larger wake inertia, the multiple vortex blobs production is the main difference between the bouncing and the sliding regimes of motion.

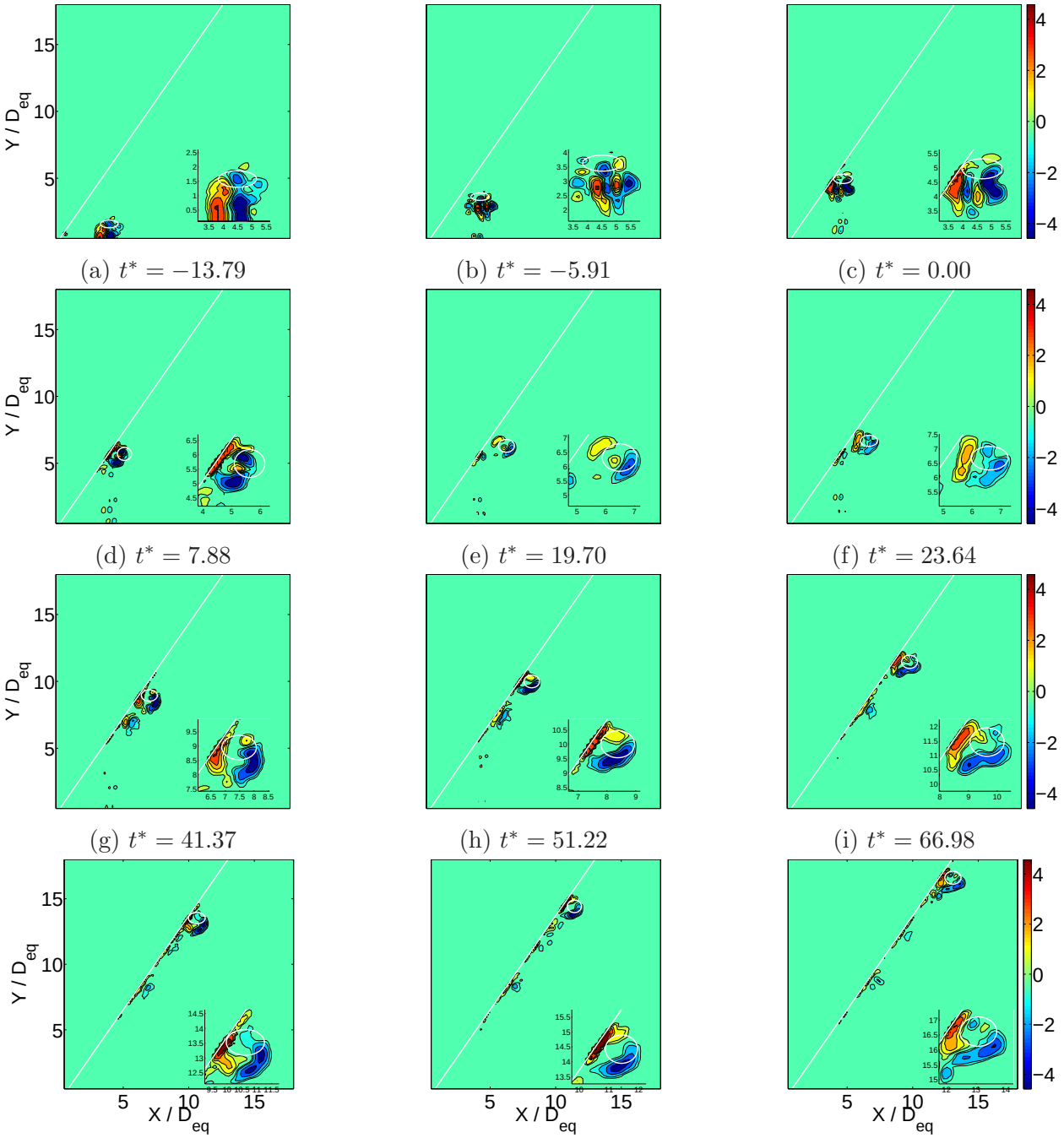

(a) $t^* = -13.79$ (b) $t^* = -5.91$ (c) $t^* = 0.00$

(d) $t^* = 7.88$ (e) $t^* = 19.70$ (f) $t^* = 23.64$

(g) $t^* = 41.37$ (h) $t^* = 51.22$ (i) $t^* = 66.98$

(j) $t^* = 82.74$ (k) $t^* = 92.59$ (l) $t^* = 114.26$

Figure 4.9: The temporal evolution of the dimensionless vorticity field, defined as $\omega* = \dfrac{\omega D_{eq}}{U_{term}}$ as well as the approximate position and shape of a 1.6 mm diameter bubble in water is shown for an inclination angle of $\theta = 55°$. The corresponding times are also reported in the top left corner of each map in terms of $t* = \dfrac{tU_{term}}{D_{eq}}$.

4.4 Conclusion

The sliding and bouncing motion of a bubble interacting with an inclined wall have been introduced. PIV experiments were used to visualize vortex production in the bubble wake and the main differences between the two regimes were discussed. In the next chapter, the transition between the sliding and the bouncing is discussed.

Chapter 5

On the conditions for the sliding-bouncing transition for the interaction of a bubble with an inclined wall

In this chapter the condition of transition between the sliding and bouncing motions for a bubble interacting with an inclined wall is studied experimentally. The results of this chapter are presented in the same way as the paper that has been published in the Physical Review Fluids (Phys. Rev. Fluids 1, 032201(R), published 12 July 2016).

5.1 Abstract

In this study, we analyze the interaction of a single rising bubble with an inclined wall. We conduct experiments considering different liquids and bubble sizes, to cover a wide range of Reynolds and Weber numbers, with wall angles from nearly horizontal to nearly vertical. For all cases, the bubble initially collides with the wall; after the initial interaction, in accordance with Tsao and Koch (1997), the bubble either steadily slides on the wall or ascends colliding

repeatedly with it. Considering a force balance for the bubble motion on the wall, we propose a set of conditions for the transition from sliding to bouncing which is validated with the present and previous data.

5.2 Introduction

The study of two phase bubbly flows is largely justified by the numerous engineering applications and natural phenomena in which such flows occur. Significant advances have been reached in recent years due to the mature understanding of the hydrodynamic forces that affect the motion of single bubbles ascending in Newtonian liquids (Magnaudet and Eames, 2000). There is a clear understanding of the effects of viscous and inertial forces around interacting bubbles(Hallez and Legendre, 2011). Conversely, despite their ever-presence, the understanding of wall effects is still modest.

The interaction of ascending bubbles with vertical walls has been studied by several authorsTakemura and Magnaudet (2003); De Vries et al. (2002); Moctezuma et al. (2005); Figueroa-Espinoza et al. (2008). Similar to the case of bubble pair interactionsLegendre et al. (2003), the force between the bubble and the wall transitions from repulsive to attractive as the Reynolds number increases Takemura and Magnaudet (2003). When the wall attracts the bubble, it is possible to observe repeated bouncing De Vries et al. (2002); Moctezuma et al. (2005). According to De Vries et al. (2002) the bounce and rebound are affected by the wake behind the bubble. The process of bubble bouncing against a horizontal wall was analyzed in detail by Zenit and Legendre Zenit and Legendre (2009); they identified the conditions for rebound, as opposed to arrest, considering the dependence of the coefficient of restitution with the Stokes and capillary numbers. For the interaction of a bubble with an inclined wall, an interesting phenomena occurs: the motion of the bubble can either be repeated bouncing (as for a vertical wall) or steady sliding. The same bubble-fluid combination can exhibit the two behaviors; the type of motion observed is determined by the inclination of the wall. Tsao

and Koch Tsao and Koch (1997) originally reported this phenomenon. They proposed the transition occurred for a single value of the Weber number, but did not explain the physical process for the transition fully.

The sliding motion of bubbles on inclined walls has been studied to some extent. Aussillous and Quéré (2002) proposed scalings for the wall velocity, considering different regimes of bubble deformation; however, they restricted their analysis for nearly horizontal walls. The bouncing motion of bubbles on a wall has been addressed mainly for the case when the wall is vertical. De Vries et al. (2002) conducted flow visualization of the process and concluded that the bubble wake significantly influences the rebound off the wall.

In the present study, we investigate experimentally the motion of high Reynolds and moderate Weber number bubbles interacting with an inclined wall, closely following the original investigation by Tsao and Koch (1997). Unlike them, we substantially extend the range of parameters by considering different fluids (with different viscosities, densities and surface tensions) and bubble sizes. Based on this wider perspective, we are able better characterize the phenomena and explain the physical mechanism that leads to the transition from sliding to bouncing.

5.3 The physical conditions for the transition from sliding to collisional modes

Clearly, from the data shown in Table 2.1 and in Fig.2.2, the critical angle for the transition varies for each liquid-bubble combination. The angles do not seem to correlate with either Re_{term} or We_{term}. Tsao and Koch (1997) reported that the transition occurred for $We_{wall} = 0.4$, which implies that the transition is a result of the deformability of the bubble. Figure 5.1 shows a map of Re_{wall} as a function of We_{wall} for all the experiments conducted in this investigation. Clearly, a single value of either Re_{wall} or We_{wall} that characterizes the transition for all cases cannot be identified. Also from Table 2.1 and Fig.2.2, the transition

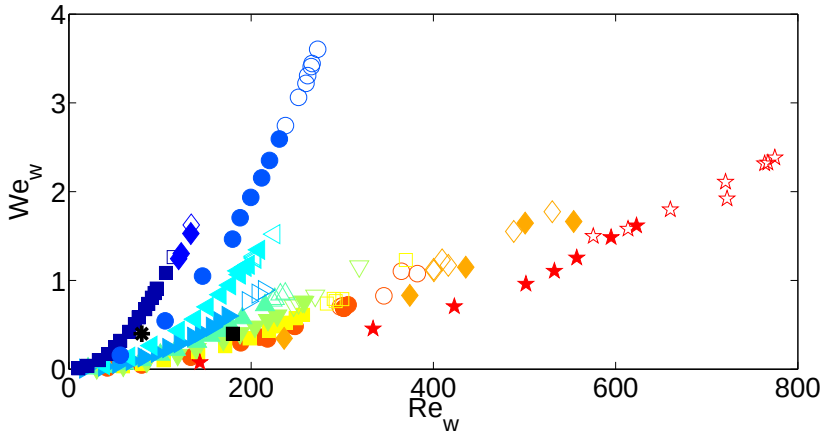

Figure 5.1: Map of wall Reynolds, Re_{wall}, and Weber, We_{wall}, numbers showing all the experiments conducted in this investigation. The symbols are according to Table 2.1. In all cases, the filled and empty symbols show the experiments in which sliding or bouncing was observed, respectively. The black squares, (■), show the data from Tsao and Koch (1997); the (∗) and (×) symbols are results from Takemura and Magnaudet (2003) and De Vries et al. (2002), respectively.

does not occur for a single value of θ_{trans}.

Note that, it is possible to also include the data corresponding to the transition to bouncing regime for vertical walls. Takemura and Magnaudet (2003) argued that the transition from wall-repulsion to wall-attraction was associated with the prevalence of inertial over viscous effects; hence, for such a case the transition would be characterized by a critical value of Re rather than We. The critical conditions from Takemura and Magnaudet (2003) and De Vries et al. (2002) are also shown in the figure.

5.3.1 Analysis

To understand the conditions for transition we consider a simple force balance for the bubble motion, in both parallel and perpendicular directions. From above, we recognize that both Re_{wall} and We_{wall} are important parameters to characterize the transition. In particular, the value of We_{wall} will determine the shape of the bubbles during their interaction with the wall Legendre et al. (2012).

To evaluate the influence of We_{wall} on the bubble shape, we shown typical bubble shapes

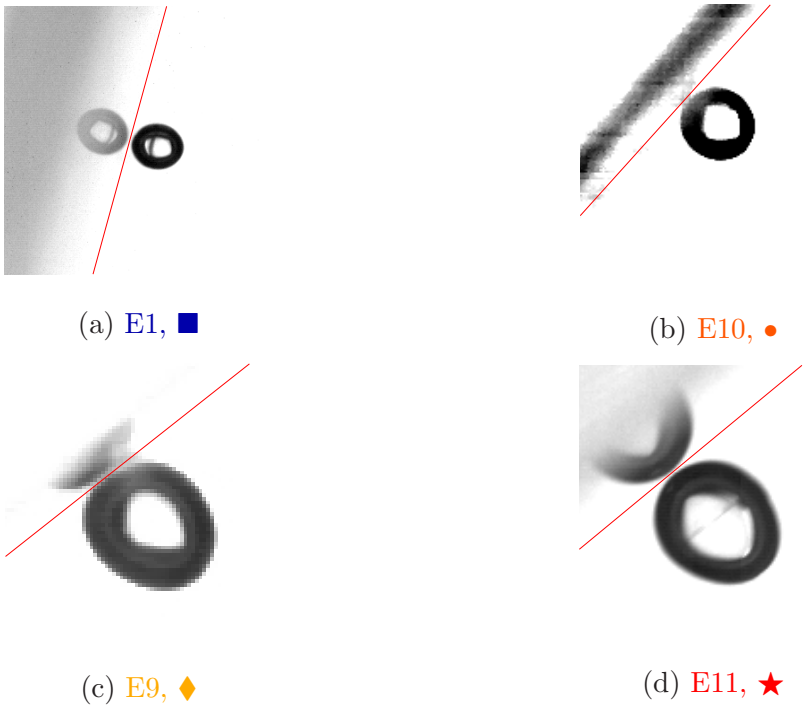

(a) E1, ■ (b) E10, ●

(c) E9, ♦ (d) E11, ★

Figure 5.2: Images for all bubbles in the sliding motion, at an angle just below the transition. The symbols are according to Table 2.1. (a) Exp.1, $Re_{wall} = 106$, $We_{wall} = 1.07$, $\theta = 75^o$; (b) Exp. 7, $Re_{wall} = 311$, $We_{wall} = 0.71$, $\theta = 50^o$; (c) Exp. 10, $Re_{wall} = 522$, $We_{wall} = 1.57$, $\theta = 40^o$; (d) Exp. 8, $Re_{wall} = 627$, $We_{wall} = 1.63$, $\theta = 40^o$. Images are shown on the same scale.

for the sliding regime, at angles slightly below θ_{trans}. Figure 5.2 shows snapshots of four experiments. In (a) and (b), the bubbles have $We_{wall} < 1.1$, for which the shape is close to spherical and the elongation is parallel to the wall resulting from gravity effects. The images (c) and (d), in the same figure, for which $We_{wall} > 1.5$ show bubbles that are largely deformed. It is curious to observe that, for this case the bubbles are elongated in the direction perpendicular to the wall, arguably resulting from inertial effects.

Let us now consider a force balance for a bubble both in the parallel and perpendicular directions. We first recognize that there is a gravitational force pushing the bubble to remain in contact with the wall. Second, we consider that there are viscous and/or inertial drag forces in the parallel wall direction. More importantly, we also argue that there is an inertial wall-repulsive force acting in the normal direction that results from the interaction of the bubble wake with the wall similar to what was previously discussed by De Vries et al. (2002). By

conducting a Schlieren-type visualization, these authors were able to observe the interaction between the bubble and vortex blobs from the wake. They argued that the interaction gave rise to a lift-type force that depended on the strength of the circulation of the vortex filament. They proposed that such force was proportional to $\rho V_{wall}^2 D_{eq}^2$. In our case, the force pushing the bubble away from the wall also results from both the vorticity in the wake (proportional to V_{wall}/D_{eq}) but also on the proximity of the wall. The wall provides the symmetry breaking mechanism and vorticity interaction is known to result in a repulsive effect(Legendre et al., 2003). Since we argue that the force arises from the wake, we conjecture that it also scales with $\rho V_{wall}^2 D_{eq}^2$.

Hence, balancing gravity with an inertial wake-induced wall force for the perpendicular direction, the criteria for bubble departure from the wall would be:

$$\rho V_{wall}^2 D_{eq}^2 \gtrsim \rho D_{eq}^3 g \cos\theta. \tag{5.1}$$

For the motion in the direction parallel to the wall, we can balance the buoyancy with a viscous drag force:

$$\mu D_{eq} V_{wall} \sim \rho D_{eq}^3 g \sin\theta. \tag{5.2}$$

Taking the ratio of Eqns.(5.1) and (5.2), we have:

$$Re_{wall} \gtrsim \cot\theta. \tag{5.3}$$

Therefore, we can say that when the wall Reynolds number angle surpasses a certain critical value, the bubble will not be able to remain sliding on the wall beyond the angle θ. This critical condition is expected to apply for spheroidal bubble for which the drag force is dominated by viscous effect Moore (1965). In Fig. 5.3, we replot our results separating the data in two different sets. In Fig. 5.3(a), the results corresponding to $We < 1.2$ are shown in terms of Re_{wall} as as function of $\cot\theta$ as suggested by Eqn.(5.3). The data clearly shows

that there is, indeed, a linear relation between Re_{wall} and $\cot\theta$ for the critical conditions. For the transition, our data can be closely fitted to

$$Re_{wall} = Re_0 + 310\cot\theta \tag{5.4}$$

where $Re_0 \approx 80$. In fact, the value of Re_0 coincides with the transition data for vertical walls from De Vries et al. (2002) and Takemura and Magnaudet (2003). The transition conditions reported by Tsao and Koch (1997) (black squares) are also in consistent agreement with Eqn.(5.4).

For bubbles with large values of We_{wall}, here $We_{wall} > 1.5$, we observed that the transition is not given by Eqn.(5.3). For such cases the bubbles are more deformed, as shown in Fig.5.2 (c) and (d). We conducted visualization experiments of the wake structure for this case. Figure 4.8g shows the flow around a sliding bubble for experiment E10 (see Table 2.1), for an angle slightly below the critical one ($\theta = 50^o$). Significant vortex shedding in the bubble wake is clearly observed; hence, in this case, the resulting drag would be dominated by inertial effects. Therefore, the force balance parallel to the wall is now:

$$\rho V_{wall}^2 D_{eq}^2 \sim \rho D_{eq}^3 g \sin\theta. \tag{5.5}$$

The ratio of Eqns.(5.1) and (5.5) suggests that, for the transition $\cot\theta$ should be constant. Figure 5.3(b) shows, again, Re_{wall} as a function of $\cot\theta$ but only for experiments with $We_{wall} > 1.5$. The transition is now clearly observed for a constant angle around $\cot\theta \approx 1$, corresponding to a value of $\theta \approx \pi/4$. These data cover a significant range of Re_{wall} (from 200 to 600).

It is important to note that the strength of the wake-induced lift and the drag force, and as a result the induced transition criteria, are probably affected by the Reynolds and Weber numbers corrections. Indeed, there are several factors that may affect the magnitude of these forces: the structure of the far wake, the vorticity production on the bubble surface, the

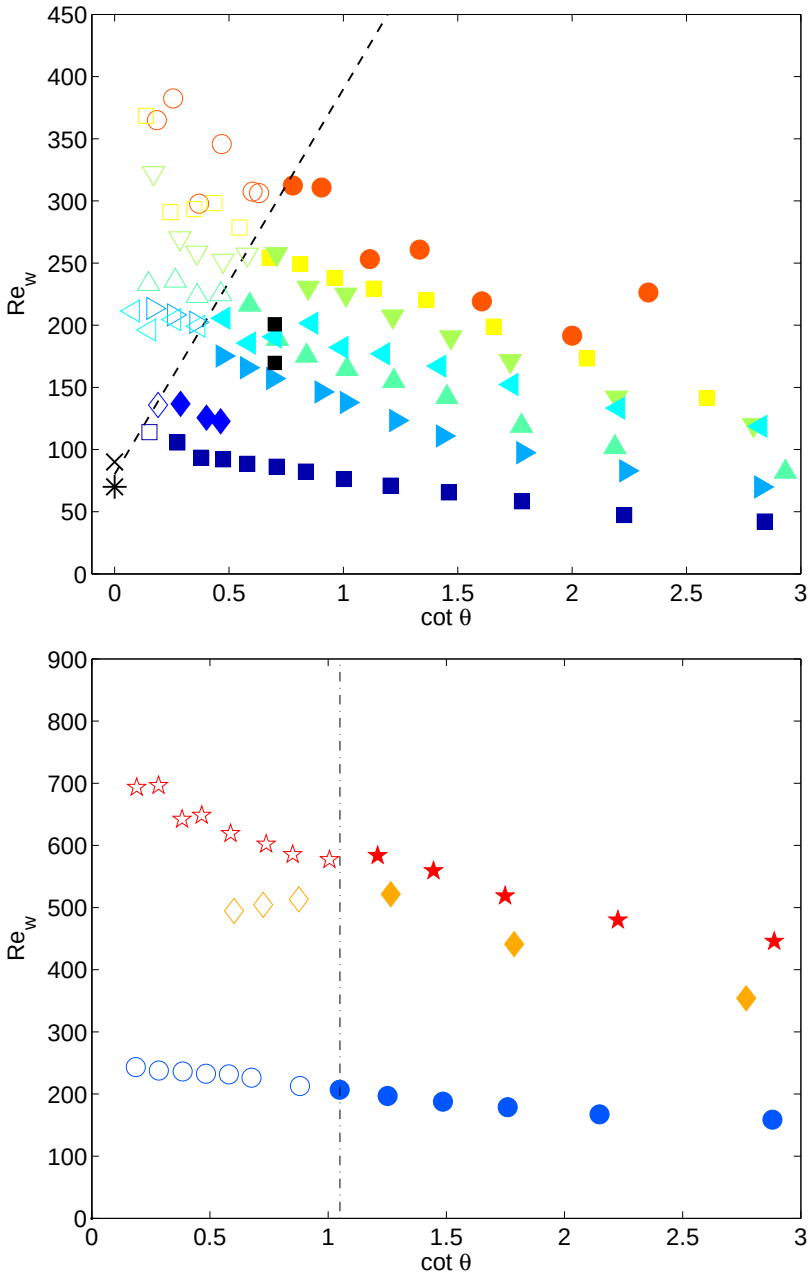

Figure 5.3: Conditions for transition: (a) $We_{wall} < 1.2$, Wall Reynolds, Re_{wall} as a function of $\cot\theta$; (b); $We_{wall} > 1.5$, Wall Weber, We_{wall}, as a function of inclination angle, θ. The symbols are according to Table 2.1. In all cases, the filled and empty symbols show the experiments in which sliding or bouncing was observed, respectively. The black squares, (■), are the data from Tsao and Koch (1997); the (∗) and (×) symbols are results from Takemura and Magnaudet (2003) and De Vries et al. (2002), respectively. The dashed line in (a) corresponds to Eqn.(5.4). The vertical dashed-dotted line in (b) corresponds to $\theta = 43.7^o$.

bubble shape, the interaction with the wall and even the possible presence of surfactants. The fact that our model prediction agrees well with the experiments indicate that such dependence of the forces with Re and/or We are not significant for the range of parameters explored here.

5.4 Conclusions

In this investigation we studied the interaction of an air bubble rising in a viscous fluid, during its interaction with an inclined wall. This particular problem had been addressed previously. Tsao and Koch (1994) first reported that, for air bubbles in water, the interaction changes from steady sliding to repeated bouncing at a certain angle. They argued that the condition for transition occurred at a certain critical Weber number, based in the sliding velocity, We_{wall}. Conversely, Takemura and Magnaudet (2003) claimed that, for a vertical wall, the transition would occur for a certain critical value of Re_{wall}. In this investigation, thanks to wider range of experimental conditions, we demonstrate that, instead, the transition results from the appearance of a wake induced lift. Furthermore, we found that there are two different regimes for the transition depending on the value of the Weber number (based on the wall velocity) which, in turn, determines the shape of the bubble, the wake structure and, therefore, the nature of drag force (viscous or inertial) on it. To our knowledge, the physical conditions to determine the transition had not been explained to date. We plan to study both regimes, sliding and repeated bouncing, in detail in the future.

Chapter 6

Sliding and bouncing motion of a high-Re moderate-We bubble interacting with an inclined wall

6.1 Introduction

Following the justification of the transition between the sliding and bouncing regimes of motion, the sliding motion dynamics is studied first in this chapter. This study follows the investigation of Aussillous and Quéré (2002), where the sliding motion of spherical and pancake bubbles was described through a force balance. However, that study only dealt with small inclination angles ($\theta < 5°$), whereas the whole range of inclination from almost horizontal to nearly vertical is considered here. The steady sliding velocity evolution will be observed for all the experimental conditions of Table 2.1 and inclination angles lower than the associated transition angle. Note that for this range of experimental data, the pancake shape reported by Aussillous and Quéré (2002) is not observed here.

Then, when the force balance along the normal direction involves a normal buoyancy force larger than the induced wake lift force, the bubble cannot remain sliding against the wall.

What is observed, instead, is that the bubble bounces periodically against the wall. This time-average steady motion is characterised by a constant bouncing amplitude and period. To generate this motion, the attractive buoyancy force has to be balanced by the repulsive lift force effect. The physics responsible for the collisional type motion will be also reported here, as well as the evolution of the bubble dynamics with the inclination angle.

6.2 Sliding bubble velocity

As described before, if the inclination angle is smaller than a certain transition angle the bubble slides against the wall with a constant velocity after a collision and a transient phase. Despite the apparent simplicity of the phenomenon, few authors have studied it. The range of experimental conditions considered in the present investigation should give us an extended panorama of the mechanics of the sliding bubbles.

The evolution of the steady sliding velocity with the inclination angle is shown in Figure 6.1 for all the experimental conditions of Table 2.1 (reported in Table 2.1). For all experimental conditions, the bubble-wall velocity increases monotonically with the inclination angle.

To understand the sliding motion, we consider the force balance proposed by Aussillous and Quéré (2002) in the direction parallel to the wall. It is important to mention that Aussillous and Quéré (2002) only considered small inclination angles ($\theta \leq 6°$) whereas we report here sliding motions for inclination angles up to 75°. As the bubble slides against the wall, it is driven upward by the buoyancy force ($F_{buoyancy} \sim \rho g D_{eq}^3 sin(\theta)$) and the drag force balances the gravity. Apart from the drag force resulting from the friction of the liquid, here after referred as Stokes force, the flattening of the bubble interface close to the wall generates an additional resistance to the bubble motion (see Figure 6.2). Indeed, when the bubble is deformable, it flattens against the wall during its sliding motion, because of the normal buoyancy action. A lubrication film is then formed. The associated force will be referred as lubrication force.

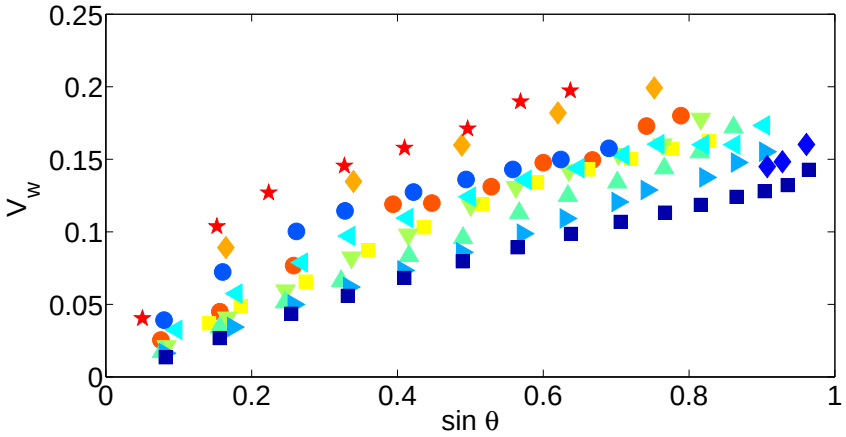

Figure 6.1: Sliding bubble velocities, V_{wall}, as a function of $sin\theta$, where θ is the inclination of the wall with respect to the horizontal direction, for all the experimental conditions of Table 2.1 are plotted according to the corresponding symbol codes.

The scaling of the Stokes force is

$$F_{Stokes} \sim \mu V_{wall} D_{eq} \tag{6.1}$$

The lubrication force is usually scaled as (Aussillous and Quéré (2002)):

$$F_{lubrication} \sim \frac{\mu V_{wall}}{h_{film}} l_{film} \lambda \tag{6.2}$$

where h_{film} is the thickness of the liquid film, l_{film} the length of contact between bubble interface and the liquid film. λ is the length of curved part of the bubble interface starting from the bubble edge to the interface in contact with the liquid film. To obtain an expression for h_{film} and λ, the flow in the liquid film during the sliding motion of the bubble is considered. The balance between the capillary force, resulting from the interface deformation by the lubrication film, and the viscous force applied to the flow in the liquid film gives the relation:

$$\frac{\mu V_{wall}}{h_{film}^2} \sim \frac{\sigma \kappa}{\lambda} \tag{6.3}$$

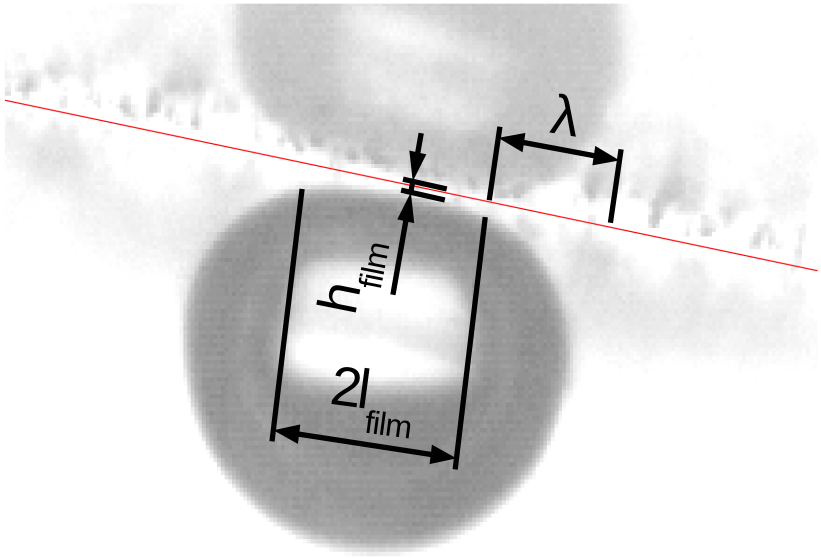

Figure 6.2: Illustration of the parameters of scaling of the lubrication force, for a 2.8 mm diameter bubble in experimental conditions E5 and a wall inclination of 10°.

where κ^{-1} is the capillary length. A second relation between both parameters is obtained through the balance of the Laplace pressure for the static bubble and the sliding bubble:

$$\kappa \sim \frac{h_{film}}{\lambda^2} \tag{6.4}$$

Considering these two relations, the expression of h_{film} and λ can be obtained and integrated in the expression of $F_{lubrication}$:

$$F_{lubrication} \sim \sigma \, l_{film} \, Ca_{wall}^{2/3} \tag{6.5}$$

where $l \sim D_{eq}^2 / \sqrt{\frac{\sigma}{\rho g}}$ is the length of contact between the bubble interface and the liquid film. Ca_{wall} is the capillary number considering the sliding velocity of the bubble ($Ca_{wall} = \frac{\mu V_{wall}}{\sigma}$). As a result, the balance of forces acting on a sliding bubble is given by the following scaling

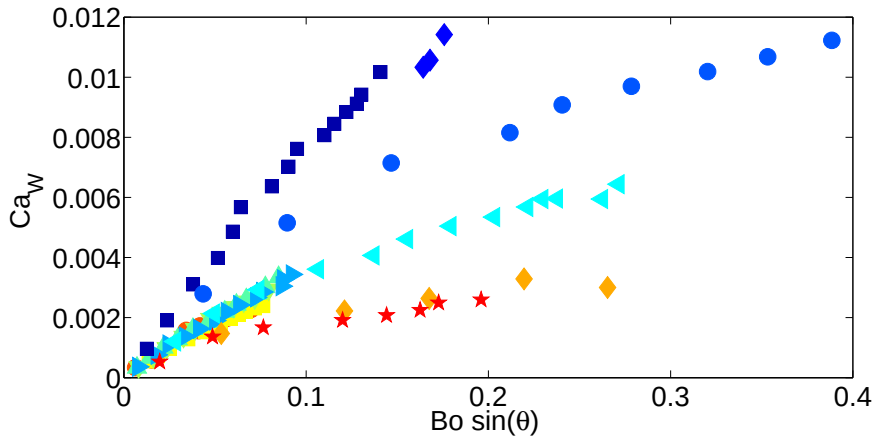

Figure 6.3: Map of wall capillary number, Ca_{wall}, and projected Bond number, $Bo\,sin\,\theta$, calculated for the experimental conditions of Table 2.1 and plotted according to the corresponding symbol codes. The blue and cyan continuous lines correspond to a fit of the contaminated and clean bubbles data respectively with a linear trend. This figure represents the Stokes force term as a function of the buoyancy term in equation (6.6)

law (Aussillous and Quéré (2002)):

$$\boldsymbol{a}\,Ca_{wall} + \boldsymbol{b}\,Ca_{wall}^{2/3}\sqrt{Bo} \sim Bo\,sin(\theta) \tag{6.6}$$

where $Bo = \dfrac{D_{eq}^2 \rho g}{\sigma}$ is the Bond number whereas **a** and **b** are constant, that can be inferred by a fit of the experimental results. From left to right, the first term of the equation represents the Stokes force, the second term is the lubrication force and the last one is the buoyancy force. If the Stokes force dominates over the lubrication force, a linear relation should exist between Ca_{wall} (respectively $\sqrt{Bo}\,Ca_{wall}^{2/3}$ if the lubrication force dominates over the Stokes drag) and $Bo\,sin(\theta)$. In Figure 6.3 (respectively Figure 6.4) the Stokes drag term (respectively lubrication term) is plotted as a function of the buoyancy term. Comparing both graphs, a closer fit to linear evolutions as well as a better collapse of all the data is obtained with the Stokes drag. Hence the sliding bubble motion is more likely to be controlled by the Stokes drag for these experiments. However, a more detailed analysis of Figure 6.3 is necessary to understand the sliding motion.

Indeed, a progressive departure between the linear trend and the experimental data is ob-

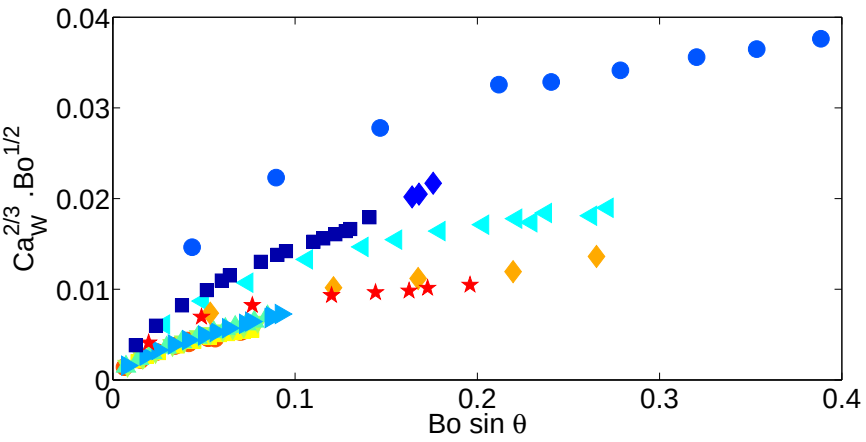

Figure 6.4: Evolution of $Ca_{wall}^{2/3} \times Bo^{1/2}$ as a function of the projected Bond number, $Bo\,sin\,\theta$, calculated for the experimental conditions of Table 2.1 and plotted according to the corresponding symbol codes. This figure represents the lubrication force term as a function of the buoyancy term in equation (6.6)

served in Figure 6.3 as the value of $Bo\,sin(\theta)$ increases. This gap is larger for experiments with large values of We_{wall}. Large values of We_{wall} are associated to large deformations of the bubble. Hence, to analyse this evolution of behavior, images of the sliding bubble shapes in experiment E3 are presented in Figure 6.5 for different inclination angles. For low inclination angles, the shape of the bubble is dominated by the action of the gravity as the major axis of the bubble is parallel to the wall and the minor axis is perpendicular to it. The compression acting on the bubble comes from the normal buoyancy force.

For larger inclination angles, when the bubble acquires a significant inertia it begins to elongate perpendicularly to the wall. Hence if the fluid stress on the bubble interface due to the bubble inertia becomes larger than the normal buoyancy force, the bubble passes from spherical to distorted shape. This regime, that will be referred as inertial motion, can be characterised by a larger bubble axis perpendicular to the wall than parallel to it. In Figure 6.3, the experimental data corresponding to this regime do not follow the linear trends because equation (6.6) is no longer applicable.

The transition from gravity-dominated to inertia-dominated deformation is obtained through the introduction of a new definition of the aspect ratio of the bubble. Instead of using the

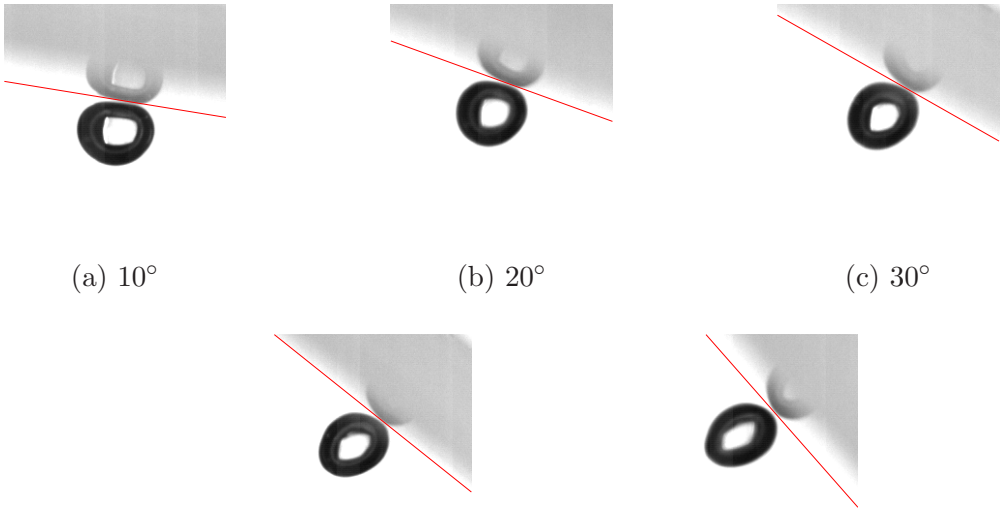

(a) 10° (b) 20° (c) 30°

(d) 40° (e) 50°

Figure 6.5: Images for the sliding bubbles shape evolution at different inclination angles in experimental conditions E3. (a) $Re_{wall} = 59$, $We_{wall} = 0.04$, $D_{eq} = 1.7$ mm, (b) $Re_{wall} = 119$, $We_{wall} = 0.16$, $D_{eq} = 1.7$ mm, (c) $Re_{wall} = 169$, $We_{wall} = 0.33$, $D_{eq} = 1.7$ mm, (d) $Re_{wall} = 204$, $We_{wall} = 0.48$, $D_{eq} = 1.7$ mm, (e) $Re_{wall} = 228$, $We_{wall} = 0.60$, $D_{eq} = 1.7$ mm. The subcaption reports the corresponding inclination angle. Images are shown with the same scale.

major and minor axis, we consider the axis parallel and perpendicular to the wall:

$$\chi_{wall} = \frac{Axis_{\parallel}}{Axis_{\perp}} \tag{6.7}$$

Therefore, the transition between regimes is characterised by a wall aspect ratio $\chi_{wall} > 1$ for gravity-dominated shape regime, whereas $\chi_{wall} < 1$ is observed in inertia-dominated shape regime of deformation. In Figure 6.6, we plot χ_{wall} as a function of the corresponding We_{wall} for all the experiments. Figure 6.6 clearly shows the two observed regimes. In the following sections we will analyse the two regimes separately.

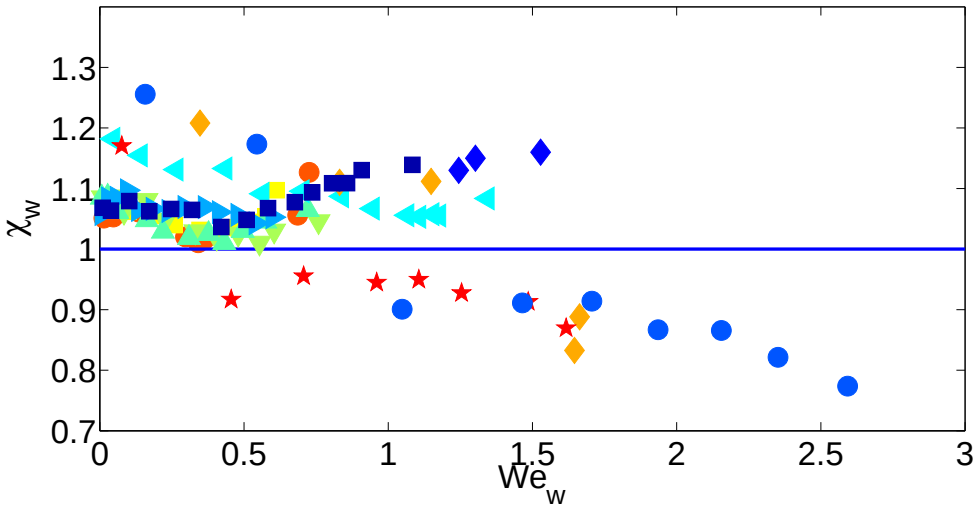

Figure 6.6: Evolution of the wall aspect ratio, χ_{wall}, defined in equation 6.7 as a function of the wall Weber number, We_{wall}, for all experimental conditions of Table 2.1 plotted according to the associated symbol codes. The criteria of sliding regime transition, $\chi_{wall} = 1$ is plotted in blue line.

6.3 Analysis

6.3.1 Gravity-deformation regime

As the shape of the bubble is controlled by the action of the gravity, the Stokes force can be scaled as a viscous force and according to equation (6.6) without the lubrication force results in a linear relation between $Bo\,sin(\theta)$ and Ca_{wall} so a description of the sliding bubble motion is given by:

$$Ca_{wall} \sim Bo\,sin(\theta) \tag{6.8}$$

In Figure 6.9 the evolution of Ca_{wall} as a function of $Bo\,sin(\theta)$, is shown, considering only the data corresponding to $\chi_{wall} > 1$. A good fit of the experimental data with linear trends is observed. Note that two different linear trends are shown and that a progressive gap is observed between the experimental results and the linear trend for large values of $Bo\,sin(\theta)$. We need to consider all the experimental parameters to understand the results. Hence, the effect of bubble contamination will be observed. As commented in Chapter 2, the presence of contamination can be studied by comparing the experimental terminal drag coefficient with

the correlation of Schiller and Naumann (1933) and Maxworthy et al. (1996) in Figure 6.8. We find that the terminal drag coefficients of large bubbles (experiments E3, E5, E9 and E11) agree well with the Schiller and Naumann (1933) expression. Consequently a strong contamination of the interface is suggested, except for E3 that corresponds to silicon oil. Indeed, according to Zenit and Magnaudet (2008), silicon oils are non-polar. Therefore the surface of the bubble remains clean unlike the other liquids used. As explained before, the absence of impurity on the bubble interface produces a different structure of flow around the bubble and so a different Stokes drag intensity is observed. Schiller and Naumann (1933) proposed a correction of the drag coefficient corresponding to solid spherical particle at intermediate Reynolds number ($Re < 800$), which can be interpreted as an immobile interface or a contaminated bubble:

$$Cd_{Shiller} = Cd_{Stokes}\left(1 + 0.15\, Re_{term}^{0.687}\right) \tag{6.9}$$

with Cd_{Stokes} being the drag coefficient of a spherical particle in the Stokes regime. In order to separate the effects of the interface contamination from the effect of the presence of an inclined wall on the bubble dynamics, we apply the Shiller based correction to the experimental data of the terminal conditions with a fitting parameter adjusted in order to align the corrected results with the model of Maxworthy et al. (1996):

$$Cd_{corrected} = \frac{Cd_{exp}}{(1 + 0.15 Re^{0.687}) k_d}, \tag{6.10}$$

where $k_d = 2$ is a fitting coefficient. We observe in Figure 6.8 the corrected drag coefficients, plotted in empty symbols, align well with the data of clean bubble.

The capillary number represents the ratio between the viscous force and the surface tension. In the case of a sliding bubble (see previous force balance and equation (6.6)) the viscous force comes from the drag force. Hence, in order to eliminate the effect of contamination of the liquid from the sliding dynamics and more particularly on the experimental Ca_{wall}, we

apply the previous correction to the experimental data:

$$Ca_{w\,corrected} = Ca_{w\,exp}\left((1 + 0.15Re_{wall}^{0.687})\,k_d\right) \tag{6.11}$$

The resulting data are plotted in Figure 6.9 in empty symbols. The corrected data agrees now with the results for clean bubbles corresponding to experiments E1, E2 and E3. Hence, we can conclude that the evolution of Ca_{wall} observed for these experimental data with the cyan linear trend results from the contamination of the liquid. Yet a gap is still observed with the linear trends for large values of $Bo\,sin(\theta)$ that can not be attributed to the contamination. Accordingly, the effect of the bubble deformation is now considered. The drag coefficient corrections proposed by Moore (1965) can be used to isolate the effect of deformation from the bubble dynamics. Accordingly, we correct now the experimental data of the terminal drag coefficient as:

$$Cd_{corrected} = \frac{Cd_{exp}}{G(\chi)}, \tag{6.12}$$

and the wall capillary number as:

$$Ca_{w\,corrected} = Ca_{w\,exp}\,G(\chi_{wall}) \tag{6.13}$$

where $G(\chi)$ is the first order correction of the drag force for the bubble deformation when the Reynolds number increases which is given by (Moore (1965)):

$$G(\chi) = \frac{1}{3}\chi^{4/3}(\chi^2-1)^{3/2}[(\chi^2-1)^{1/2} - (2-\chi^2)sec^{-1}\chi]/[\chi^2 sec^{-}1\chi - (\chi^2-1)^{1/2}]^2 \tag{6.14}$$

Based on the potential flow theory, the energy dissipation on an ellipsoidal bubble is calculated analytically. The expression of the drag coefficient as a function of the aspect ratio of the ellipsoid is then deduced from the drag force. As observed in Figure 6.8, the corrected values now agree well with Maxworthy's expression. The effect of the bubble deformation is then well separated from the bubble dynamics through this correction. Consequently, the

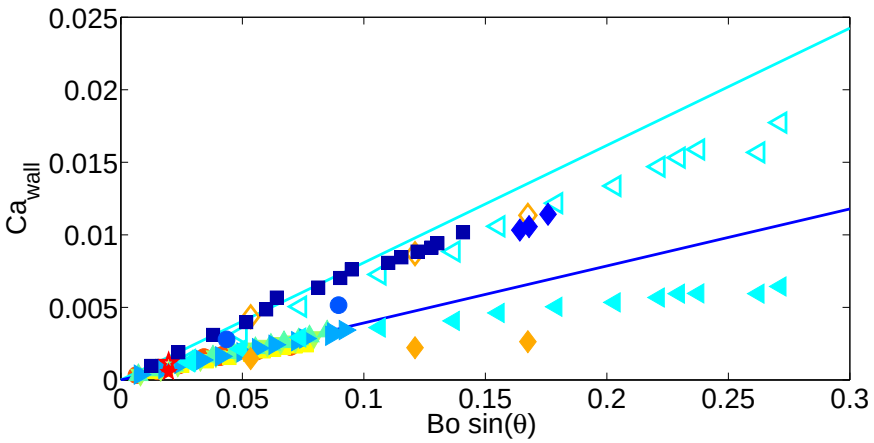

Figure 6.7: Map of wall capillary number, Ca_{wall}, and projected Bond number, $Bo\,sin\,\theta$, calculated for the experimental conditions of Table 2.1 that belong to the viscous regime ($\chi_{wall} > 1$) and plotted according to the corresponding symbol codes. The blue and cyan continuous lines correspond to a fit of the contaminated and clean bubbles data respectively with a linear trend. This figure represents the Stokes force term as a function of the buoyancy term in equation (6.6). In empty symbols are plotted the data corrected according to equation (6.10) or equation (6.12).

wall capillary number fits well with the linear relation of clean bubbles. Thanks to these corrections, an agreement with equation (6.8) is obtained for all the experimental data of the gravity-dominated shape regime of deformation. As for the existence of two linear trends, it is indeed associated to spherical sliding bubbles on one hand (blue line) and deformed sliding bubbles on the other hand (cyan line). More explicitly,the cyan line correponds to the force balance of (6.8), whereas the cyan line corresponds to the force balance (6.6) where the lubrication force term is transformed into an additive drag through the deformation corrections (6.13).

Given that the Stokes force dominates, we can consider the drag coefficient expression for a rising bubble in presence of a wall developed by Kok (1993). He calculated an analytical expression of the drag coefficient of a pair of bubbles rising symmetrically in a quiescent fluid, considering potential flow. The resulting drag coefficient was obtained by multiplying the drag coefficient of a free rising bubble at high Reynolds number with a correction term

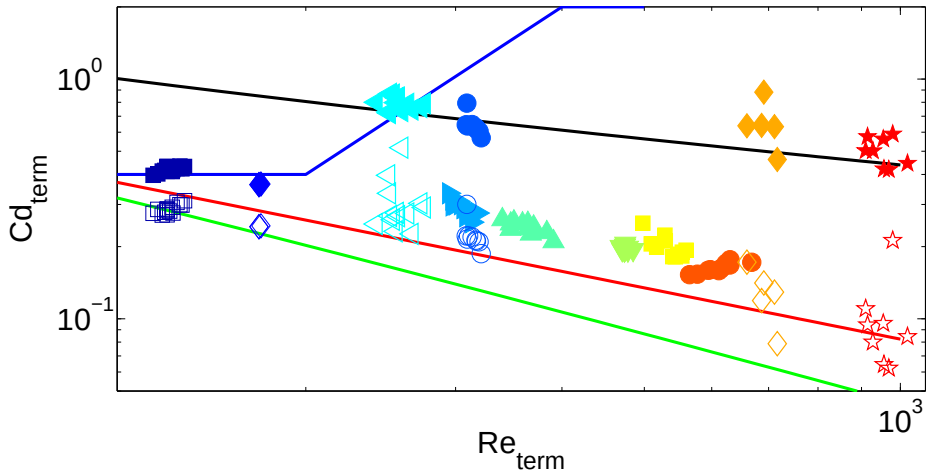

Figure 6.8: Map of terminal drag coefficient, Cd_{term}, and terminal Reynolds number, Re_{term}, calculated thanks to equation (4.3) for the experimental conditions of Table 2.1 and plotted according to the corresponding symbol codes. The green red and black continuous lines correspond to Moore (1965), Maxworthy et al. (1996) and Schiller and Naumann (1933) expressions respectively. For the green line an aspect ratio of 1 is taken in the corresponding drag coefficient expression proposed by Moore (1965). In Magenta line a fit of the Moore (1965) expression on some experimental data is presented. The drag coefficient evolution, taking into account the shape evolution of the bubble given by Moore (1965) is shown in orange, cyan and blue lines for $Mo = 5 \times 10^{-9}$, $Mo = 1 \times 10^{-9}$ and $Mo = 2 \times 10^{-11}$ respectively. The empty symbols corresponds to the data corrected according to equation (6.10) or equation (6.12).

depending on the dimensionless distance between the bubble and its image:

$$Cd = \frac{48}{Re}\left(1 + s^3 + \frac{3}{4}s^6 + ...\right) \tag{6.15}$$

where $s = \dfrac{h}{D_{eq}}$, where h is the distance between the bubble and the wall. Figueroa-Espinoza et al. (2008) have shown that for the case of a bubble confined between two walls, in addition to the inviscid contribution of the potential-flow, the production of vorticity at the wall also contributes to the drag force. They inferred the viscous contribution from direct numerical simulations of the flow of a static spherical bubble placed in between two moving walls. In agreement with Legendre (2007), the viscous contribution was established as a function of the maximum vorticity (Ω_{max}) produced by the bubble motion on the wall. The contribution was then added to the inviscid potential flow correction in the expression of the drag coefficient. Its dependence with the dimensionless distance s showed good agreement with experimental data. As a first approximation of this contribution for the case of a single wall, we consider half the contribution proposed by Figueroa-Espinoza et al. (2008) for a bubble rising in a channel:

$$\frac{Cd}{Cd_{Moore}} = \left(1 + \phi_{walls} + \left(\frac{16\omega^*_{max}}{Re}\right) + ...\right), \tag{6.16}$$

where ϕ_{walls} is the term given by the potential flow theory and representing the effect of the walls on the drag coefficient of a high Reynolds number bubble. $\dfrac{16\omega^*_{max}}{Re}$ is the drag coefficient expression as a function of the vorticity production proposed by Legendre (2007) for large Reynolds numbers. $\omega^*_{max} = \dfrac{3}{8}s^3 Re$ is the value obtained numerically by Figueroa-Espinoza et al. (2008) considering the presence of two walls. Hence, we propose to model the drag coefficient of a bubble sliding against a wall by:

$$\frac{Cd}{Cd_{Moore}} = \left(1 + s^3 + \frac{1}{2}\left(\frac{16\omega^*_{max}}{Re}\right) + ...\right) = (1 + 4s^3 + ...), \tag{6.17}$$

For the case of a sliding bubble, very close to the wall, the dimensionless distance is $s \sim 0.5$.

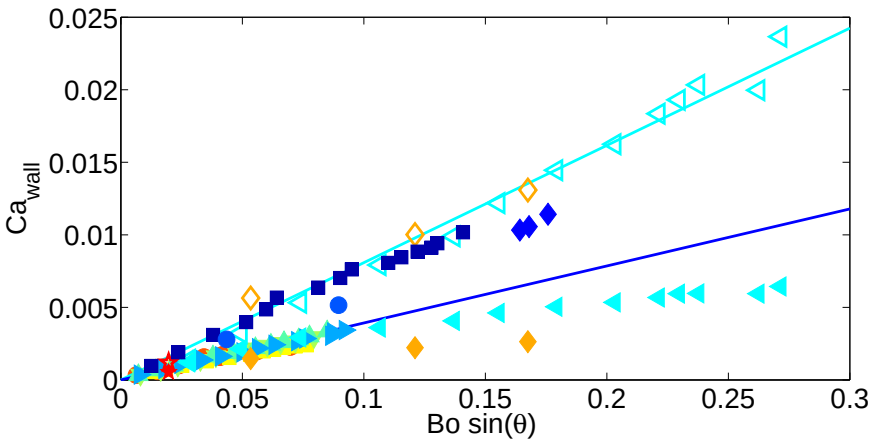

Figure 6.9: Map of wall capillary number, Ca_{wall}, and projected Bond number, $Bo\,sin\,\theta$, calculated for the experimental conditions of Table 2.1 that belong to the viscous regime ($\chi_{wall} > 1$) and plotted according to the corresponding symbol codes. The blue and cyan continuous lines correspond to a fit of the contaminated and clean bubbles data respectively with a linear trend. This figure represents the Stokes force term as a function of the buoyancy term in equation (6.6). In empty symbols are plotted the data corrected according to equation (6.10) or equation (6.12).

And taking $Cd_{Moore} \sim Cd_{Levich} = \dfrac{48}{Re}$, the analytical expression for the drag coefficient for a sliding bubble is simply:

$$Cd = \frac{73}{Re} \tag{6.18}$$

The resulting drag coefficient approximation is plotted in Figure 6.10. In this same figure we also plot the experimental drag coefficients of all the experiments inferred from the balance between the drag force and the tangential buoyancy force:

$$Cd_{wall} = \frac{4}{3}\frac{D_{eq} g sin\theta}{V_{wall}^2} \tag{6.19}$$

We apply equation (6.10) and equation (6.12) to the original experimental data to correct both contamination and deformation and plot the corresponding values in empty symbols. The analytic expression obtained for the drag coefficient is in agreement with the trend of the experimental drag coefficient of spherical sliding bubbles corresponding to the development hypothesis. Nevertheless, a constant gap exists that comes from the overvaluation of the

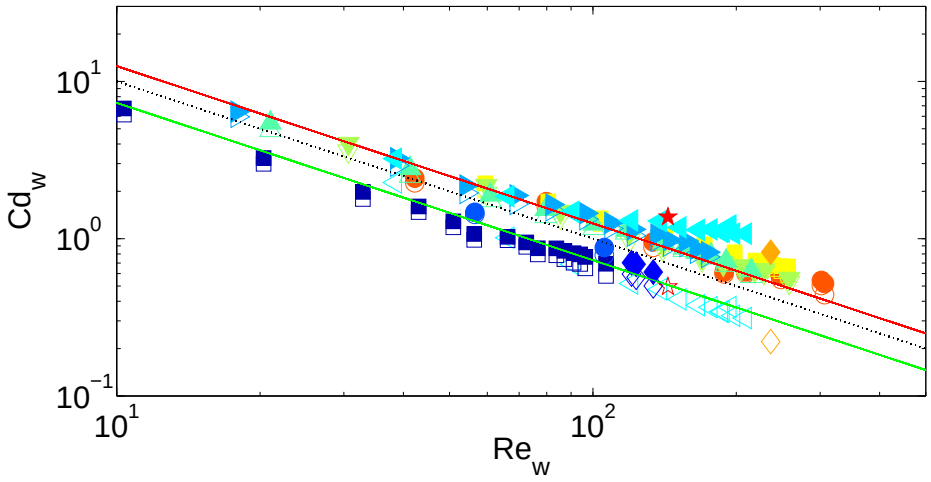

Figure 6.10: Map of wall drag coefficient, Cd_{wall} as defined in equation (6.19), and wall Reynolds number, Re_{wall}, calculated for the experimental conditions of Table 2.1 that belong to the viscous regime ($\chi_{wall} > 1$) and plotted according to the corresponding symbol codes. The green red and black lines correspond to equation (6.18), equation (6.20) and the empirical relation proposed by Tsao and Koch (1997) ($Cd_{wall} = \frac{100}{Re}$) respectively. In empty symbols are plotted the data corrected according to equation (6.10) or equation (6.12).

effect of the vorticity production at the wall based on the (Figueroa-Espinoza et al., 2008) relation and the number of wall. The evolution of the drag coefficient of spherical bubbles with respect to the Reynolds number is actually:

$$Cd_{wall} = \frac{k}{Re_{wall}}, \tag{6.20}$$

where $k = 125$. The drag coefficient of deformed bubbles are aligned with the theoretic trend (6.18). Yet, it is surprising that the drag coefficients of deformed bubbles are smaller than for the spherical bubbles. This phenomenon is attributed to a lower vorticity production along the wall when the bubble is deformed compared to the vorticity production of a spherical bubble.

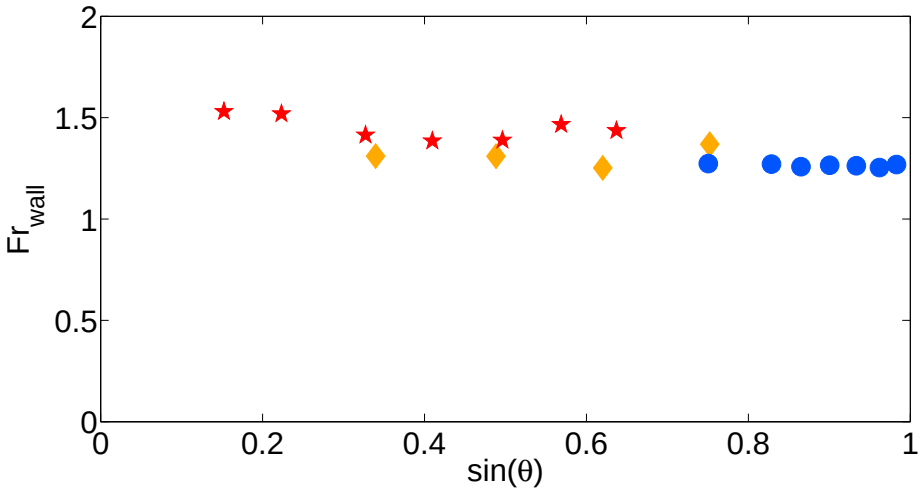

Figure 6.11: Map of wall Froude number, Fr_{wall} defined by equation (6.22), and $cos\,\theta$, calculated for the experimental conditions of Table 2.1 that belong to the Inertial regime ($\chi_{wall} < 1$) and plotted according to the corresponding symbol codes.

6.3.2 Inertial Regime

As discussed above, when the bubble motion acquires sufficient inertia it shape is such that $\chi_{wall} < 1$. In this case, the bubble appears nearly perpendicular to the wall. As a larger area is exposed to the flow we can expect a vortex detachment (see chapter 4)and the drag force to obey an inertial scaling. Considering that the drag force is balanced with the buoyancy we have:

$$\rho V_{wall}^2 D_{eq}^2 \sim \rho g D_{eq}^3 sin(\theta) \tag{6.21}$$

This expression can readily be written as:

$$Fr_{wall} = \frac{V_{wall}}{\sqrt{g D_{eq} sin(\theta)}} \sim constant \tag{6.22}$$

The Froude wall number (Fr_{wall}) is the ratio between the bubble inertia and the buoyancy. Figure 6.11 shows Fr_{wall} as a function of $sin\theta$ for the experiments for which $\chi_{wall} < 1$. For all the data, a nearly constant value Fr_{wall} is observed. Given that in this case inertial effects dominate due to the wake detachment induced by the deformation (4.8g), the corrections

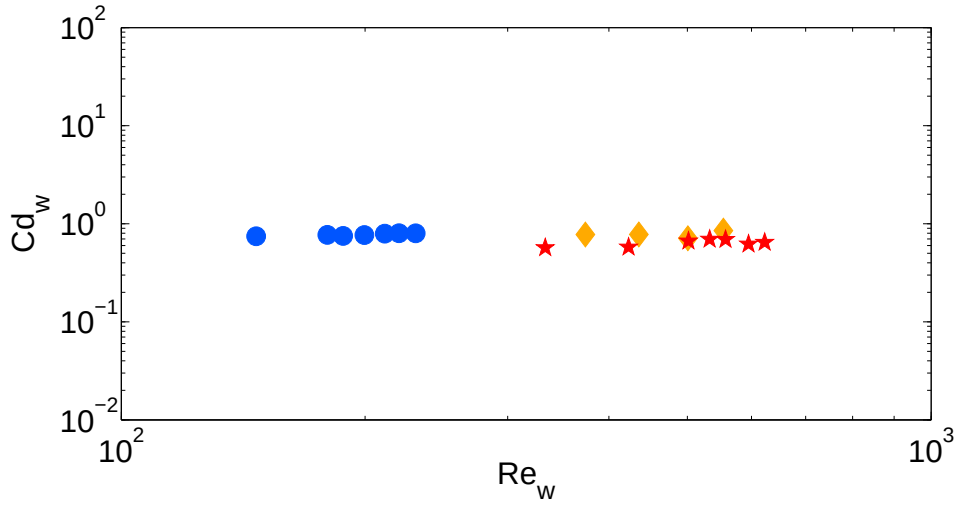

Figure 6.12: Map of wall drag coefficient, Cd_{wall} as defined in equation (6.19), and wall Reynolds number, Re_{wall}, calculated for the experimental conditions of Table 2.1 that belong to the inertial regime ($\chi_{wall} < 1$) and plotted according to the corresponding symbol codes. The vertical axis is the same as in Figure 6.10 to make possible a comparison between the two regime

for the contaminated bubble and the deformation discussed before are not applicable. Accordingly, considering the definition of the experimental drag coefficient, equation (6.19) we have:

$$Cd_{wall} = Fr_{wall}^{-2} \tag{6.23}$$

Therefore, for this case the drag coefficient is constant. Figure 6.12 shows the drag coefficient as a function of the Reynolds number, which clearly shows the $Cd_{wall} \sim constant$. A constant drag coefficient of approximately 0.7 is effectively observed for sliding bubbles in inertial regime. The data cover a wide range of Reynolds numbers (from 150 to 650 approximately). Therefore, the bubbles that belong to the inertial regime are controlled by a drag force independent of the inclination angle of the wall and the Reynolds number.

6.3.3 Conclusion

In this section we studied the sliding motion of bubbles for inclination angles lower than the transition angle. A first study of this configuration had already been presented by

Aussillous and Quéré (2002) but was restricted to low inclination angles ($\theta < 6°$). They proposed a simple force balance to describe the evolution of the sliding velocity with the inclination angle, considering the buoyancy force, the Stokes force and the lubrication force. Based on a wider range of experimental conditions and inclination angles, we found the existence of two regimes of sliding motion. Indeed when the inertia achieved by the bubble is large the bubble acquire a large deformation aligning perpendicularly to the wall. Based on an adapted definition of the aspect ratio considering the ratio of the parallel to the perpendicular axis, the transition occurred for $\chi_{wall} \sim 1$. For aspect ratios smaller than one, the bubble motion was controlled by a viscous drag force. In agreement with Aussillous and Quéré (2002), and considering equivalent diameters lower than the corresponding capillary length, no lubrication force acted on the bubble. As a result, a linear relation of the wall capillary number (Ca_{wall}) and the tangential Bond number ($Bosin(\theta)$) was observed. Given the experimental conditions of the study, both the bubble interface contamination and bubble deformation affected the results. By applying corrections of the viscous force based on the Schiller and Naumann (1933) and Moore (1965) corrections respectively, the data followed an identical linear tendency. A model of the drag coefficient of the sliding bubbles was proposed based on the additive contributions of the inviscid potential-flow drag correction proposed by Kok (1993) and the drag contribution due to the vorticity production on the wall (Figueroa-Espinoza et al. (2008)). The drag coefficient proposed agreed well with the experimental data of clean bubbles. For the cases where the wall aspect ratio was higher than one ($\chi_{wall} > 1$), the motion of the bubble resulted from a balance between an inertial drag force and the buoyancy. The force balance showed that the wall Froude number is constant for all angles. Consequently the drag coefficient was found to be constant and independent of the wall Reynolds number. The experimental data agreed well with these scaling arguments.

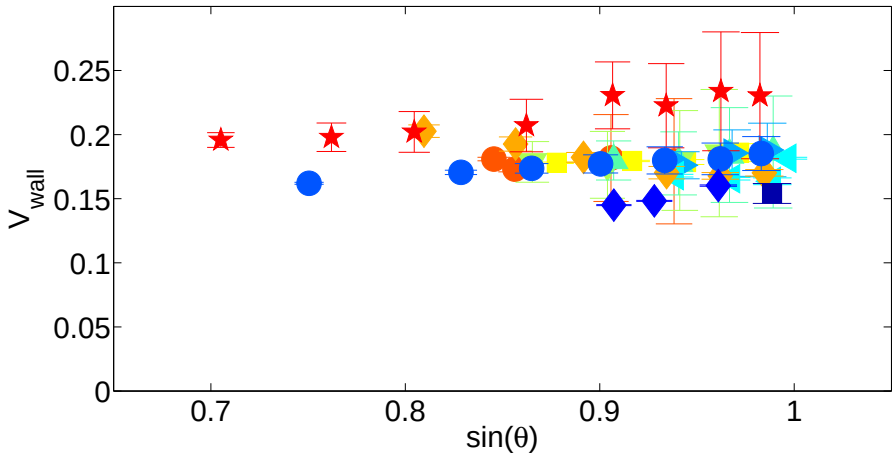

Figure 6.13: Mean tangential bubble velocities, V_{wall}, for the bubbles in the bouncing regime as a function of $sin(\theta)$, whith θ the inclination angle. As well, the error bars represent the standard deviation of the associated tangential velocity considering the bouncing motion. All data of Table 2.1 are presented with the corresponding symbol codes.

6.4 Bouncing motion of bubbles

Unlike when the bubble is sliding, the bubble never achieves a constant velocity when it bounces periodically. As a consequence, a mean time-average velocity will be considered to characterise the dynamics of the bubble. However, the mean normal velocity is zero. Hence, the bouncing dynamics of the bubble will be studied through the mean tangential velocity. This parameter is calculated considering several complete bounces, once a constant bouncing amplitude is observed. The mean tangential velocity of the collisional modes observed for the experimental conditions depicted in Table 2.1 is shown as a function of the inclination angle in Figure 6.13. The standard deviation of the tangential velocity, considering its variations during one bounce, is reported in the same figure. Data are color and symbol coded according to the description of Table 2.1.

The mean tangential velocity ranges between $150\,mm.s^{-1}$ and $220\,mm.s^{-1}$ so that a similar order of magnitude is found compare to the sliding motion. In contrast with the sliding motion velocities, the mean tangential velocities of the bouncing bubbles are nearly independent from the inclination angle. Also, the physical properties of the bubble-liquid system have small

influence on the dynamics of the bubble. In contrast, the standard deviation increases with the inclination angle. To understand the physics that engender such a behavior, the time evolution of the tangential velocity during one bounce is analyzed. The bubble-wall distance and the tangential velocity evolutions with the time are shown in Figure 6.14a and Figure 6.14b respectively, for a 1.6 mm diameter bubble in experimental conditions E6 (see Table 2.1) and an inclination angle of 60°. Full symbols are used to show the times in which the bubble is in contact with the wall. Empty symbols show the times of bouncing. The bubble-wall contact phase begins when the bubble impacts the wall and finishes when the tail detaches from the wall. The small decrease of tangential velocity observed during the contact phase is balanced by an equivalent increase observed during the bounce. The largest evolution of the bubble tangential velocity occurs during the bounce phase. The variation of the mean tangential velocity, reported in Figure 6.13, is generated during this phase. During the bounce phase, the bubble motion is controlled by the balance between the drag and the added mass forces, both aligned with the bubble path but in opposite directions; the buoyancy force, directed along the vertical direction, and the lift force, perpendicular to the bubble path. The physics of the lift force have been studied by De Vries et al. (2002). However, unlike his theory and in agreement with the Chapter 5, we consider here that the lift force is wall-repulsive. In Figure 6.15, the evolution of the tangential velocity of the same 1.6 mm diameter bubble in experimental conditions E6 with the time is shown for four different inclination angles (65°, 70°, 75°, 80°). The variation of the tangential velocity during one bounce increases with the inclination angle because of the effect of the lift force. Considering De Vries et al. (2002), the lift force scales as:

$$F_{lift} \sim \rho_l D_{eq}^2 V^2 \tag{6.24}$$

with D_{eq} is the equivalent diameter and V is the magnitude of the velocity. Actually, when the inclination angle increases, the bubble inertia increases too and tends toward the terminal conditions. As a consequence, the lift force magnitude becomes more important and both the deceleration and acceleration that it generates are more intense. This explains the almost

constant mean tangential velocity, as well as the increasing standard deviation when the inclination angle increases.

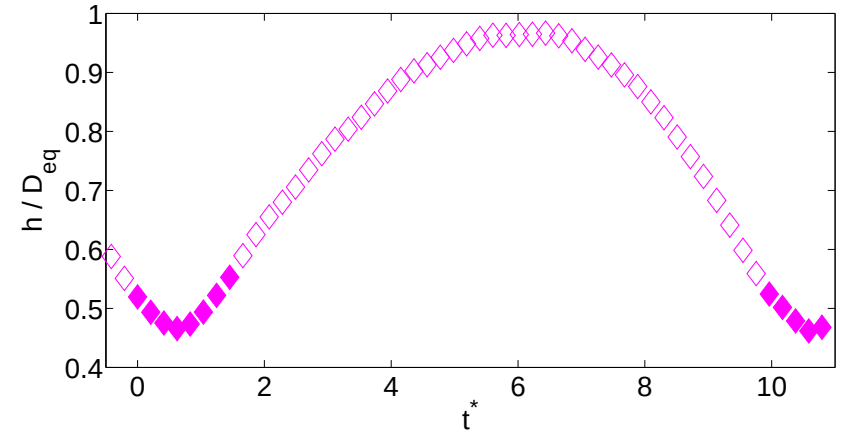

(a)

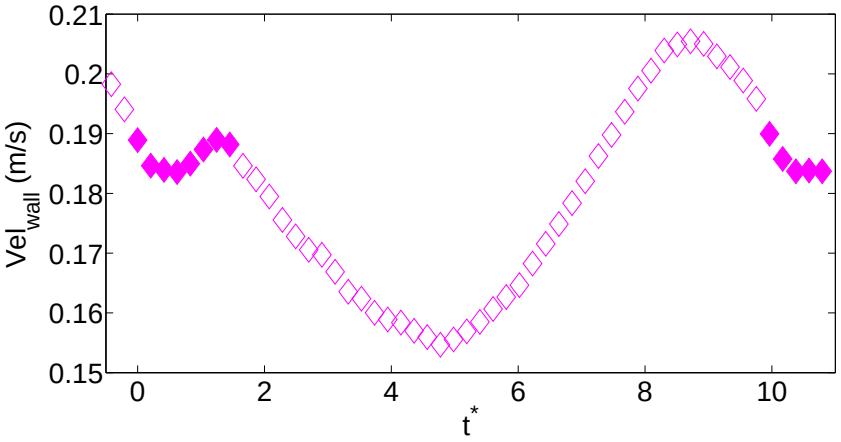

(b)

Figure 6.14: Steady bounce of a bubble for inclination angles larger than the transition angle. The steady motion of a 1.6 mm diameter bubble in experimental conditions E6, from Table 2.1, is reported for a 65° inclined wall. In empty symbol is reported the tangential velocity evolution of the bubble during the bounce phase, whereas the full symbols correspond to the contact phase. (a) dimensionless distance, h/D_{eq}, and (b) tangential velocity evolutions, V_{wall}, are shown for one steady bounce as a function of the dimensionless time, tV_{term}/D_{eq}.

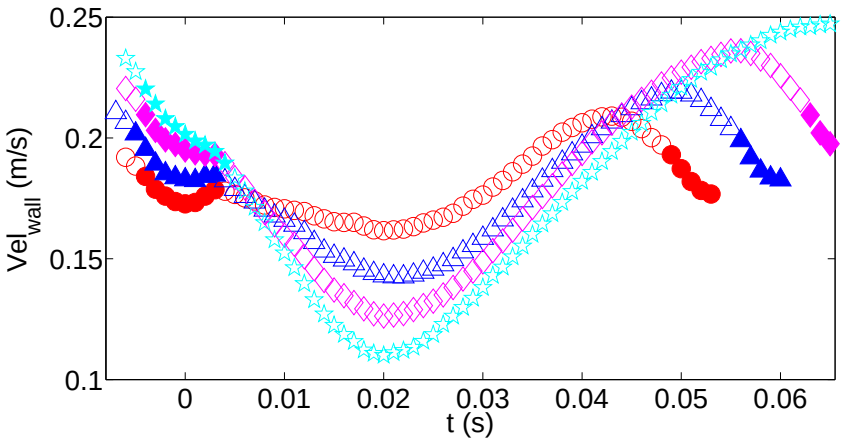

Figure 6.15: Steady bounce of a bubble for inclination angles larger than the transition angle. The steady motion of a 1.6 mm diameter bubble in experimental conditions E6, from Table 2.1, is reported for inclination angles of 65°, 70°, 75° and 80°. The associated data are represented in red, blue, magenta and cyan colors respectively. In empty symbol is reported the tangential velocity evolution of the bubble during the bounce phase, whereas the full symbols correspond to the contact phase. The tangential velocity evolution, V_{wall}, is shown for one steady bounce as a function of the dimensionless time, tV_{term}/D_{eq}.

6.5 Analysis

Considering the tangential velocity of the bouncing bubbles, the lift force significantly influences the resulting motion. However, if we consider the mean behavior of the bubble through a balance of force, the lift force is in the normal direction. The force balance in the tangential direction is:

$$\rho V_{wall}^2 D_{eq}^2 \sim \rho g D_{eq}^3 sin(\theta) \tag{6.25}$$

where V_{wall} is the mean tangential velocity. This balance results in a constant drag coefficient.

$$\frac{V_{wall}}{\sqrt{gD_{eq}sin(\theta)}} = Fr_{wall} = \frac{1}{\sqrt{Cd_{wall}}} \sim constant \tag{6.26}$$

However, compared to the sliding inertial bubbles, a much larger bubble deformation is generated when the bubble bounces.

In Figure 6.16, the drag coefficient of the bouncing bubbles, for the experimental conditions

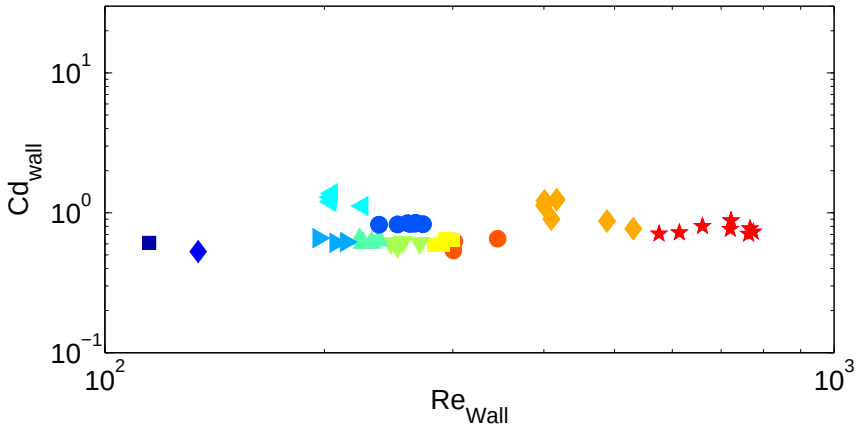

Figure 6.16: Map of the wall drag coefficient, Cd_{wall}, and wall Reynolds numbers, Re_{wall}, obtained for the bouncing motions of bubbles calculated thanks to equation (6.19) for the experimental conditions of Table 2.1 and plotted according to the corresponding symbol codes. The data reported correspond to the mean tangential velocities of the bubble for inclination angles larger than the transition angle. In empty symbols the corrected wall drag coefficient, considering either equation (6.10) or equation (6.12) are shown.

of Table 2.1, are plotted as a function of the wall Reynolds numbers with the corresponding symbols. As expected, a constant drag coefficient is observed. The value observed is the same as the constant drag coefficient of the inertial sliding bubbles:

$$Cd_{wall} \sim 0.7 \tag{6.27}$$

Hence the inertial nature of the bouncing motion is confirmed.

6.5.1 Conclusion

In this chapter, the dynamics of the bubble, considering inclination angles larger than the transition angle were studied. Accordingly, the inertia achieved by the bubble generates a lift force higher than the normal buoyancy force (see Chapter 5). Hence, the bubble bounces repeatedly against the wall instead of sliding. The tangential velocity evolution with the time during one bounce highlights the predominance of the lift force in the bubble dynamics. Through its wall-repulsive effect, the lift force regulated the tangential velocity so

that a global tangential velocity increase was generated during the bounce that compensates exactly the tangential velocity decrease associated to the bubble-wall impact. The balance of force used for the inertial sliding bubbles was applied successfully to describe the mean tangential motion of the bouncing bubbles. Accordingly a constant drag coefficient was obtained ($Cd_{wall} \sim 0.7$).

Chapter 7

Oblique collision of a bubbles at high Reynolds numbers

7.1 Introduction

In the previous chapters, the study have been focused on the steady behavior achieved by the bubble after impacting the wall and realising a few transient bounces. This chapter analyzes the process of impact of a bubble at its terminal state with an inclined wall. One possible approach to model the interaction is by a coefficient of restitution ϵ defined as:

$$\epsilon = |\frac{V_{depart}}{V_{approach}}| \tag{7.1}$$

where V_{depart} and $V_{approach}$ correspond to the particle velocity before and after the collision. This quantity has been introduced by Joseph et al. (2001) to lump in one parameter all the experimental results of collision of a solid particle against an horizontal wall in a viscous liquid. It has since been largely extended to a variety of particle-wall collisions. Yet, when the particle considered is a bubble, the understanding of the physics is, to our knowledge, limited to the case of rectilinearly rising bubble and horizontal wall (Zenit and Legendre (2009)). Accordingly, the present study is an extension of Legendre et al. (2005) and Zenit

and Legendre (2009) to consider the collision of bubbles with an inclined wall. The process is observed using a high speed camera within a large range of experimental conditions and inclination angles. A detailed description of the approach, collision and rebound processes from a dynamical and energetic perspective is included in the following section. Both normal and tangential coefficients of restitution are analysed.

7.2 Dynamics of the bubble-oblique wall interaction

The instantaneous evolution of the velocity, position and shape of a bubble during its interaction with an inclined wall were observed. To this end, collisions in experimental conditions E10 and E1 of Table 2.1 were recorded with a frame rate of 3000 images per second. As well, some experimental data of table 2.1 are considered but with the framing rate (1000 frames per second) used in Chapter 6. The experimental conditions used for this study are reported in Table 7.1. For all the interactions bubbles were injected from the bottom of the tank according to the sketch shown in Chapter 2. Hence, they impact the inclined wall after having reached their terminal conditions (V_{term} and χ_{term}). The inclination angles considered ranged from 5° to 80°.

In the present investigation, we observe free-rising bubbles, not only rectilinearly but also following zig-zag and helicoidal trajectories. These 2D and 3D trajectories together with the

Experiment	Composition %	ρ kg/m^3	μ $mPas$	σ mN/m	D_{eq} mm	Re_{term}	We_{term}	χ_{term}	Framing rate s^{-1}
E4, ▶	W-G 80-20	1045	1.555	70.2	1.7	305±7	1.9±0.09	1.26±0.04	1000
E6, ▲	W-G 85-15	1033	1.363	70.0	1.6	367±16	2.1±0.16	1.44±0.05	1000
E7, ▲	W-G 90-10	1021	1.165	70.6	1.6	469±14	2.5±0.15	1.63±0.08	1000
E8, ■	W-G 95-5	1009	1.038	70.8	1.7	536±21	2.6±0.20	1.58±0.07	1000
E10, ★	W 100	998	0.955	72.6	1.6	601±40	2.7±0.3	1.78±0.10	1000
E12, ●	W 100	998	0.955	72.6	2.0	639±30	2.6±0.3	1.71 ±0.19	2919
E13, ◀	SO 100	855	1.280	18.0	1.1	139±4	1.8±0.08	1.30±0.01	3152

Table 7.1: Physical properties for the oblique collision experiments conducted in this investigation. In all cases, the liquids were mixtures of water (W), glycerol (G); percentages in the second column are by weight. Two experiments were performed using silicon oil (SO).

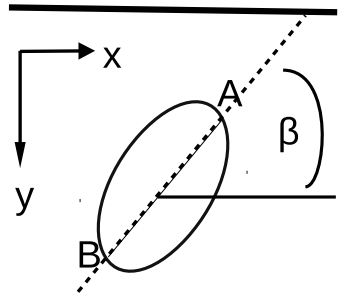

Figure 7.1: Schematic representation of the angle β measured between the major axis of the bubble, dashed line, and the wall direction, solid black line. Point A and B are the point located on the bubble and the major axis. The figure is rotated so the tangential direction of the inclined wall is horizontal. In the configuration represented the point A is the first point to collide the wall.

inclination of the wall generate a tangential velocity component during the collision. According to Pelletier et al. (2015), the zig-zag and helicoidal rising bubbles remains in a plane as soon as the contact occurs. Therefore, data of the position (x, y), time (t) and the aspect ratio (χ) provide a complete description of the phenomenon. For visualisation purposes, as illustrated in Figure 7.1, the original images were rotated in such a way that the wall coincides with the horizontal direction. Hence the **x** axis is associated with the tangential direction and the **y** axis with the normal direction, as shown in figure 7.1.

All the experimental conditions considered in this study resulted in a bounce of the bubble. Hence the Stokes number is larger than that for the transition between arrest and bouncing. When rising freely, Ellingsen and Risso (2001) and De Vries et al. (2002) showed that the nature of the wakes of bubbles rising rectilinearly differs from the nature of the wake of bubbles rising in zig-zag or in helicoidal path. However, Pelletier et al. (2015) showed that, both regimes, the normal coefficient of restitution shows a dependence with the modified normal Stokes number (St^*_{norm}), which has been proposed by Zenit and Legendre (2009) for the case of rectilinear bubble motion.

Figure 7.2 shows images of a 1.15 mm diameter bubble rising in silicon oil (experimental conditions E1) interacting with a wall tilted of 30° from the horizontal (black line). Under these conditions the bubble rises rectilinearly. For the entire experiment, the evolution of

the normal position, aspect ratio, normal and tangential velocities, major/minor axis are plotted in Figure 7.3a, 7.3b, 7.3c, 7.3d, 7.3e respectively as function of the time. The initial time ($t = 0$) is defined as the moment when the normal velocity passes, the first time, from negative values to positive values. The time is normalized by V_{term}/D_{eq} where V_{term} is the terminal velocity of the bubble and D_{eq} its equivalent diameter. The position and the velocity are also normalized by D_{eq} and V_{term} respectively. In each image of Figure 7.2, the major and minor axes, represented in red and blue lines respectively, are inferred from the Legendre polynomial expansions of the bubble contour (see Chapter 2 for more details). The major axis is indeed obtained by considering the maximum axis whereas the minor axis is orthogonal to it. The Legendre polynomial of the bubble contour is shown in green. The angle between the major axis and the wall direction, β, as illustrated in Figure 7.1 is also considered. Its temporal evolution is shown in Figure 7.3f.

For a time $t^* \leq t_1^*$ (blue line in Figure 7.3), the bubble moves toward the wall with its terminal state conditions. Therefore, the bubble following a rectilinear path, constant normal and tangential velocities as well as a constant aspect ratio are observed.

At time t_1^*, the bubble has not yet impacted the wall but both tangential and normal velocities start to decrease. Until $t^* = t_2^*$ (red line in Figure 7.2) the bubble motion is controlled by the inertial drainage of the liquid film (Zenit and Legendre (2009)). Therefore the aspect ratio and the β angle remain constant until the bubble impacts the wall ($t^* = t_2^*$).

Once the bubble impacts the wall, it starts to rotate around the point of contact, labelled as point A in Figure 7.1. This rotation process is illustrated in Figure 7.4a. During this rotation, the angle β increases progressively until the major axis aligns with the wall direction ($\beta = 0$). Therefore a viscous liquid film, a lubrication film, forms between the wall and the bubble upper surface. The size of this lubrication film increases progressively from right to left. Unlike what is observed for normal collisions, the lubrication film does not form symmetrically with respect to the bubble center. Instead it forms progressively from the first point of contact to the opposite edge of the bubble, labelled as B point in Figure 7.1. Mean-

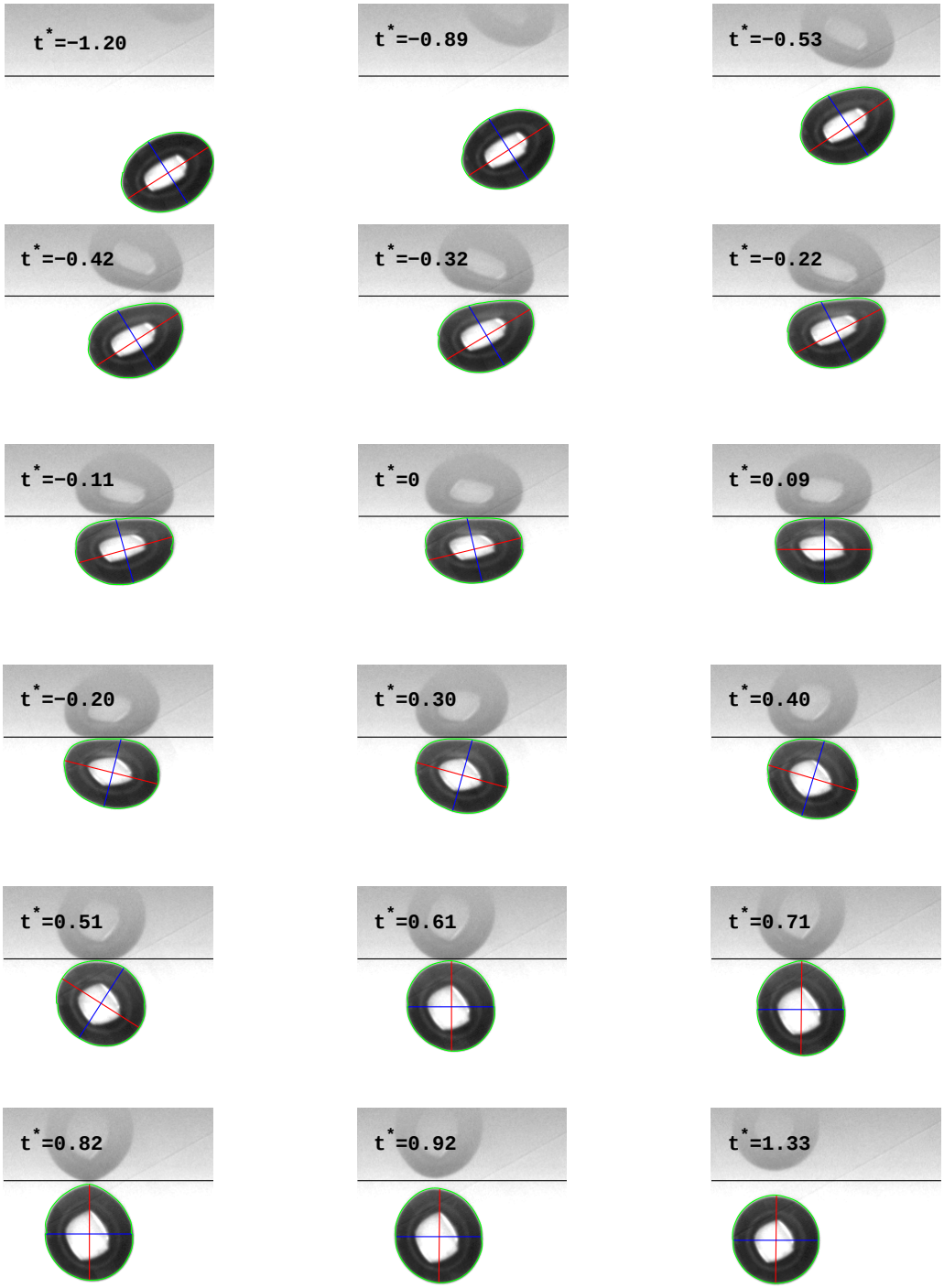

Figure 7.2: Collision of a bubble with a wall inclined of 30° from the horizontal in experimental conditions $D_{eq} = 1.3mm$, $Re_{term} = 139$, $We_{term} = 1.8$, corresponding to experiment E13, from Table 7.1. The bubble contour resulting from the Legendre polynomial expansion, the major and minor axis of the bubble are represented in solid green, red and blue lines respectively at every step time. The wall location is shown in black line. For each image the corresponding dimensionless time $t^* = t\,V_{term}/D_{eq}$ is written on top of the subcaption. Note that the image was rotated to make the wall appear horizontal.

while the bubble is compressed against the wall by its added mass inertia. Hence its aspect ratio increases and reaches a maximum value at time t_3^* (black line in Figure 7.3). Once the aspect ratio achieves a maximum value, the bubble shape evolves toward a spherical shape. The tangential velocity starts to increase as soon as the bubble impacts the wall. However, no drastic change in the normal velocity evolution is observed at the transition between the inertial drainage of the liquid film and the lubrication film formation.

At time $t^* = t_3^*$ the restitution phase begins. The normal velocity and the angle β become positive, after what they keep increasing until they reach simultaneously a maximum. For the angle β, this maximum is 90°. Indeed the bubble rotates around the B point in Figure 7.1 in the opposite direction to the rotation generated during the impact phase. This second rotation is illustrated in Figure 7.4b. Accordingly, the size of the lubrication film decreases progressively from right to left until the formation of a tail. The bubble stops rotating when the major axis becomes aligned with the normal to the wall. During this phase, the tangential velocity decreases until it reaches a minimum.

From that moment on ($t^* \geq t_4^*$) the angle β attains a 90° value. That is, the bubble remains in contact with the wall and keeps on moving normally, which leads to the formation of a tail. Accordingly, a small increase of the aspect ratio is observed. During this phase the bubble is no longer accelerated in the normal direction. Thus the impulse given by the wall is considered to end at t_4^*. Hence the increase of the tangential velocity observed for $t_4^* \leq t^* \leq t_5^*$ resulting from the flow field around the bubble rather than the effect of the wall. Indeed, as described by De Vries et al. (2002) for the interaction of a bubble with a vertical wall, the flow fields acts on the bubble under the effect of a lift force. This repulsive force is oriented normally to the bubble path and directed in the opposite direction of the pressure gradient. A positive component of the lift force is then generated in the tangential direction as the bubble moves toward the wall or more exactly as its normal velocity is negative. Combined with the effect of the buoyancy force, a tangential acceleration of the bubble is observed. For a time $t^* \geq t_5^*$ (magenta line in Figure 7.3), the bubble is bouncing and the tail detaches

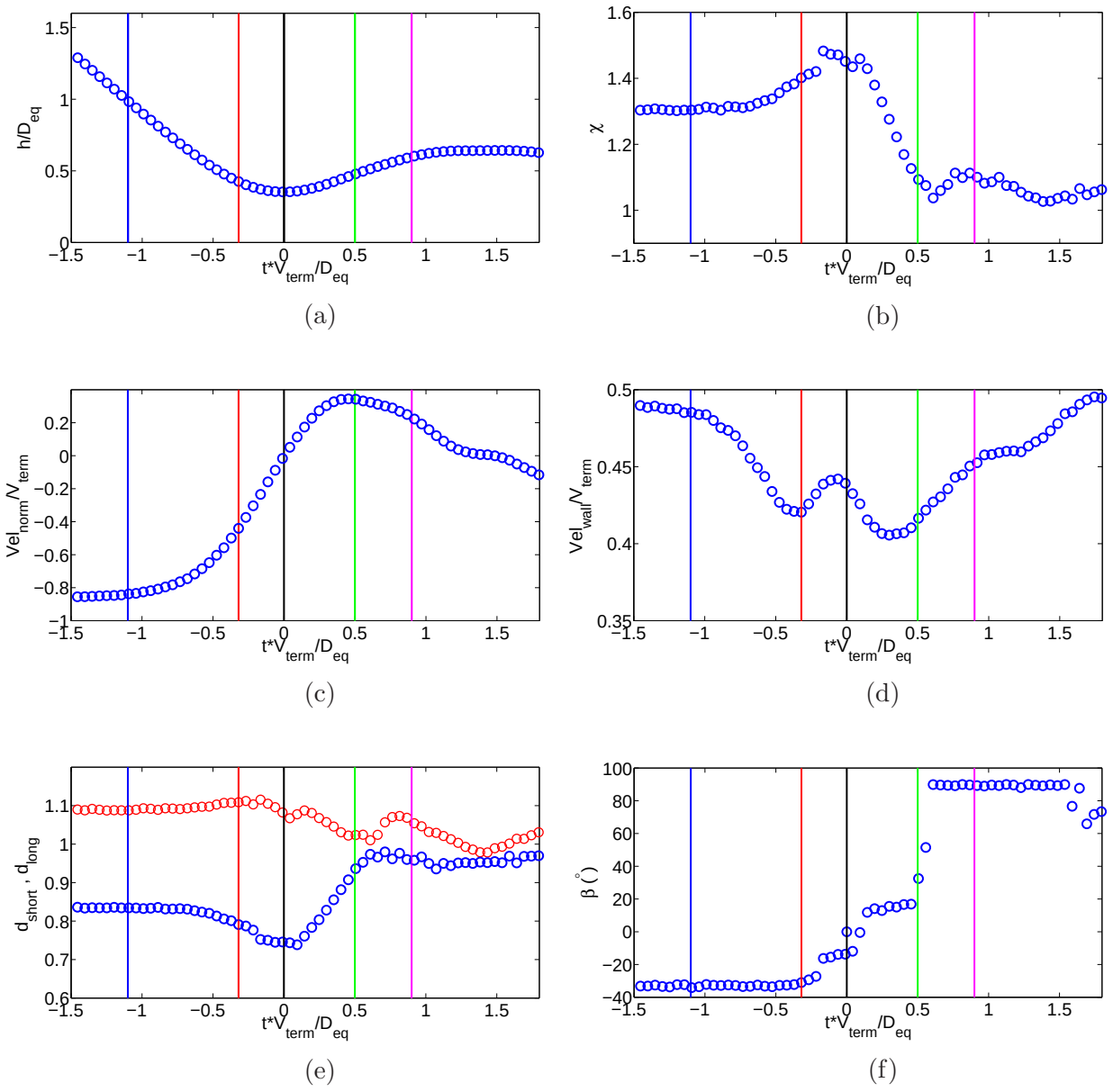

Figure 7.3: Collision of a bubble with a wall inclined of 30° from the horizontal in experimental conditions $D_{eq} = 1.3$ mm, $Re_{term} = 139$, $We_{term} = 1.8$, corresponding to experiment E13, from Table 7.1. Evolution of (a) the normalized distance between the bubble centroid and the wall, h/D_{eq}, (b) the aspect ratio, χ, (c) the normalized normal velocity of the bubble, V_{norm}/V_{term}, (d) the normalized tangential velocity of the bubble, V_{wall}/V_{term}, (e) the Major and Minor axis of the bubble (mm) in red and blue respectively, the β angle in degree as a function of normalized time, tD_{eq}/V_{term}, for the experiment shown in Figure 7.2. The dimensionless times t_1^*, t_2^*, t_3^*, $t_{3,2}^*$ and t_4^* used in the description of the collision process are plotted in each graph in blue, red, black, green and magenta lines respectively.

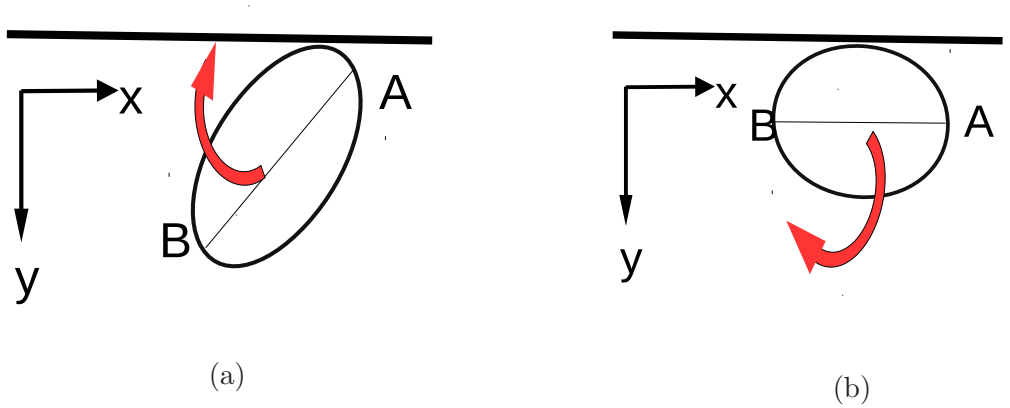

(a) (b)

Figure 7.4: Schematic representation of the two bubbles rotations during the bubble-wall collision. First when the bubble impacts the wall (a) and the lubrication film starts to form and then when the restore phase begins (b) and until the bubble tail detach from the wall. The wall location is represented with a thick black line whereas the major axis of the bubble is represented with a thin black line. The red arrows show the corresponding direction of rotation of the bubble during each phase.

from the wall. When the bubble reaches the maximum amplitude of the bounce, its normal velocity reaches a zero value. Therefore, the bubble is no longer pushed in the tangential direction until the bubble moves again toward the wall.

Different characteristic times can be chosen for the beginning and the end of the interaction. For the beginning of the process, either time t_1^* when the inertial drainage applies on the bubble dynamics or time t_2^* when the bubble impacts the wall can be considered. On the other hand, the end of the interaction may occur either when the normal velocity begins to decrease and the impulse of the wall end, t_4^*, or when the tail of the bubble detach from the lubrication film, t_5^*. Based on these considerations, the contact time can be defined as:

$$t_c = t_{depart} - t_{initial} \tag{7.2}$$

7.3 Inclination angle effects

The objective of the present section is to study the effect of the inclination angle on the collision process. The interaction of a bubble in experimental conditions E1 in Table 2.1 with a wall inclination of 15°, 30°, 45° and 60° from the horizontal is considered. The evolutions

of the distance, the aspect ratio, the normal and tangential velocities, the minor/major axis and the angle β with respect to the time are shown in Figure 7.5a, 7.5b, 7.5c, 7.5d, 7.5e and 7.5f, respectively. Each figure is color coded according to the inclination angle considered.

For the different inclination angles considered here, a similar temporal evolution is observed. Particularly, the same phases of the evolution of the aspect ratio during the collision are observed but a smaller maximum deformation is achieved as the inclination angle increases. Therefore we can observe in the wall-bubble distance evolution, Figure 7.5a, that the minimum distance decreases too. For $\theta = 60°$ (green color), no significant compression of the bubble against the wall during its collision is observed. In this particular case, the bubble evolves toward a spherical shape at the same time as it rotates. During the contact phase two simultaneous processes occur in the tangential direction, each one with a different characteristic time. On one hand, there is a transfer of kinetic energy toward surface energy. This energy transfer is associated with an increase of the aspect ratio. The time of response tends to decrease as the normal inertia of the bubble at the contact decreases, basically as the inclination angle increases. On the other hand there is the bubble rotation. The rotation begins when the angle β begins to increase and ends when it reaches 90°. Unlike the capillary time of response, the same period is observed for the four inclination angles.

As detailed in the previous section, one of the possible definition of the contact time is to consider that it starts when the bubble forms a viscous film and finishes with the impulse of the wall. Defined in this way, it corresponds to the constant period of the first bubble rotation. The spring-mass system proposed by Legendre et al. (2005) to model the normal collision of a drop with a horizontal wall is considered for the present study. Zenit and Legendre (2009) have indeed demonstrated that the same system is also representative of the bubble-wall normal collision. Considering the shape and velocity of the bubble at terminal state as the initial condition when the collision begins, the bubble start to deform then. The

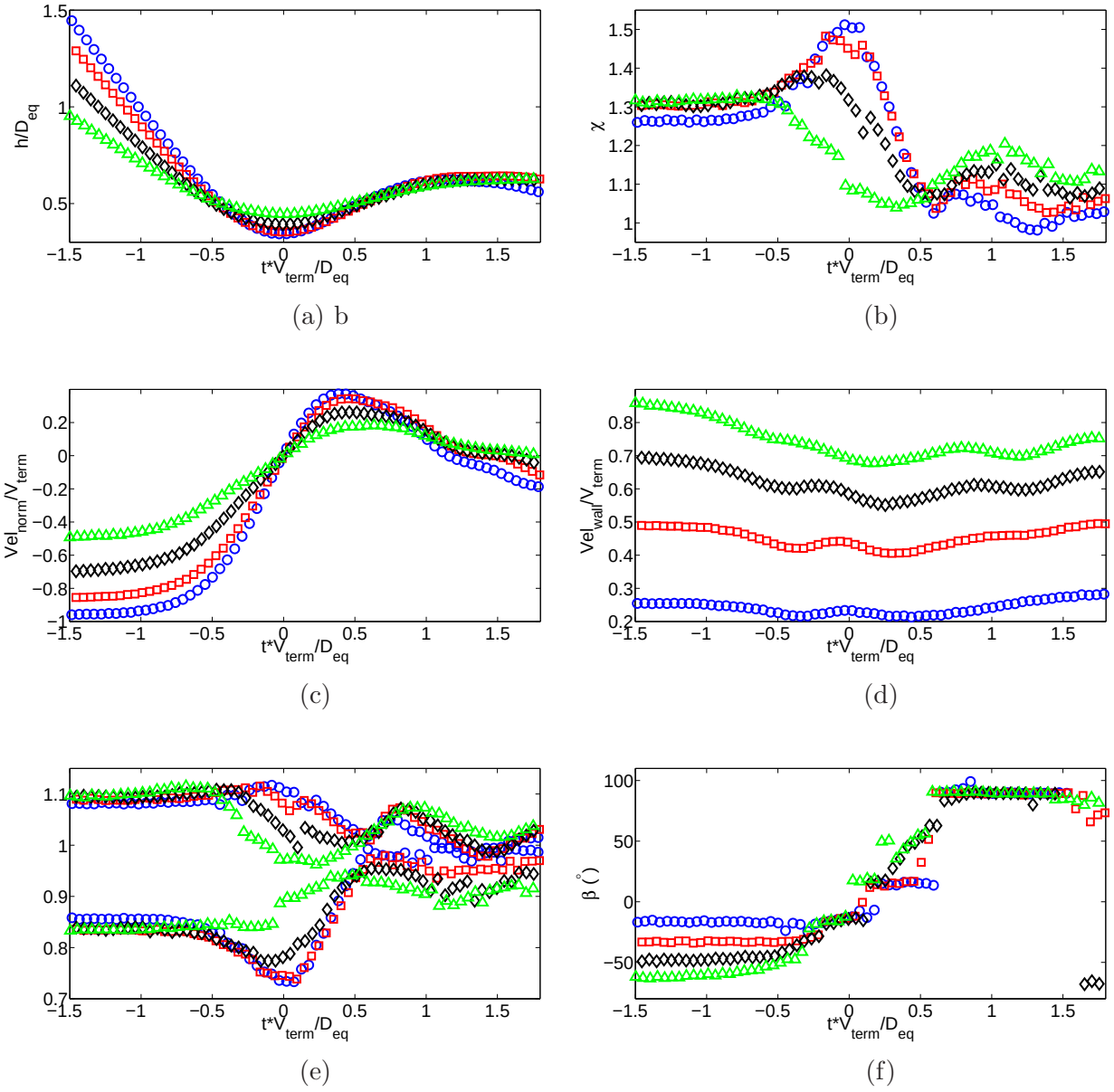

Figure 7.5: Collision of a bubble with a wall inclined of 15°, 30°, 45° and 60° from the horizontal plotted in blue, red black and green symbols respectively. The bubble interacts with the wall in experimental conditions D_{eq} = 1.3 mm, Re_{term} = 139, We_{term} = 1.8, corresponding to experiment E13, from Table 7.1. Evolutions of (a) the normalized distance between the bubble centroid and the wall, h/D_{eq}, (b) the aspect ratio, χ, (c) the normalized normal velocity of the bubble, V_{norm}/V_{term}, (d) the normalized tangential velocity of the bubble, V_{wall}/V_{term}, (e) the major and minor axes of the bubble (mm) in red and blue respectively, the β angle in degree as a function of normalized time, $t\,V_{term}/D_{eq}$.

bubble deformation in the direction normal to the wall is defined as:

$$\eta(t) = Axis_{norm,term} - Axis_{norm,t} \tag{7.3}$$

Hence, the temporal evolution of the normal deformation of the bubble is governed by the mass-spring equation system proposed by Zenit and Legendre (2009):

$$m^* \frac{\partial \eta^2}{\partial t} + K_1 \mu R_{eq} \frac{\partial \eta}{\partial t} + K_2 \sigma \eta = 0 \tag{7.4}$$

with $m^* = \frac{4}{3}\pi \rho^* R_{eq}^3$ the total mass involved in the collision considering $\rho^* = \rho_b + C_{AM}\rho_l$ where C_{AM} is the added mass coefficient of the bubble. K1 and K2 are constants.The second term of the equation represents the viscous dissipation generated by the liquid film drainage. It is modelled by the lubrication force expression of Klaseboer et al. (2001) considering a constant film thickness. As defined previously, the contact time initiates when η begins to change, that is when $t = 0$, and finishes when the bubble-wall distance becomes higher than one radius, that is when η becomes zero. The contact time thus corresponds to the half-period of the solution of equation (7.4), and is given by:

$$\tau_\mu = \pi \sqrt{\frac{m^*}{K_2 \sigma}} / \sqrt{1 - (\frac{1}{2} K_1 \mu R_{eq})^2 / K_2 \sigma m^*} \sim \pi \sqrt{\frac{m^*}{K_2 \sigma}} \tag{7.5}$$

The theory is therefore in agreement with the constant contact time observed for the experimental conditions considered here. In addition, the time evolution of the normal velocity during the contact is in agreement with the velocity profile reported by Zenit and Legendre (2009). similarly, a smaller rebound velocity is observed as the normal Stokes number, $St^*_{norm} = \frac{(\rho_b + C_{AM}\rho_l) D_{eq} U_{norm}}{9\mu}$, decreases. Given these agreement between the results of the normal velocity and the spring-mass model, this latest should predict well the normal behavior of the bubble. We will evaluate after this assumption considering the evolution of the normal coefficient of restitution. The tangential velocity decrease generated during both

the inertial drainage of the liquid film and the contact phase can be related to the terminal tangential velocity. The temporal evolution of the tangential velocity shows the need to define clearly the initial and terminal times of the collision. According to this choice, completely different values of tangential coefficient of restitution can be obtained; this is not the case for the normal coefficient of restitution. Tangential coefficients of restitution larger than one have been reported by Pelletier et al. (2015). Such values are disconcerting given that the coefficient of restitution is a measure of the energy dissipated by the collision. Based on the velocity evolution with the time, we consider the dimensionless time t_4^*, when the normal velocity of the bubble reaches its maximum, as the end of interaction. The dimensionless time t_1^* just before the beginning of the inertial drainage phase will be considered as the initial time. The moment when the bubble impact the wall, t_2^*, will also be considered as a second option.

7.4 Energy balance

Following the idea proposed by Legendre et al. (2005) to study of the impact of a drop against an horizontal wall, and Zenit and Legendre (2009), for a bubble impacting an horizontal wall, the oblique collision process can be represented through a coefficient of restitution. Generally speaking, this parameter is defined as

$$\epsilon = -\frac{V_{depart}}{V_{impact}} \tag{7.6}$$

where, U_{impact} is either the bubble velocity at the beginning of the inertial drainage of the liquid film or the bubble velocity of impact. U_{depart} is the velocity of the bubble when the normal velocity reaches its maximum. With regard to the oblique collision, the normal and tangential coefficients of restitution can be obtained by applying this definition to the tangential and normal velocities respectively. The coefficient of restitution gives an indirect measure of the energy dissipated during the collision. A detailed description of the energy

transfer during the different phases of the interaction is thus considered here.

When a bubble collides with a wall, it can either bounce or arrest. The behavior adopted by the bubble results from the competition between surface energy, kinetic energy and dissipation. First, the bubble moves at its terminal state conditions. The corresponding kinetic energy is balanced by the surface energy associated with the ellipsoidal shape of the bubble. Then during the inertial drainage of the liquid film, its velocity decreases while the bubble keeps a constant shape. Accordingly, a transfer from the kinetic energy to the dissipation energy should be observed. Once the bubble impacts the wall, its shape evolves considerably while its velocity decreases quickly. Consequently, its kinetic energy is not only dissipated but it is also transferred toward surface energy. When the restitution phase begins, the surface energy is, in turn, transferred back to kinetic energy. The rebound occurs when the kinetic energy restored through the bubble deformation is larger than the dissipation resulting from the resistance of the viscous film. For an oblique collision, the energy transfer process is not fundamentally changed from the normal collision process, but it is complicated due to the existence of two component of the motion.

The surface energy associated with the terminal state of the bubble can be taken as reference to study the effect of the wall. The evolution of surface energy under the effect of the wall is thus given by:

$$E_{\Delta,S} = \sigma \left(A(t) - A_{term} \right) \tag{7.7}$$

where σ is the surface tension of the bubble and A(t) and A_{term} are the bubble area at time t and at its terminal state, respectively. To evaluate the bubble surface, the Legendre polynomial expansion of the shape contour, whose method of calculation is shown in Chapter 2, is used:

$$A(t) = 2\pi \left(\int_0^{\pi} \sqrt{1 + \left(\frac{\frac{\partial R(\theta,t)}{\partial \theta}}{R(\theta,t)} \right)^2} \left(R(\theta,t) \right)^2 sin\theta \, d\theta \right) \tag{7.8}$$

The kinetic energy of a deformed bubble is calculated according to:

$$E_k = \frac{1}{2}(C_{AM}\rho_l + \rho_b))\mathcal{V}_b(U_{norm}^2 + U_{wall}^2) = E_{k,norm} + E_{k,wall} \tag{7.9}$$

The bubble volume, $\mathcal{V}_b$, is calculated with its equivalent diameter ($\mathcal{V}_b = \frac{1}{6}\pi D_{eq}^2$). C_{AM} is the added mass coefficient. The expression proposed by Milne-Thomson (1968), considering the bubble aspect ratio, χ, is used:

$$C_{AM} = \frac{\alpha}{2-\alpha},\ \alpha = \frac{2\,\chi^2}{\chi^2-1}\left(1 - \frac{1}{\sqrt{\chi^2-1}}cos^{-1}(1/\chi)\right) \tag{7.10}$$

Finally, the dissipated energy is obtained by considering the method proposed by Jeong and Hyungmin (2015). Since the total energy of the bubble is composed of the sum of surface energy, kinetic energy and dissipation energy, the energy dissipation is:

$$E_D(t) = (E_{S,term} + E_{k,term}) - (E_S(t) + E_k(t)) \tag{7.11}$$

The temporal variations of the surface energy, $E_{\Delta,S}$, the kinetic energy, $E_{k,norm}$ and $E_{k,wall}$, and the dissipated energy for a 1.15 mm diameter bubble in silicon oil (Experiment E1) interacting with a wall tilted of 15°, 30°, 45° and 60° from the horizontal are shown in Figure 7.6. The figure is color coded according to the inclination angle considered. Once the inertial drainage of the liquid film begins at $t^* = t_2^*$ a small decrease of the surface energy is observed as its front interface tends to flatten close to the wall. This phenomenon, illustrated in Figure 7.7, induces a decrease of the bubble surface. By comparison, more significant dissipation is observed from a decrease of tangential and normal kinetic energies. The normal velocity of the bubble evolves according to the inertial model proposed by Zenit and Legendre (2009) for the normal approach of a bubble:

$$\frac{h_t}{V_{term}} = \left(\frac{2\kappa+1}{2\kappa+h_0/h}\right)^{3/2} \tag{7.12}$$

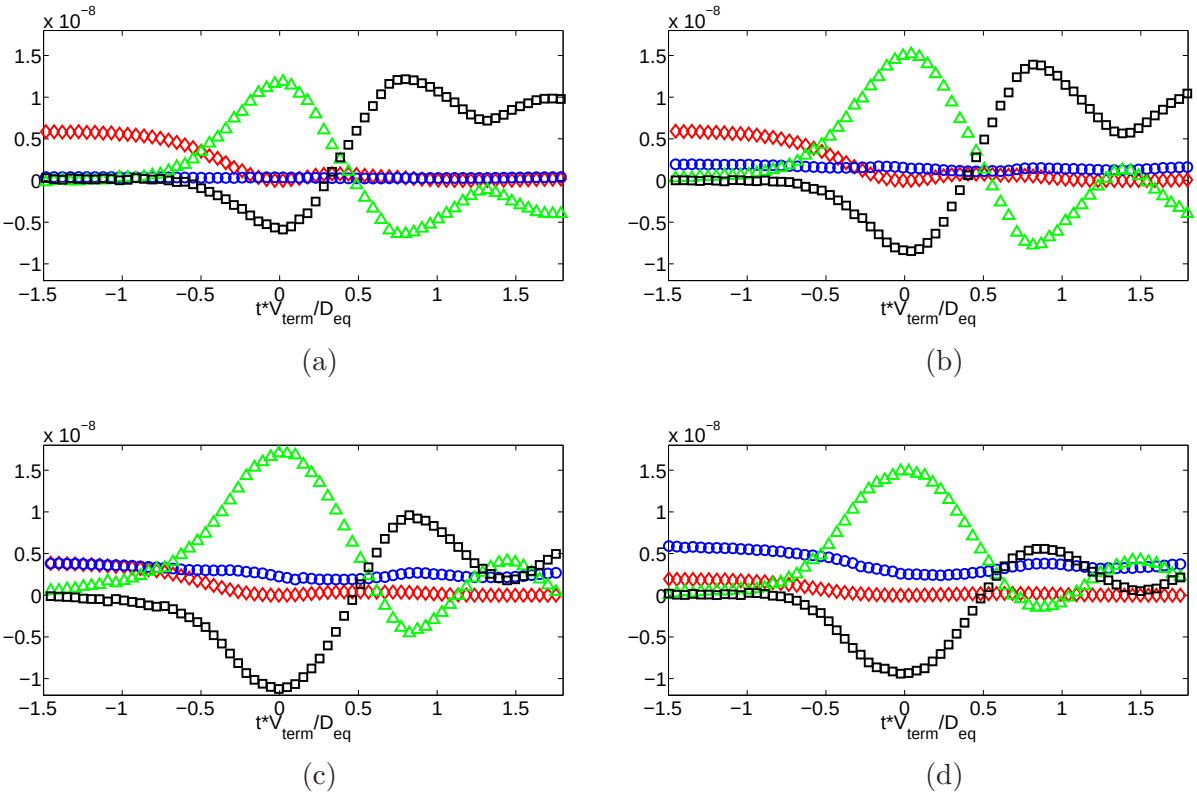

Figure 7.6: Collision of a bubble with a wall inclined of (a) 15°, (b) 30°, (c) 45° and (d) 60°. The bubble interacts with the wall in experimental conditions $D_{eq} = 1.3$ mm, $Re_{term} = 139$, $We_{term} = 1.8$, corresponding to experiment E13, from Table 7.1. In each graph the evolutions of normal kinetic energy, $E_{k,norm}$ (red symbols), the tangential kinetic energy, $E_{k,wall}$ (blue symbols), surface energy, $E_{\Delta,S}$ (black symbols) and dissipation energy, E_D (green symbols) as a function of normalized time, $t\,V_{term}/D_{eq}$.

Figure 7.7: Images of bubble in its terminal states (a) and at the end of the inertial drainage of the liquid film phase (b). The bubble interacts in experimental conditions E13 corresponding to $D_{eq} = 1.3$ mm, $Re_{term} = 139$, $We_{term} = 1.8$. Images are shown at the same scale.

with V_{term} the terminal velocity of the bubble and κ a constant based on the physical parameters. h_0 and h represents the distance from the bubble interface to the wall at the beginning of the inertial drainage phase and at time t respectively, h_t its time derivative. It is very likely that the tangential velocity evolves according to the same physics.

As soon as the bubble impacts the wall at t_2^*, a drastic change of tangential kinetic energy is observed. Depending on the inclination angle considered, the wall kinetic energy can either increase or maintain a constant value. On the other hand, no clear transition is observed for the normal kinetic energy evolution. For the surface energy, a fast decrease is observed resulting from the flattening of the bubble surface as illustrated in Figure 7.7. Indeed the bubble is compressed against the wall by its added mass inertia leading to a decrease of the surface area. Legendre et al. (2005) and Zenit and Legendre (2009) have demonstrated that the lubrication film formation induces an important viscous dissipation. Thus an increase of the dissipation energy is observed during this phase.

Based on the energy variations with respect to the time, a new time ($t_{2,1}^*$) is introduced that characterizes the moment when the bubble shape evolves toward a spherical shape as response to the impact. This moment will be referred as capillary response time. The capillary response of the bubble interface induces a decrease of the size of the lubrication film which is balanced by the effect of the bubble rotation, illustrated in Figure 7.4a. Therefore, a nearly constant surface energy is observed until the beginning of the restitution phase. Meanwhile, the normal kinetic energy is close to zero as the bubble reaches its minimum distance to the wall. This phase is characterised by a tangential motion of the bubble. A strong decrease of the wall kinetic energy is observed: the wall velocity decreases due to the shape evolution. The largest dissipated energy is achieved during this phase because it corresponds to the maximum size of the lubrication film, generating the largest amount of viscous dissipation.

Subsequently, the restore phase begins and the bubble shape evolves. Its surface energy is increased. In parallel to this change of shape, the bubble rotates around its left side as illustrated in Figure 7.4b. An important part of the surface energy is transferred to the

normal kinetic energy. Accordingly, an increase of the normal kinetic energy is observed until it achieves a local maximum when the wall impulse ends (t_4^*). On the other hand, as a response to the bubble rotation and shape evolution associated with the bubble expansion, a strong decrease of the wall kinetic energy is observed. Therefore, the viscous dissipation is significantly reduced.

From the moment when the normal velocity of the bubble reaches a maximum, the bubble is no longer pushed by the wall. Yet, because of the inertia generated by this last impulse at time t_4^*, the bubble keeps on moving normally to the wall. As a consequence, a small decrease of the normal kinetic energy is observed during this phase. Due to this normal motion and the resistance of the lubrication film on the bubble interface, the bubble shape expands in the direction normal to the wall. Its surface energy is largely increased until the bubble tail detachment. At this precise moment, the surface energy reaches its maximum value. This maximum is much larger than its surface energy at the terminal state. An energy dissipation, smaller than that at the terminal states, is observed during the whole phase. It reaches a minimum value when the tail of the bubble begins to detach from the lubrication film.

Once the tail detaches from the lubrication film, the bubble is no longer in contact with the wall. As a consequence, the bubble tends to recover a shape similar to the terminal state. The associated surface energy decreases significantly. Because of the lower inertia achieved by the bubble during this phase, in comparison with its terminal state, a larger surface energy is observed. Once its shape stabilises its inertia increases again under the combined effect of the buoyancy and the lift force. Hence the bubble evolves toward an ellipsoidal shape so its surface energy increases.

7.5 Coefficients of restitution

Based on the detailed description of the different mechanisms of energy transfer and instantaneous velocities evolution detailed in the previous sections, a model for the coefficient of

restitution will be developed in this section. To support this model, the entire range of experimental conditions of Table 7.1 is considered for inclination angles from 5° to 75°. Because of the wall inclination and the free rising of the bubble before they impact a normal and a tangential coefficient of restitutions are defined as:

$$\epsilon_{norm} = |\frac{V_{norm,depart}}{V_{norm,impact}}| \tag{7.13}$$

$$\epsilon_{wall} = |\frac{V_{wall,depart}}{V_{wall,impact}}| \tag{7.14}$$

In the previous section, careful attention has been paid to define the times for impact and rebound. Accordingly, the terminal conditions ($h \geq D_{eq}$) and the end of the wall impulse are considered. Defined in this way, the coefficient of restitutions will give an indirect measure of the energy dissipation resulting from the inertial drainage of the liquid film, the formation of the lubrication film and the restore phase. Unlike for the normal velocity evolution, Figure 7.5c, a drastic change of behavior is observed in the tangential velocity evolution when the bubble impacts the wall or, more precisely, when the formation of the liquid film starts. Hence, the terminal state of the bubble should be considered to describe the collision process. The wall effect is considered to end when the normal acceleration of the bubble evolves considerably as the consecutive motion is actually due to the flow field configuration. Based on the normal velocity evolution, the constant contact time and the evolution of the coefficient of restitution with the modified normal Stokes number, the normal behavior of the bubble was found to be in agreement with the model proposed by Zenit and Legendre (2009).

7.5.1 Normal coefficient of restitution

The model, established for the velocity evolution of a bubble colliding against an horizontal wall, consists in a mass-spring system to represent the evolution of the normal deformation of the bubble according to equation (7.4). From the solution of this model equation, the

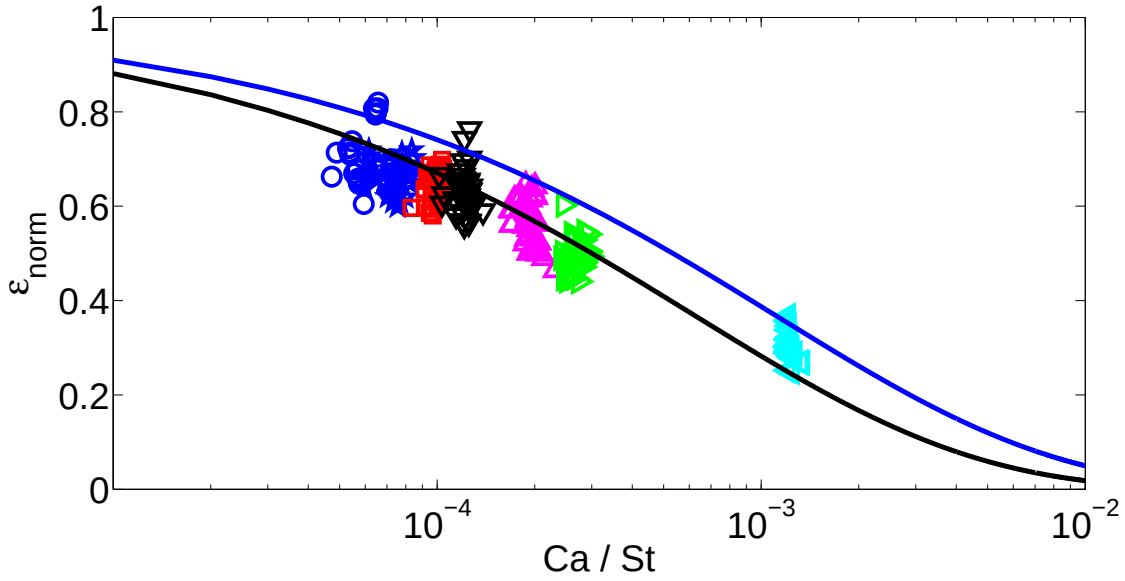

Figure 7.8: Coefficient of restitution based on the bubble normal velocity ϵ_{norm} as a function of the ratio of the capillary number and the modified Stokes number based on the normal velocity Ca_{norm}/St^*_{norm}. The experimental results are plotted according to the symbols of Table 7.1. The blue line corresponds to expression (7.17) while the black line corresponds to a fit of expression (7.16) considering all the experimental data except the one corresponding to conditions E12 and E13.

coefficient of restitution can be estimated considering the value of the bubble velocity at the impact and the depart:

$$\epsilon_{norm} = |\frac{\frac{\partial \eta}{\partial t}_{t=t_{max}}}{\frac{\partial \eta}{\partial t}_{t=0}}| = -\frac{\partial \eta}{\partial t}_{t=t_{max}} \tag{7.15}$$

where t_{max} is assumed to correspond roughly to the moment when the bubble recover its initial shape, that is when $\eta = 0$. The normal coefficient of restitution is shown to scale as:

$$\epsilon_{norm} = exp\left(-\frac{\pi}{2}\frac{K_1}{\sqrt{K_2}}\sqrt{\frac{Ca_{norm}}{St^*_{norm}}}\right) \tag{7.16}$$

with K_1 and K_2 constants of equation 7.4 and Ca_{norm} and St^*_{norm} the capillary and modified Stokes numbers based on the normal velocity and integrating the added mass effects. Figure 7.8 shows the normal coefficient of restitution measured for all the experimental conditions of Table 7.1. The experimental data follows clearly the dependence of equation (7.16) given

by the mass spring system represented in blue line and black line. For the experimental data recorded with a similar framing rate as for the Zenit and Legendre (2009) study, E12 and E13, the normal coefficient of restitution is fitted by the expression proposed by Zenit and Legendre (2009):

$$\epsilon_{norm} = exp\left(-30\sqrt{\frac{Ca_{norm}}{St^*_{norm}}}\right) \tag{7.17}$$

Considering that the only difference between E10 and E12 is the framing rate used, we can conclude that the framing rate in all the experiments but E12 and E13 underestimate the departure velocity but reproduces the correct trend. Nonetheless, the model of Zenit and Legendre (2009) reproduces correctly the normal coefficient of restitution. This result is important since equation (7.17) can be used to represent bubble-wall collision not only for horizontal wall but also for inclined wall and independently of the free rising motion nature.

7.5.2 Tangential coefficient of restitution

We now consider the tangential coefficient of restitution, ϵ_{wall}. The tangential motion of the bubble is controlled by the competition between the inertia, the surface deformation and the viscous dissipation. The dimensionless numbers associated to the competitions between these forces are thus considered in order to report the evolution of ϵ_{wall}. The competition between the surface deformation and the inertia is characterized by the tangential Weber number, whereas the competition between the viscous dissipation and the inertia is described with the tangential Reynolds number. Finally, the competition between the the surface deformation and the viscous dissipation is represented by the tangential Capillary number. All the dimensionless numbers are calculated with the tangential components of the terminal conditions of the bubble. In Figure 7.9 the evolution of the experimental tangential coefficient of restitution with these three dimensionless numbers is plotted. There are two clear different behaviors depending on the collision process as described in Figure 7.4 and 7.10. Considering the one-way collision process of Figure 7.4, reported using empty symbols, a nearly constant

tangential coefficient of restitution is shown:

$$\epsilon_{wall} \sim 0.8 \tag{7.18}$$

Note that Pelletier et al. (2015) reported that when air bubbles impact an horizontal wall in tap water with a large tangential velocity the associated tangential coefficient of restitution hold a constant value of 0.55. This value is smaller than the mean value observed here, but the impact and depart time were defined differently. Considering now the reversed collision process, represented using filled symbols, a clear dispersion of the data is observed on the plot and any of the non dimensional numbers used is able to provide a satisfactory description of the tangential bouncing process. Indeed, given that the bubbles rose in zig-zag or helical path, in some cases the bubble is orientated in such a way that the B point in Figure 7.1 collides the wall before the point A, or more specifically with a positive beta angle. The images of a bubble that interacts according to this scheme is illustrated in Figure 7.10 from the left top to the right bottom of the figure. The area of all the images is the same and the time between each frame is 3.42 ms. The bubble impacts the wall first with the edge opposite to the rising direction. A different amount of energy is then dissipated during the collision depending on whether the tangential motion of the bubble changes its direction or not. This phenomenon is more likely to happen for small inclination angles, the high values of ϵ_{wall} compared to these for small tangential Weber numbers. Globally, for the experimental conditions of Table 7.1 a small value of the tangential coefficient of restitution is then obtained. Finally, the tangential coefficient of restitution ϵ_{wall} is reported as a function of Ca/St because this dimmensionless group is the more relevant for the normal collision. Figure 7.11 shows the evolution of the tangential coefficient of restitution with this parameter. Note that Ca/St does not depend on the velocity so it is not sensible to the chose of the characteristic velocity for describing the tangential motion.

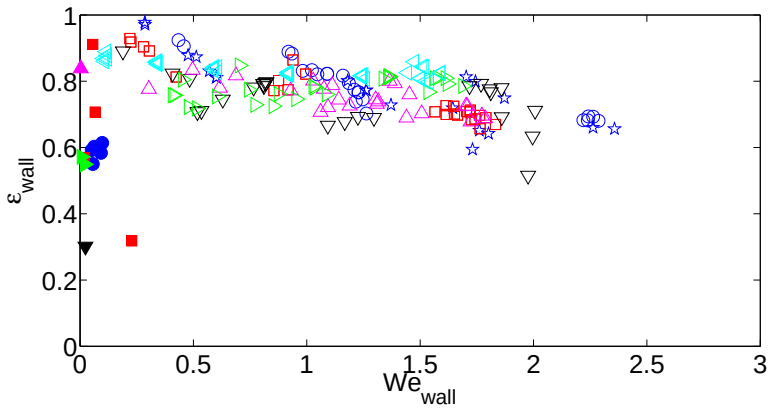

(a)

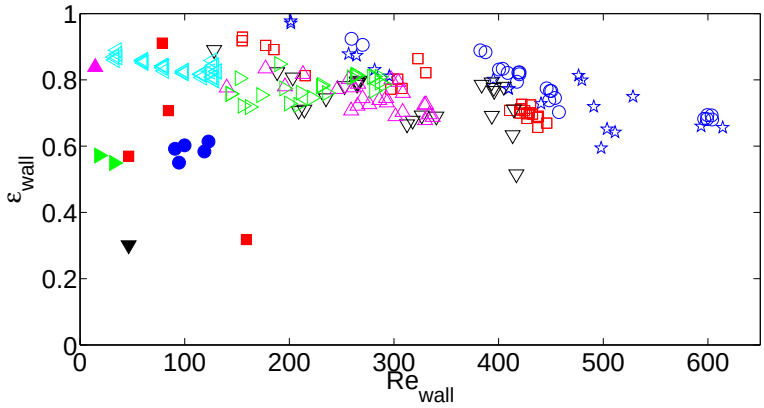

(b)

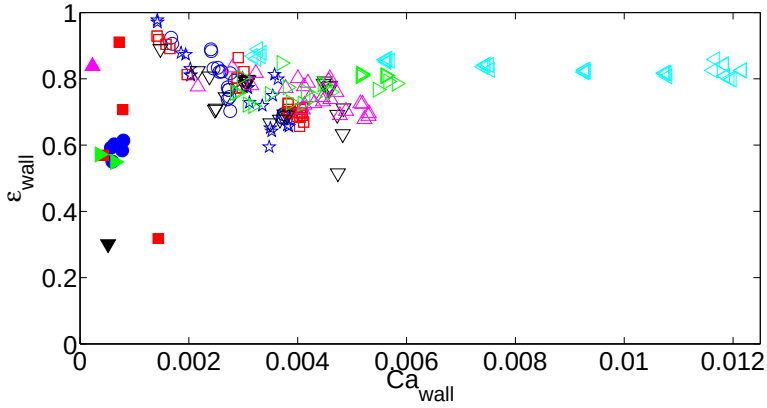

(c)

Figure 7.9: Coefficient of restitution based on the bubble tangential velocity ϵ_{wall} as a function of (a) the Weber number based on the tangential velocity We_{wall}, (b) the Reynolds number based on the tangential velocity Re_{wall} and (b) the Capillary number based on the tangential velocity Ca_{wall}. The experimental results are plotted according to the symbols of Table 7.1. The empty and solid symbols show the results obtained when the bubble interacts with the wall according to the one-way (Figure 7.4) and to the reversed collision process (Figure 7.10), respectively.

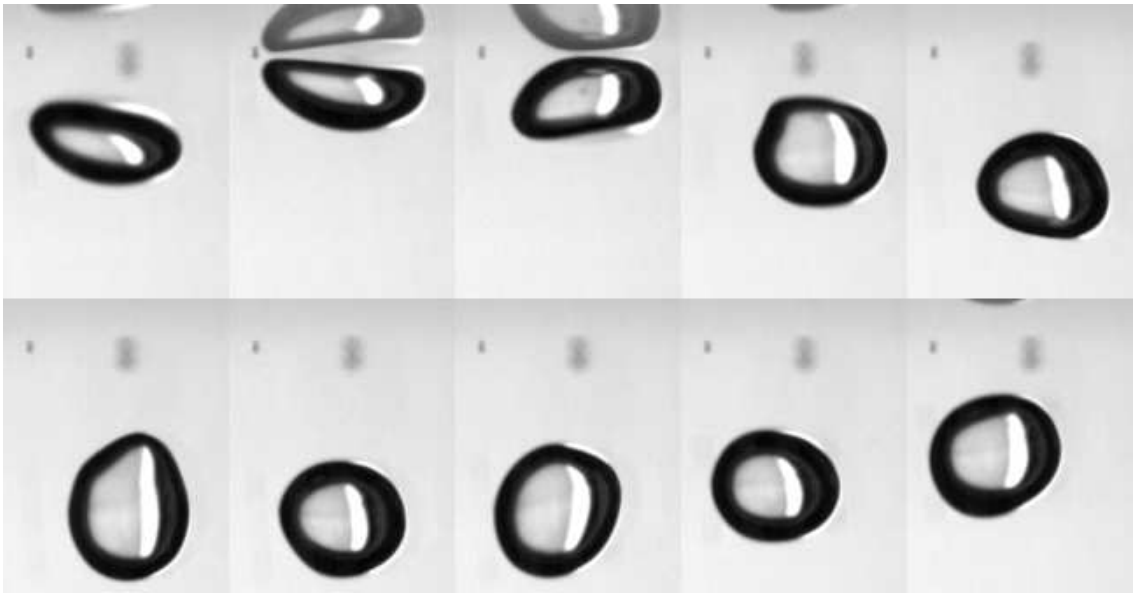

Figure 7.10: Collision of a bubble with a wall inclined of 5° from the horizontal in experimental conditions $D_{eq} = 1.9$ mm, $Re_{term} = 635$, $We_{term} = 2.6$, corresponding to experiment E12, from Table 7.1. Time series ordered from top left to bottom right, $\Delta t = 3.42$ ms illustrating the reversed collision of a bubble. For each image the area shown is the same.

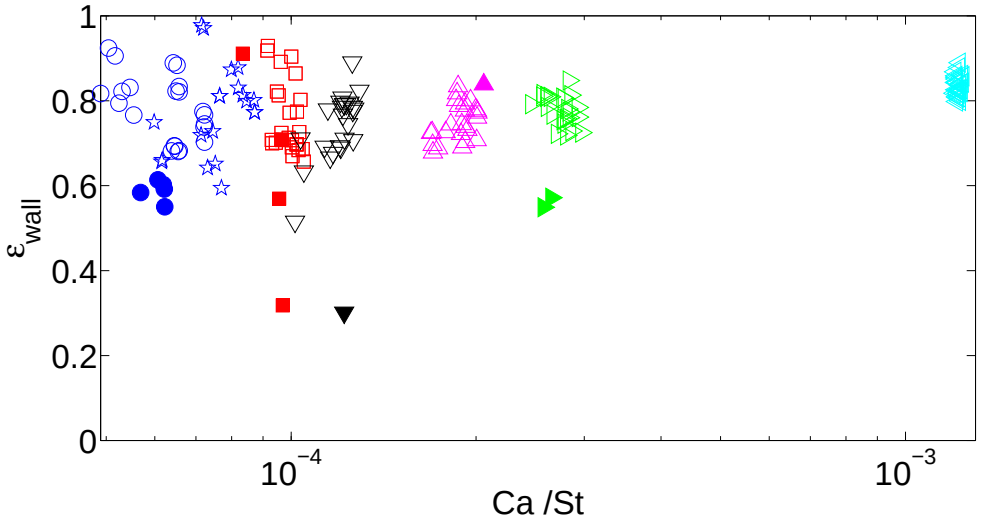

Figure 7.11: Coefficient of restitution based on the bubble tangential velocity ϵ_{wall} as a function of the non dimensional group Ca/St. The experimental results are plotted according to the symbols of Table 7.1. Empty and solid symbols show the results obtained when the bubble interacts with the wall according to the one-way (Figure 7.4) and to the reversed collision process (Figure 7.10), respectively.

7.6 Conclusion

The process of collision of a bubble with an inclined wall was studied experimentally using the experimental setup described in Chapter 2. The instantaneous bubble shape and position were recorded using two framing rates (1000 s^{-1} and 3000 s^{-1}). By considering a range of bubble diameter ($1.8 < D_{eq} < 2.7$ mm) and a variety of liquids, a range of terminal conditions $300 < Re_{term} < 300$ and $1.8 < We_{term} < 2.7$, was generated. Because of this range of experimental conditions, bubbles rising rectilinearly as well as in zig-zag and helically were observed. The inclination angle was varied from 5° to 75°.

As the bubble moves close to the wall at terminal state, its velocity begins to decrease significantly while its front interface flattens because of the inertial drainage of the liquid film. Once the bubble impacts the wall, it rotates around the side that first touches the wall until its major axis aligns with the wall direction. This rotation induces the formation of a lubrication film. Meanwhile the bubble interface begins to react to the collision and the bubble shape evolves toward a spherical shape. Then the restoring phase starts when the normal velocity changes its sign and the bubble rotates in the opposite direction until its major axis aligns with the direction normal to the wall. Then the wall impulse ends. The velocity evolution in normal direction (Zenit and Legendre (2009))is again well reproduced by a mass-spring system. In this system, the inertia is considered through the added mass, the viscous dissipation comes from the formation of the lubrication film and the springness results from the surface energy of the bubble. When the same framing rate as that used by Zenit and Legendre (2009) was used, the data of the normal coefficient of restitution agreed well with on the expression proposed for the velocity magnitude in normal contact. Based on the tangential velocity and kinetic energy evolutions during the collision, the end of the wall impulse was defined as the correct moment for the departure time used in the definition of the coefficient of restitution. Indeed during the period that separates the end of the wall impulse from the moment when the tail detaches from the wall, a significant increase of the tangential velocity is observed. This phenomenon is actually induced by the velocity field around the

bubble that induces a lift force and should not be attributed to the collision process. As no clear trend was generated, the tangential coefficient of restitution may be the result of the competition between the bubble inertia and its surface energy or the viscous dissipation and the surface energy. Therefore the tangential Weber number and the tangential Capillary number were considered to correlate ϵ_{wall}. For the range of conditions considered here, the tangential coefficient of restitution can actually be modelled by a constant value of 0.8. An expansion of the film draining model of Zenit and Legendre (2009) in two dimensions could be developed. Also, a comparison with other studies (Pelletier et al. (2015), Jeong and Hyungmin (2015)) is necessary to validate the present results. Finally, the numerical results will provide important data, unreachable experimentally to complete the understanding of this phenomenon.

Chapter 8

2D Numerical results of bubble interaction with an inclined wall

8.1 Problem statement

Through the mesh refinement step presented in Chapter 3, an optimal mesh system for the simulation of the interaction of a 2D bubble with an horizontal wall was generated. The first objective of the numerical simulations of the bubble / inclined wall interaction is to produce physical parameter ranges impossible to generate experimentally. The Numerical simulation make possible the independent variation of the parameters. The numerical simulations also generate results useful to clarify the physics of the mechanism and support the proposed theories. The second contribution of the numerical simulations is to provide data of velocity and pressure fields in and out of the bubble. Such data can only be given experimentally through measure techniques that are likely to affect the physical properties of the bubble (for example the PIV technique affects the interface behavior by introducing particle in the liquid) or the liquid.

First, the numerical configuration has to be tested for the inclined wall configuration. As detailed in Chapter 3, the inclination of the wall is produced numerically by tilting the gravity

vector from the vertical. The numerical bubble diameter being fixed, the physical parameters of the liquid and the gas have to be adapted so that the behavior of the numerical bubble can be compared to one of the experimental conditions of Table 2.1. According to the maps of Clift et al. (1978) illustrated in Figure 8.1 equivalent terminal conditions will be produced by matching Morton and Bond numbers. The experimental conditions E10 of Table 2.1 are considered for this study with the following dimensionless number values:

$$Mo = 2.14 \times 10^{-11} \ , \ Bo = 0.36 \tag{8.1}$$

From the experimental results obtained by high speed camera visualisations and PIV technique, the dynamical oblique collision process and the steady motion of the bubble will be compared to the simulation results. Hence the capacity of 2D simulation to reproduce correctly the 3D interaction of a bubble with an inclined wall will be evaluated. Such 2D simulations induce an optimal cost of time compare to fully 3D simulations.

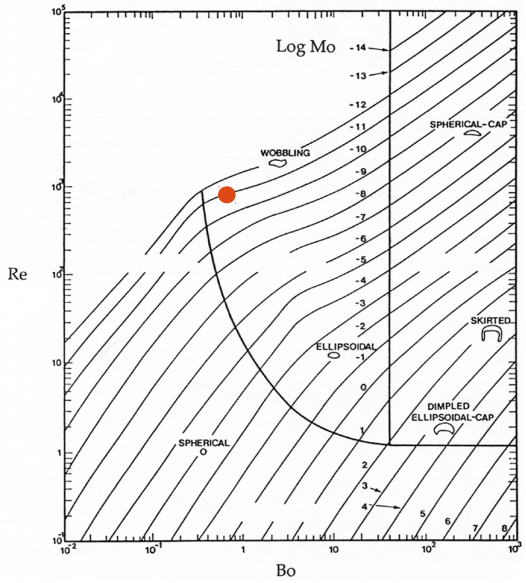

Figure 8.1: Shape regime for the bubbles and drops in unhindered gravitational motion through liquids of Clift et al. (1978). The circle represents the experimental data E10 whose dimensionless numbers are $Mo = 2.14 \times 10^{-11}$, $Bo = 0.36$

8.2 Terminal condition

Considering the values of Morton and Bond numbers of the experimental conditions E10 and the numerical diameter of the bubble ($D_{eq} = 20mm$), the physical parameters of Table 8.1 are chosen for the numerical simulations. The associated Morton and Bond numbers are 2.14×10^{-11} and 0.4 respectively, close to the experimental conditions E10. A first simulation is then conducted to simulate the free rising of the 2D bubble. After a transient period, the bubble reaches its terminal state conditions. The bubble rises rectilinearly at a

Symbol	ρ_l kg/m^3	μ_l Pas	ρ_g kg/m^3	μ_g Pas	σ N/m	D_{eq} mm	g $m.s^{-2}$	Re_{term}	We_{term}	χ_{term}	θ_{trans}
■	1000	0.0379	10	0.000379	9.81	20	9.81	560	2.30	1.34	55°

Table 8.1: Physical properties the numerical simulations conducted for the validation of the JADIM code for the bubble inclined wall interaction. The subscript l refers to the liquid properties while the subscript g refers to the bubble properties.

(a) (b)

Figure 8.2: Images of the shape of the free rising bubbles, respectively produced by the 2D numerical simulation (a) and experimentally recorded (b). The free rise of the bubble was simulated under the conditions of Table 8.1 and in experimental conditions E10 of Table 2.1 leading to the conditions: (a) $Re_{term} = 560$, $We_{term} = 2.30$, $\chi_{term} = 1.34$ and $D_{eq} = 20$ mm and (b) $Re_{term} = 614$, $We_{term} = 2.9$, $\chi_{term} = 1.78$ and $D_{eq} = 1.6$ mm

terminal velocity of $Re_{term} = 560$ and with an aspect ratio of $\chi_{term} = 1.34$. The shape of the 2D numerical bubble is shown in Figure 8.2 together with the shape of the real bubble at its terminal state in experimental conditions E10. The experimental bubble rose in zig-zag motion and seemed to be partially contaminated. To compare both terminal behaviors, we consider the terminal drag coefficient and aspect ratio together with the experimental data of Table 2.1. The theoretical expressions are detailed in section 4.1. A good correspondence of the Reynolds is obtained whereas the numerical terminal Weber number is smaller than the associated experimental values.

In spite of these differences a similarity between the simulation and the corresponding experiment is observed.

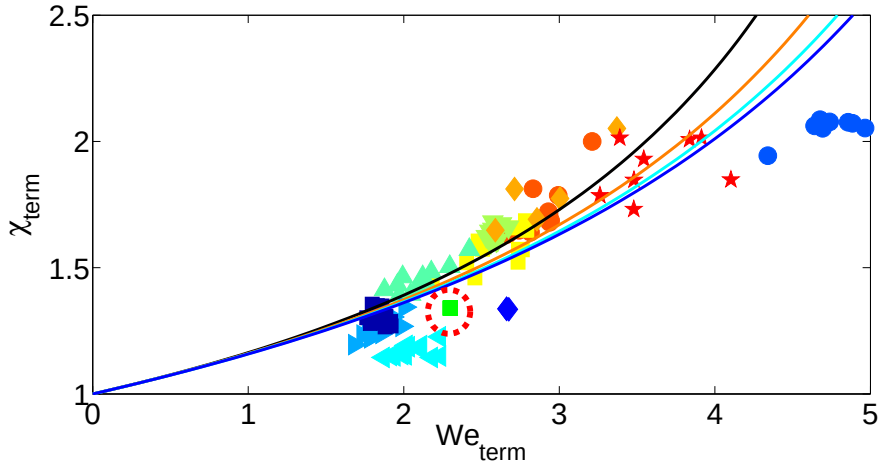

Figure 8.3: Map of terminal Weber numbers, We_{term}, and aspect ratio, χ_{term}, corresponding to the experimental conditions of Table 2.1 and the 2D numerical result associated to the conditions of Table 8.1 (green square). The continuous lines are described in Figure 4.2.

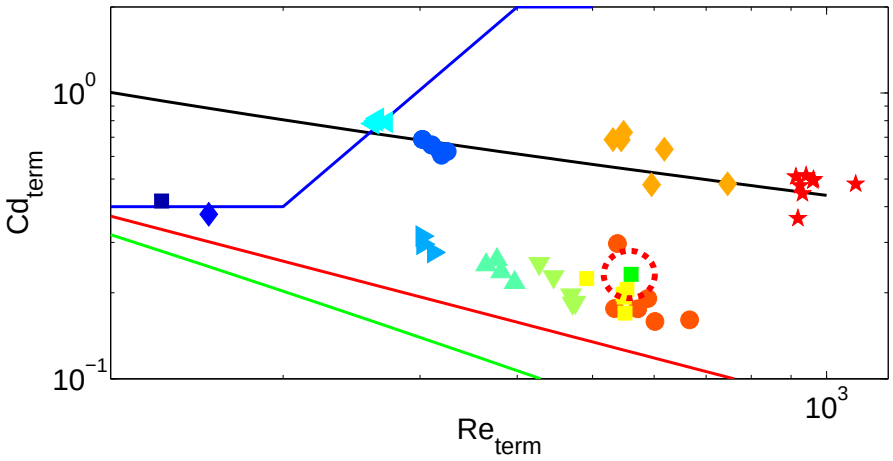

Figure 8.4: Map of terminal drag coefficient, Cd_{term}, and terminal Reynolds number, Re_{term}, calculated from equation (4.3) for the experimental conditions of Table 2.1. The result from the numerical simulation considering the conditions of Table 8.1 (green square). The lines are described in Figure 4.3.

8.3 Results and discussion

8.3.1 Process of the bubble-inclined wall collision

In this section we will simulate the interaction of a 2D bubble with an inclined wall as described in Chapter 7. The interaction of a 20 mm diameter bubble with a wall considering the physical properties of Table 8.1, and the configuration illustrated in Figure 3.2 is simulated. The gravity vector orientation with respect to the vertical direction ranged between 35° and 60°. As detailed in the previous section, the physical parameters were chosen so that the 2D numerical results may be compared to the experimental conditions E10 in Table 2.1.
Images of the bubble contour during the interaction process are shown in Figure 8.5b for the 20 mm 2D diameter numerical bubble and a 35° inclined gravity. Also, images of the contours of a 1.8 mm diameter experimental bubble rising in water, corresponding to experimental conditions E10, are shown in Figure 8.5a. In both figures the free rising phase, the inertial liquid film drainage phase, the lubrication film formation, the restore phase and the bubble bounce are observed. The behavior of the numerical bubble differs only during the bubble bounce. Once the numerical bubble is ejected from the wall and its tails is detached, it stops moving not only normally but also tangentially. This behavior is not observed experimentally as the tangentially velocity diminishes but always maintains a certain value.

Following this arrest, a behavior similar to the composed motion is observed. De Vries et al. (2002) reported this particular motion for the interaction of a bubble with a vertical wall. This phenomenon is attributed to the interaction of the wake and the bubble as it moves away from the wall. As the bubble moves away and tangentially to the wall, the wake reorganizes into a vortex blob at the bubble rear. To illustrate this phenomenon, the vorticity and velocity fields produced numerically at the moment when the bubble changes of direction, compared to the experimental observations, are shown in Figure 8.6. Here the vortex blob appears clearly and confirms the physical explanation of the bubble motion. The generated velocity field is responsible for the strong decrease of the tangential velocity and

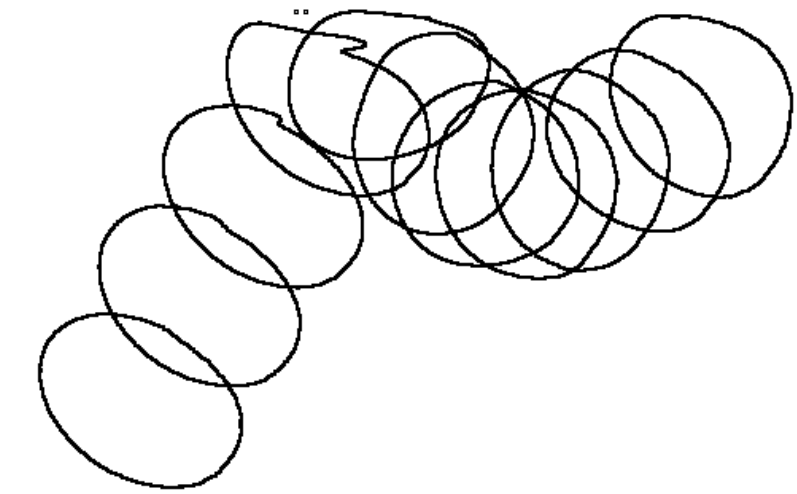

(a)

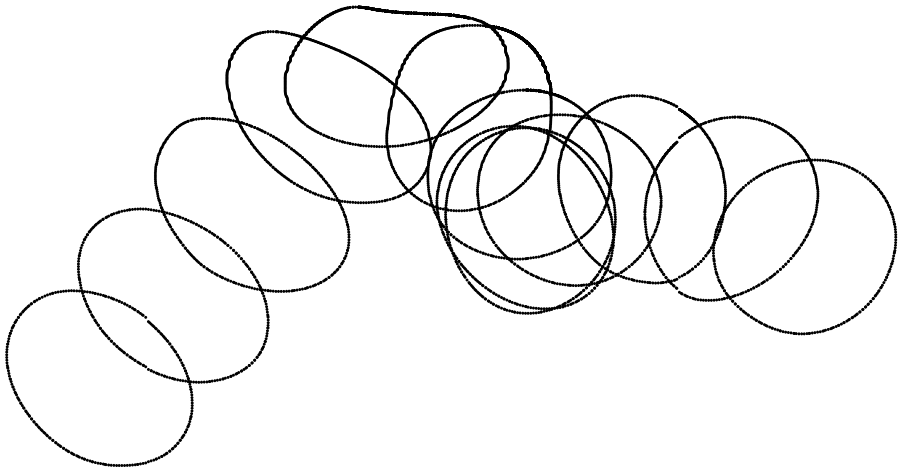

(b)

Figure 8.5: Bubble motion during the collision with a 35° inclined wall for (a) $D_{eq} = 1.9$ mm, $R_{term} = 614$ and $We_{term} = 2.9$, corresponding to experiment E10 conditions, from Table 2.1. Bubble motion during the collision with a wall considering a 35° inclined gravity for (b) 2D bubble with $D_{eq} = 20$ mm, $R_{term} = 560$ and $We_{term} = 2.3$, corresponding to numerical parameters of Table 8.1. The images are composed by superposing bubble positions at different instants with $\Delta t = 4$ ms for the experimental results and $\Delta t = 21$ ms for the numerical results. For the experimental observations, the image was rotated to make the wall appear horizontal.

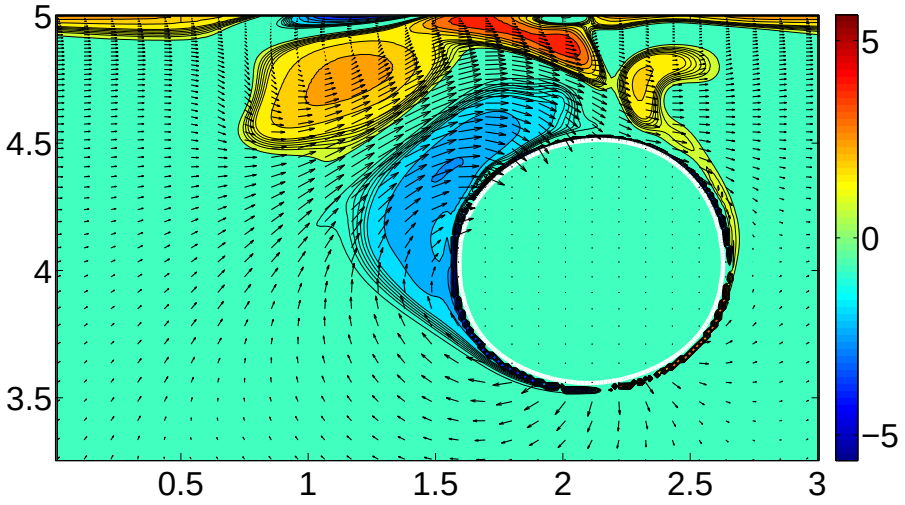

Figure 8.6: Visualization of the 2D bubble wake, through the representation of the velocity and vorticity fields at the beginning of the first bubble bounce, instants before being ejected farer from the wall. The image was plotted at $t\,V_{term}/D_{eq} = 2$ for $\theta = 35°$ and the numerical conditions of Table 8.1. The colors show the value of the vorticity, normalized by V_{term}/D_{eq}.

the larger normal velocity compared with the experiment. In fact, it can be observed that this phenomenon may be accentuated by the liquid flow at the right part of the bubble. Indeed, due to the periodic conditions at the left and right boundaries of the area and the reduced dimensions of the mesh system, part of the bubble wake is present in a zone where the liquid should be at rest. Basically, the velocity and the vorticity of the fluid close to the wall are overestimated. This size limit can explain why this phenomenon appears in the 2D numerical simulations and not in the experimental situation.

The time evolution of the normal position, the aspect ratio, the normal and tangential velocity for the experiment and 2D numerical simulation illustrated in Figure 8.5a and 8.5b are shown in Figure 8.7a, 8.7b, 8.7c and 8.7d, respectively. The numerical parameters evolve in the same way as the experimental data until the beginning of the bounce. At time $t^* \simeq 1.5$, the normal velocity stops decreasing and maintains a constant positive value. Meanwhile the tangential velocity decreases abruptly even reaching negative values. By comparison, the experimental normal velocity keeps on decreasing whereas the tangential velocity is nearly constant. An

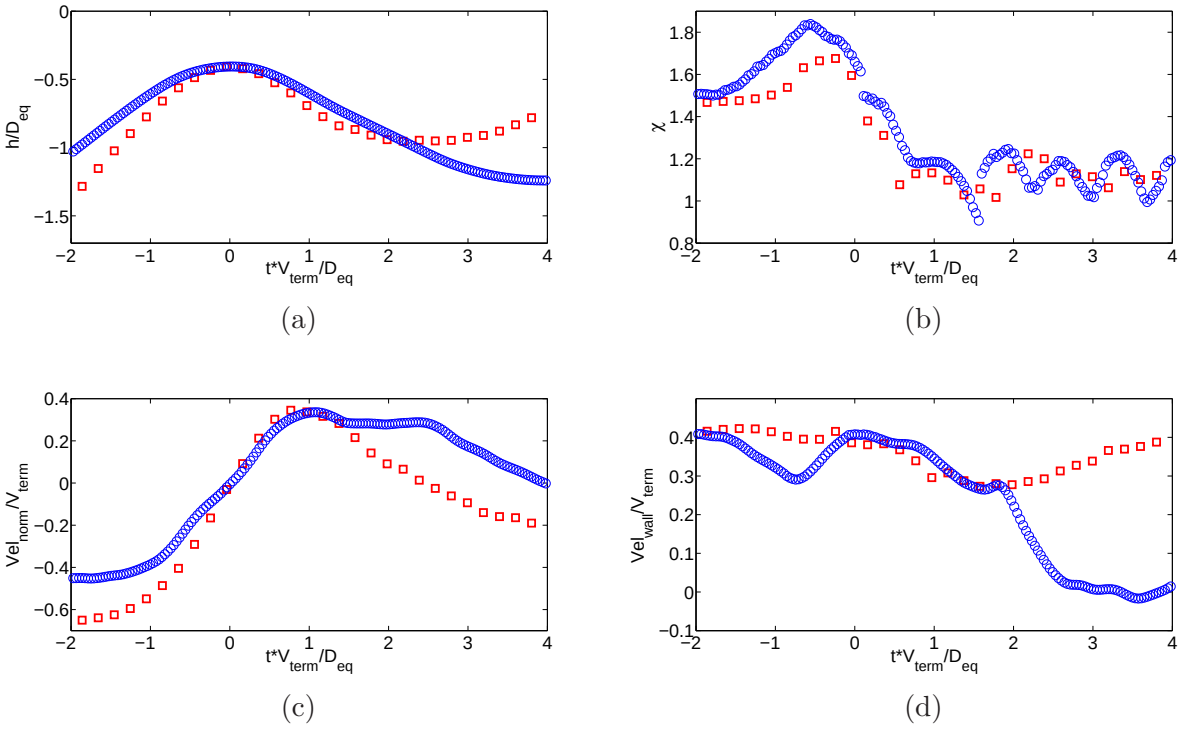

Figure 8.7: Collision of a bubble with a wall inclined of 35° from the horizontal in experimental conditions (red square symbols) $D_{eq} = 1.9$ mm, $Re_{term} = 614$, $We_{term} = 2.9$, corresponding to experiment E10, from Table 7.1 and in 2D numerical simulation (blue symbols) $D_{eq} = 20$ mm, $Re_{term} = 560$, $We_{term} = 2.3$, corresponding to conditions of Table 8.1. Evolution of (a) the normalized distance between the bubble centroid and the wall, h/D_{eq}, (b) the aspect ratio, χ, (c) the normalized normal velocity of the bubble, V_{norm}/V_{term} and (d) the normalized tangential velocity of the bubble, V_{wall}/V_{term} as a function of normalized time, tD_{eq}/V_{term}, for the experiment and simulation shown in Figure 8.5a and Figure 8.5b respectively.

interesting point to note is that this change of behavior occurs as soon as the lower interface of the bubble reaches the zone of constant mesh size ($h \geq D_{eq}$). Hence, a second element of response for the different behavior is a large mesh size that may result in inexact velocities in the front part of the bubble during its bounce. This fact affects not only the negative part of the vortex blobs but also the lift and drag forces.

The evolution of the normal position, aspect ratio, normal and tangential velocities with the inclination angle is reported in Figure 8.8a, 8.8b, 8.8c and 8.8d, respectively. The figures are color coded according to the inclination angle. In the same way as for the evolution

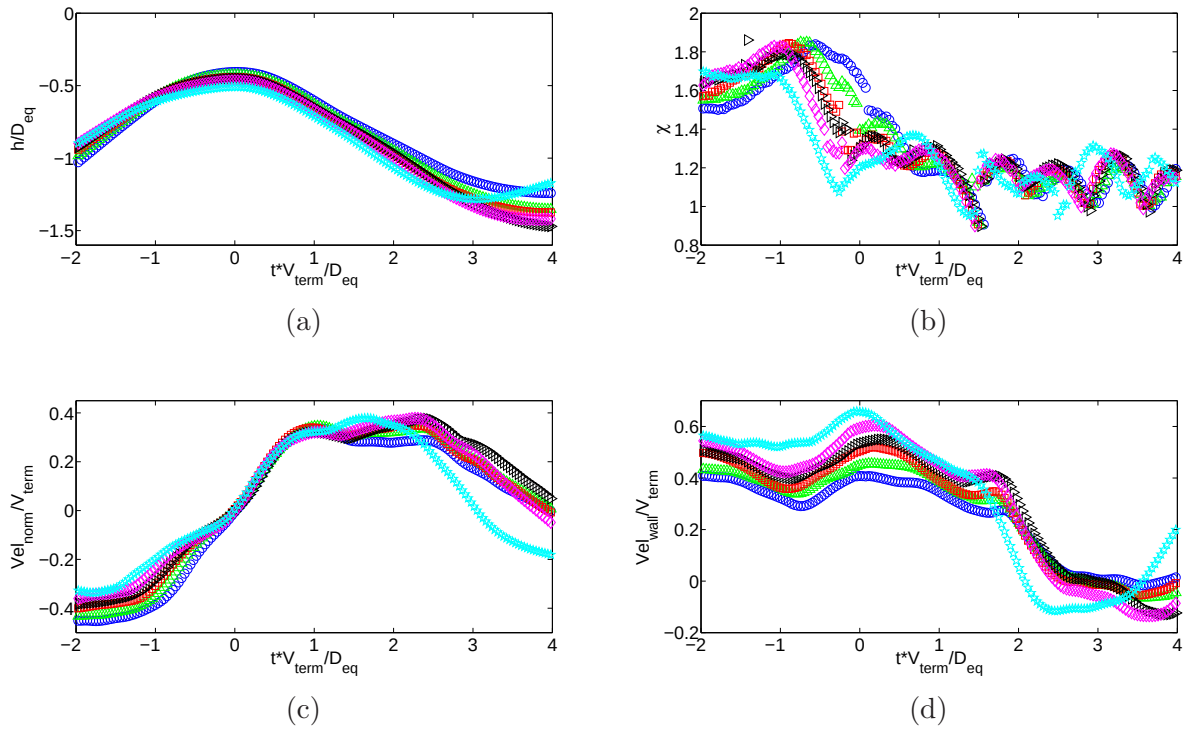

Figure 8.8: Collision of a bubble with a wall inclined of 35°, 40°, 45°, 50°, 55° and 60° from the horizontal plotted in blue, green, red, black, magenta and cyan symbols respectively. The bubble interacts with the wall in 2D numerical simulation with $D_{eq} = 20$ mm, $Re_{term} = 560$, $We_{term} = 2.3$. Evolutions of (a) the normalized distance between the bubble centroid and the wall, h/D_{eq}, (b) the aspect ratio, χ, (c) the normalized normal velocity of the bubble, V_{norm}/V_{term}, (d) the normalized tangential velocity of the bubble, V_{wall}/V_{term}.

reported in Chapter 7 the maximum aspect ratio tends to decrease with the inclination angle. Considering also the comparison with the experimental case of Figure 8.7b, the numerical reproduction of the shape evolution during the collision process is considered satisfactorily reproduced by the code. A second important aspect of the collision process is the contact time (equation (7.3)). Considering that this time begins with the inertial drainage of the liquid film and ends with the wall impulse, the contact time is $-1.5 \leq t^* \leq 1$ for all the inclination angles. During this period, the tangential and normal velocities reproduce the qualitative evolution with respect to the inclination angle observed experimentally. Finally all the phases of the tangential velocity evolutions described in Chapter 7 (inertial drainage, first rotation, capillary response, second rotation and tail detachment) are observed numerically.

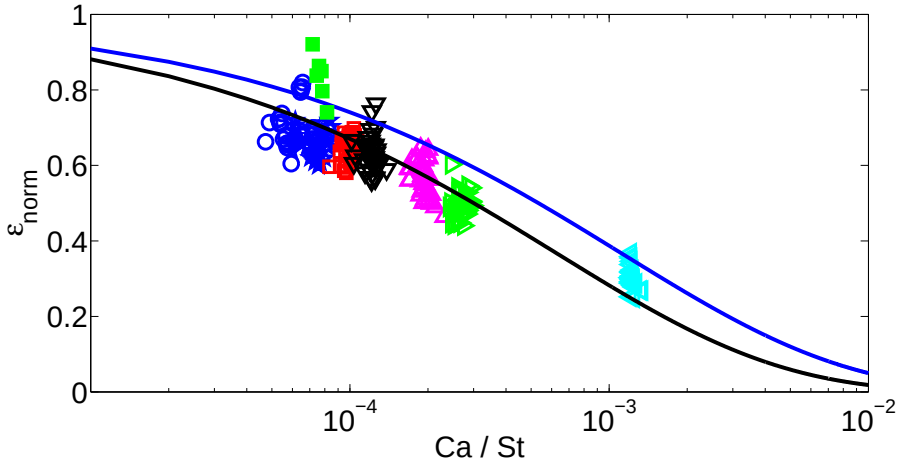

(a)

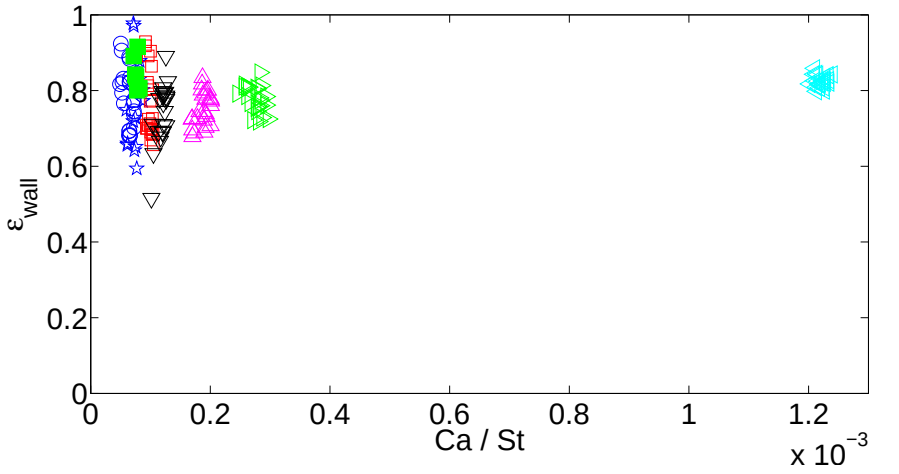

(b)

Figure 8.9: Normal ϵ_{norm} (a) and tangential ϵ_{wall} (b) coefficients of restitution evolutions respectively as a function of the ratio of the capillary number and the modified Stokes number Ca/St. The experimental results are plotted according to the symbols of Table 7.1. The blue line corresponds to expression (7.17) while the black line corresponds to a fit of expression (7.16) and the 2D numerical results are plotted using green squares.

Based on the satisfactory reproduction of the collision process, the tangential and normal coefficient of restitution evolutions with respect to Ca/St are plotted in Figure 8.9a and 8.9b, respectively. The experimental results obtained with the experimental conditions of Table 7.1 are also reported considering only the data obtained when $\theta \geq 35°$. The normal coefficient of restitutions are in agreement with the corresponding experimental data, E12 in Table 7.1. Even if a larger coefficient of restitution is observed, an agreement with the expression proposed by Zenit and Legendre (2009) (blue line) obtained for a higher framing rate is obtained. Indeed, Zenit and Legendre (2009) studied the collision process with a higher framing rate (3000 rates per seconds) and obtained an equivalent evolution of the coefficient of restitution as a function of Ca/St but with larger values. The 2D numerical results reproduce the normal behavior of the bubble during the oblique collision well. The range of tangential Weber numbers (We_{wall}) generated through the simulations is smaller than the range produced experimentally. However, a good agreement with the experimental trend is observed. Data for larger range of tangential Weber number are necessary to further validate the agreement with 2D simulations. As well, a larger range of data either 2D and 3D numerically or experimentally would clarify the physics and allow the formulation of a theoretical model for the tangential coefficient of restitution. The accuracy of the JADIM code to reproduce the oblique collision process is therefore confirmed in the normal as well as the tangential direction. Nonetheless an improvement of the mesh configuration far from the wall is necessary to reproduce correctly the bounce motion of the bubble.

8.3.2 Steady motions of the bubble

In this section we use the numerical code to study the case of the 2D bubble in its steady motion, whether it corresponds to the sliding motion or the bouncing motion. Given the size of the numerical bubble, much larger tangential velocity were obtained in comparison to the experimental results of E10. Hence the numerical and experimental results are compared through the dimensionless velocity evolution, $V^*_{wall} = V_{wall}/V_{term}$, with the inclination angle

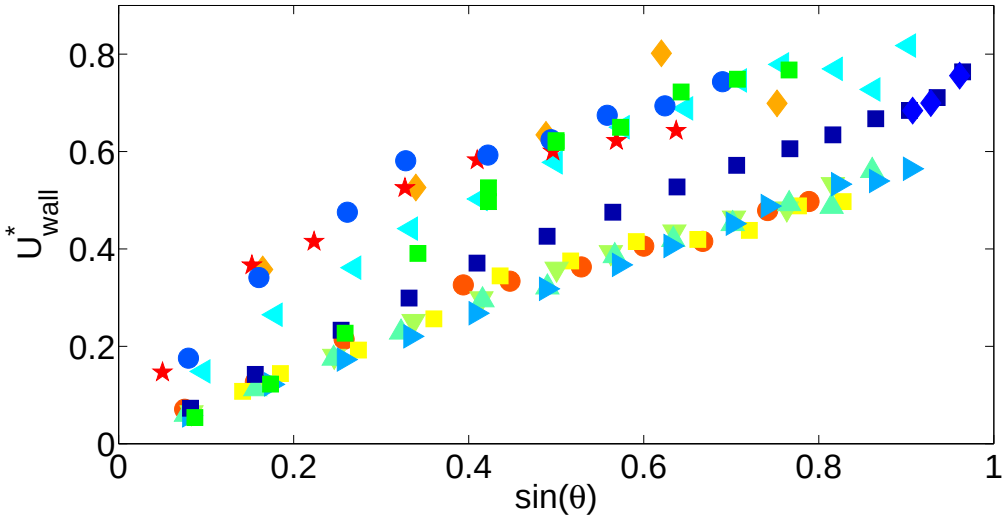

Figure 8.10: Sliding bubble dimensionless velocities, $V^*_{wall} = V_{wall}/V_{term}$, is plotted as a function of $sin\theta$, where θ is the inclination of the wall with respect to the horizontal direction, for all the experimental conditions of Table 2.1 using green squares.

in Figure 8.10. It is interesting to note that experimental data of the different physical parameters of Table 2.1, never cross each other along their evolution with the inclination angle. As for the numerical simulations, the obtained sliding velocity is close to the results of experimental spherical shape bubbles at low inclination angles and evolves toward the velocities evolutions of deformed bubbles as the inclination angle increases.

According to the results shown in Chapter 6, the shape of the 2D sliding bubble gives an indication on which regime controls the sliding bubble motion. The shape of the sliding bubble is shown in Figure 8.11 for three different inclination angles. In this same figure the shape of the bubble in experimental conditions E10 is reported for the same inclination angles. In line with the observations of section 8.3.1, good agreement is observed. In particular, a small deformation of the bubble along the axis normal to the wall is observed for all the sliding motions. Hence considering Chapter 6, the numerical bubbles should slide according to the gravity-dominated deformation regime associated to a spherical shape. The evolution of the tangential capillary number Ca_{wall} with $Bo\,sin(\theta)$ for the numerical simulations is presented together with the experimental data of Table 2.1 in Figure 8.12. The numerical

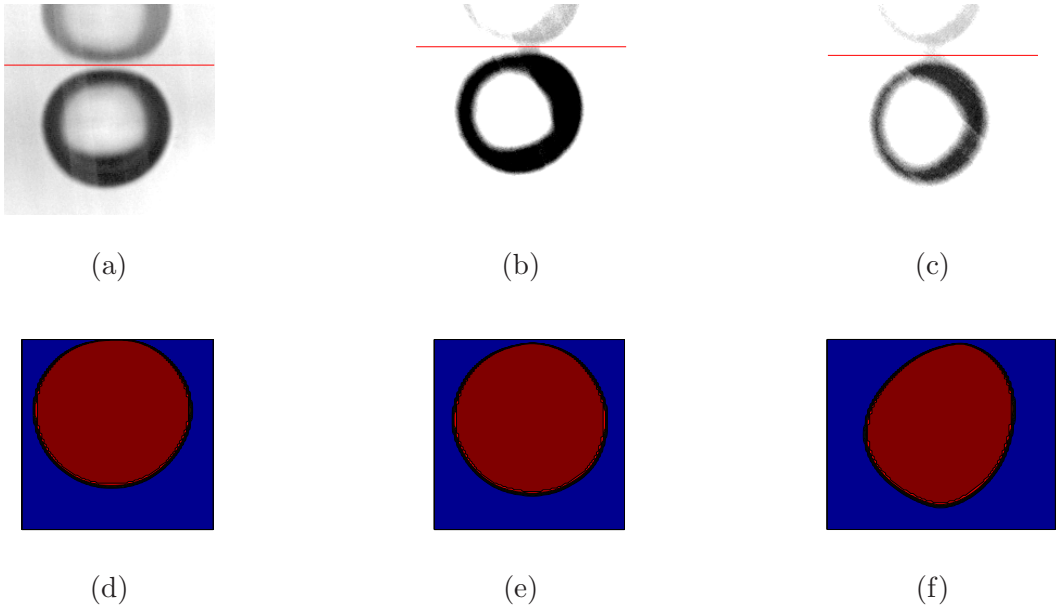

Figure 8.11: Images for the sliding bubbles shape evolution at different inclination angles in numerical conditions of Table 8.1 upper row and experimental conditions E10 lower row. The experimental and numerical data associated to the different images are: (a) $\theta = 5°$, $Re_{wall} = 42$, $We_{wall} = 0.01$; (b) $\theta = 25°$, $Re_{wall} = 188$, $We_{wall} = 0.29$; (c) $\theta = 50°$, $Re_{wall} = 345$, $We_{wall} = 0.73$; (d) $\theta = 5°$, $Re_{wall} = 30$, $We_{wall} = 0.06$; (e) $\theta = 25°$, $Re_{wall} = 278$, $We_{wall} = 0.56$; (f) $\theta = 50°$, $Re_{wall} = 420$, $We_{wall} = 1.29$;

data evolve according to the blue linear dependence as the experimental data. This result confirms not only the gravity-dominated deformation regime analysis of the sliding bubbles but also a similar evolution for 2D bubbles. The sliding motion is controlled by the balance between viscous drag force and the buoyancy force. Figure 8.13 shows the experimental drag coefficient of the sliding bubbles whose motion is controlled by the viscous regime. As shown in Figure 8.13, equation (6.20) agrees well with the numerical drag coefficient for the spherical sliding bubbles. The different trend between these two equations confirms the existence of two dynamic regimes for the gravity-dominated deformation depending on whether the sliding bubble is spherical or deformed.

Considering now the transition between sliding and bouncing motion, the wake of the bubble controls the transition. As detailed in Chapter 5, the wake generated at the rear of the bubble during its sliding motion induces a lift force on the bubble. This repulsive lift force balances the buoyancy force; when it becomes larger than the normal component of the buoyancy force, the transition is observed. The 2D vorticity field around the sliding bubble in experimental condition E10 against a 50° inclined wall, obtained experimentally is shown in Figure 8.14b. The vorticity field obtained numerically for a bubble sliding against a 50° inclined wall with the configuration detailed in Table 8.1 is presented in Figure 8.14a. Similarly to the experiments, the numerical vorticity field shows important vortex shedding in the bubble wake. Yet the asymmetry is much more pronounced compared to the experimental observations because of the weak production of negative vorticity on the side opposite to the wall. To clarify this difference the time evolution of the vorticity field during the wake formation, while the bubble is sliding, is presented in Figure 8.15. Images are separated by a constant time interval of 84 ms. The flow field close to the wall in front of the bubble remains important during the whole process of wake formation. This flow results actually from the limited dimensions of the mesh system and the periodic condition at the left and right boundary of the domain. The value of the wake induced lift force is also affected by the vorticity intensity at the rear of the bubble resulting from the interaction of the front

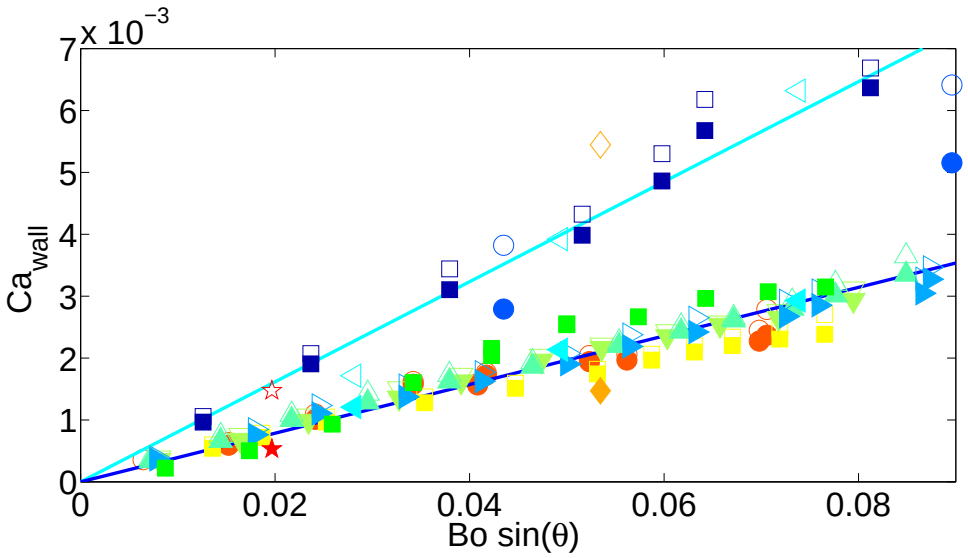

Figure 8.12: Map of wall capillary number, Ca_{wall}, and projected Bond number, $Bo\,sin\,\theta$, calculated for the experimental conditions of Table 2.1 and plotted according to the corresponding symbol codes as well as the numerical results plotted using green squares. The blue and cyan continuous lines correspond to a fit of the spherical and deformed bubbles data respectively with a linear trend. This figure represents the Stokes force term as a function of the buoyancy term in equation (6.6)

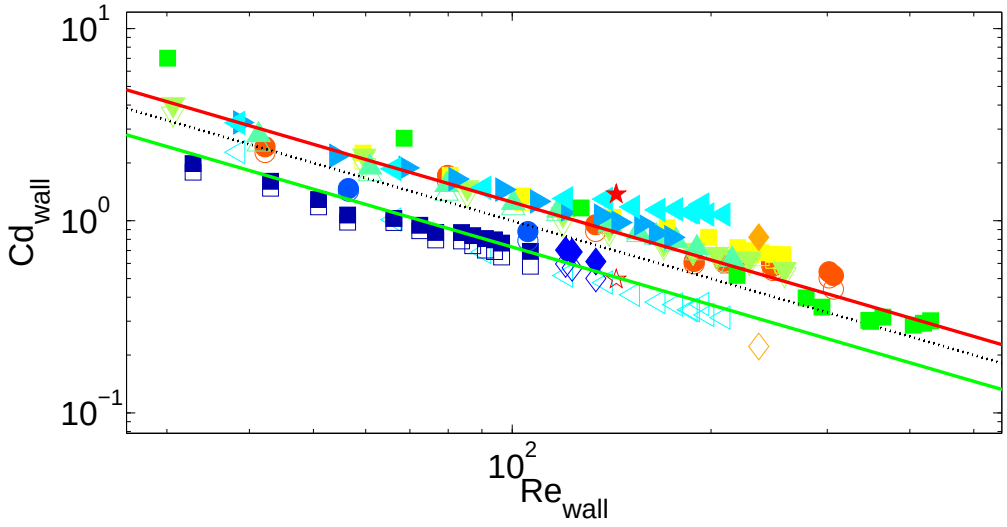

Figure 8.13: Map of wall drag coefficient, Cd_{wall} as defined in equation (6.19), and wall Reynolds number, Re_{wall}, calculated for the experimental conditions of Table 2.1 that belong to the viscous regime ($\chi_{wall} > 1$) and plotted according to the corresponding symbol codes as well as the numerical data of Table 8.1. The theoretical lines are explained in detail in the legend of Figure 6.10.

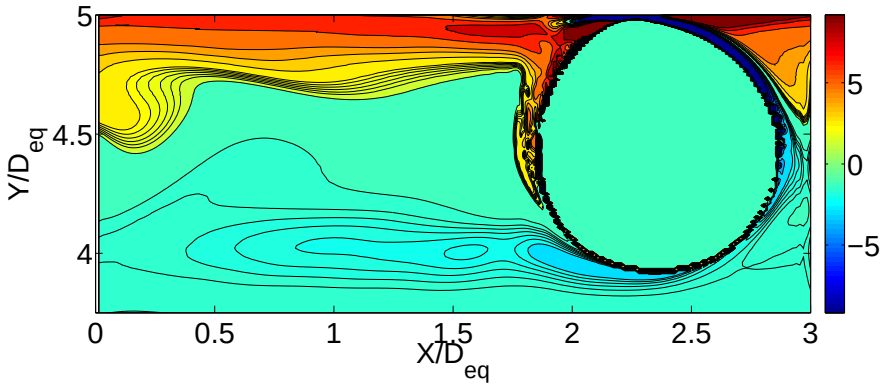

(a)

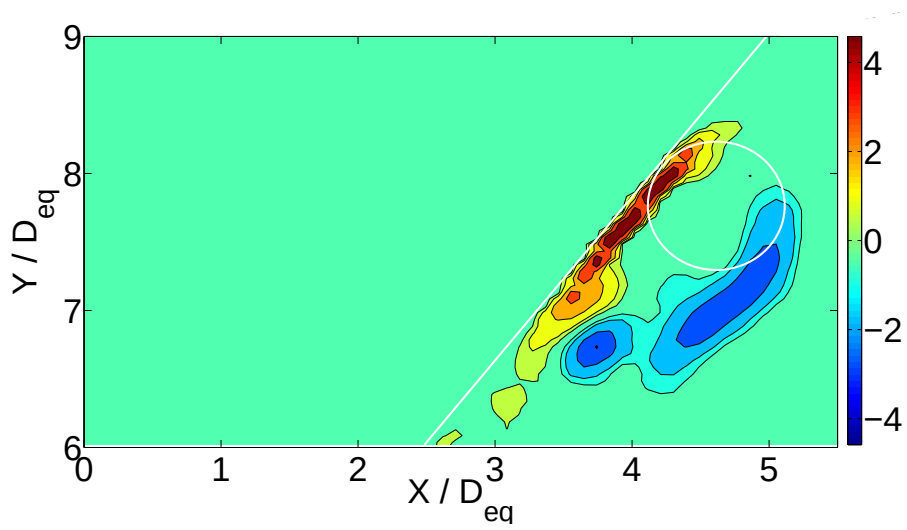

(b)

Figure 8.14: Visualization of the bubble wake for a sliding bubble, slightly below the transition angle ($\theta = 50°$ in numerical and experimental cases). The images was taken at steady sliding (a) $tV_{term}/D_{eq} = 37$ for the numerical conditions of Table (8.1) and $\theta = 50^o$ and (b) $tV_{term}/D_{eq} = 54$ for E10 in Table (2.1) and $\theta = 50°$. The colors show the value of the vorticity, normalized by V_{term}/D_{eq}.

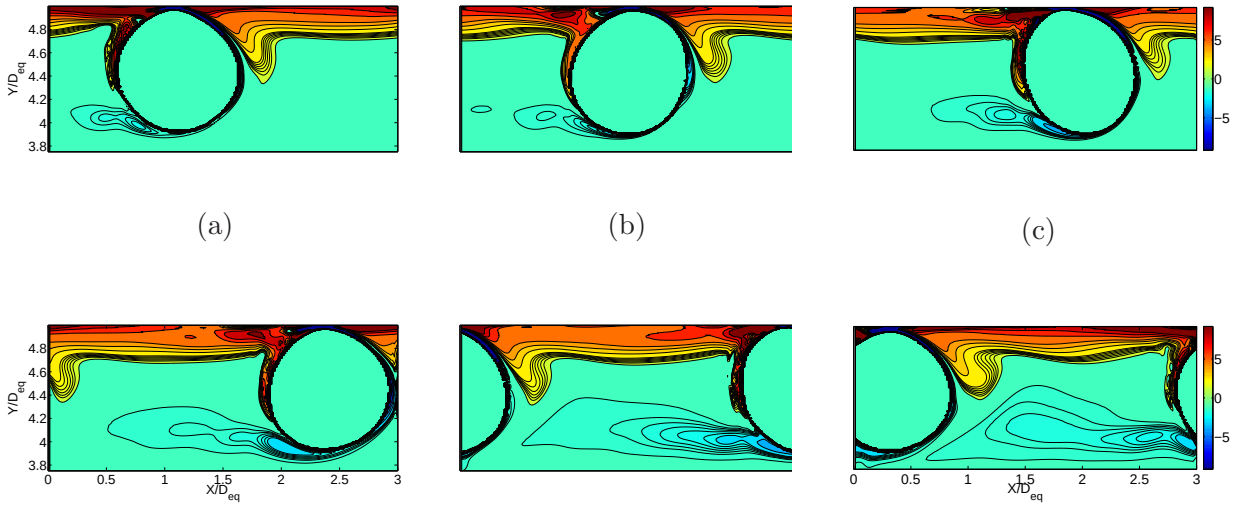

Figure 8.15: Temporal evolution of the bubble wake formation for a sliding bubble, slightly below the transition angle ($\theta = 50°$ in numerical and experimental cases). The images was taken at steady sliding motion with a constant space time $\Delta t = 84ms$ for the numerical conditions of Table (8.1). The colors show the value of the vorticity, normalized by V_{term}/D_{eq} .

flow with the rear flow due to periodic boundary conditions. The vorticity production is affected in the same way but without the confinement effect of the wall. As a result, the wake effect responsible for the transition of regime is not represented through the present numerical configuration because it reproduces a bubble line sliding under the wall. The criteria of transition proposed in Chapter 5 is not reproduced in 2D simulation as observed in Figure 8.16. We can see there that the transition occurs for a larger inclination angle than the proposed condition. In other words, the lift force is underestimated considering a periodic 2D bubble line configuration. With regard to the bouncing motion, a small wall Reynolds value is then reported in Figure 8.15.

In Figure 8.17a and Figure 8.17b the time evolution of the normal position and tangential velocity of the 20 mm diameter bubble interacting with a wall considering a 55° inclined gravity is plotted. Clearly the mean tangential velocity reported is affected by the mesh size far from the wall. A strong decrease of the tangential velocity at the beginning of each

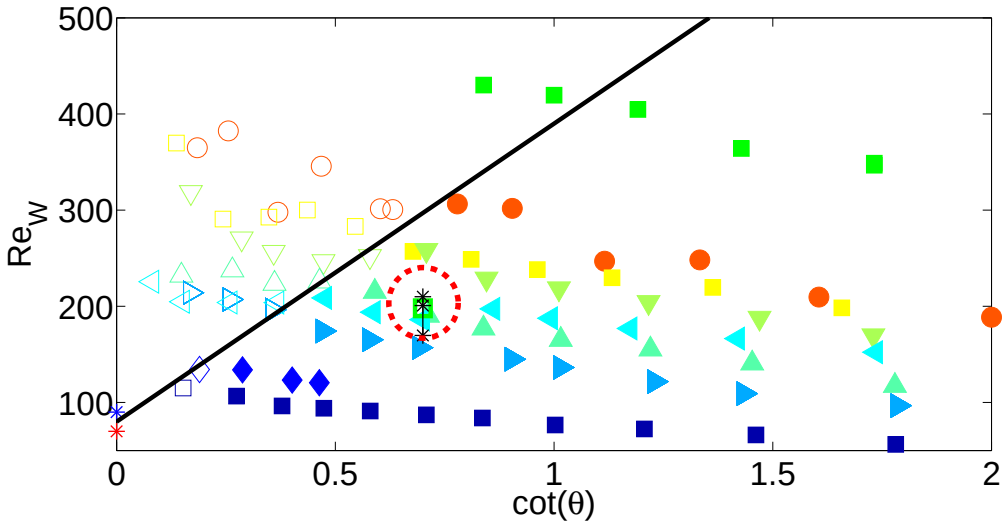

Figure 8.16: Conditions for transition for the viscous regime of motion: Re_{wall} as a function of $\cot\theta$. The symbols are according to Table 2.1 and Table 8.1. In all cases, the filled and empty symbols show the experiments in which sliding or bouncing was observed, respectively. The black stars are the data from Tsao and Koch (1997); the $(*)$ and $(\times)$ symbols are results from Takemura and Magnaudet (2003) and De Vries et al. (2002), respectively. The black line corresponds to Eqn.(5.4).

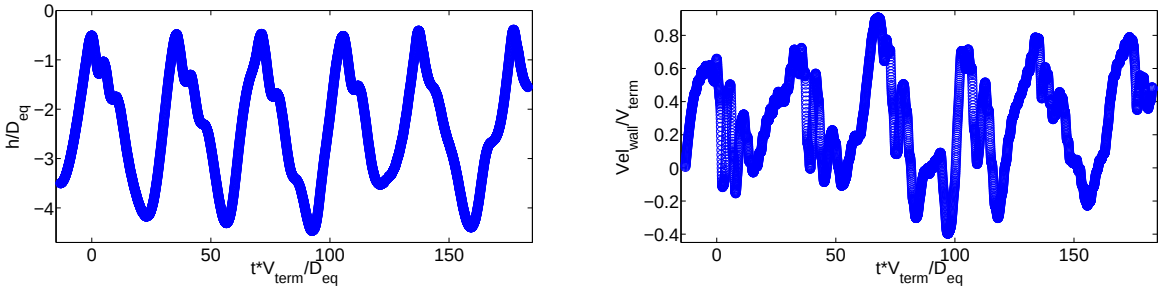

(a) (b)

Figure 8.17: Numerical collision of a bubble with a wall inclined of 60° from the horizontal in conditions $D_{eq} = 20$ mm, $Re_{term} = 560$, $We_{term} = 2.3$, corresponding to conditions of Table 8.1. Evolution of (a) the normalized distance between the bubble centroid and the wall, $h/D_{eq}$and (b) the normalized tangential velocity of the bubble, V_{wall}/V_{term} as a function of normalized time, tD_{eq}/V_{term}.

bounce results in the small wall Reynolds number value observed in Figure 8.16 due to the bubble line interaction.

8.4 Conclusion and future work

The interaction of a 2D 20 mm diameter bubble with a wall, considering a gravity inclination varying from 5° to 60° from the vertical have been simulated. The physical parameters of the problem (ρ_l, ρ_l, μ_l, μ_g, σ, g) were chosen such that the Morton and Bond numbers were the same as those of a 1.8 mm real bubble in water corresponding to experimental conditions E10. In this way the 2D numerical simulation may be compared to the experimental results of E10 to evaluate the capacity of the 2D simulation to reproduce the main behaviors observed in experiments. In some simulations the bubble reached the wall with a certain inertia whereas in other simulations the bubble initiated its motion close to the wall.

With regard to the oblique collision process, the phases of inertial liquid drainage, lubrication film formation, capillary response and restitution, as detailed in Chapter 7, were well reproduced. Apart from the different phases, agreement is also obtained with the experimental normal coefficient of restitution and expression proposed by Zenit and Legendre (2009). As for the tangential coefficient of restitution, despite the different range of tangential Weber number produced, the 2D numerical results followed the trend observed experimentally. Different physical parameters will be considered in the future to generate the correct range of tangential Weber number. In contrast, during the bouncing motion when the bubble interface achieves a certain mesh size, the mesh refinement is no longer satisfactory and the lift force acting on the bubble is overestimated. Therefore whether to reproduce the first bounce or the steady bouncing motion of the bubble, the numerical configuration is here describing a bubble line due to the periodic condition. A new mesh system that consists in a much smaller mesh size far from the wall and of larger extend in the direction parallel to the wall has to be considered to obtain the bouncing motion of a single bubble.

The sliding motion of the bubble reproduced closely the behavior of the 1.8 mm diameter bubble in water. The bubble slides according to the viscous regime scaling law and the evolution of its drag coefficient was fitted by the model established in Chapter 6. Due to a mesh length smaller than the bubble wake extend, the liquid located in front of the bubble during its sliding motion is still in motion as part of the wake whereas it is at rest experimentally. The negative vorticity production at the bubble side opposite to the wall extends on a distance larger than the mesh system width. The wake induced lift force is clearly affected and the transition criteria established in Chapter 5 is then impacted.

Chapter 9

Conclusions and perspectives

9.1 Conclusions

The aim of the thesis was to study the interaction of a bubble with an inclined wall. It is partly motivated from the transition of behavior observed by Tsao and Koch (1997) for a bubble in water. The steady motion of the bubble passes from a sliding motion to a periodical bouncing motion as the inclination angle increases. Despite the presence of similar transitions in a large number of situations, no clear conditions of transition have been proposed to date. The second objective of the thesis was to extend the idea of Zenit and Legendre (2009) to characterise the bubble-wall collision process through a coefficient of restitution to the inclined wall configuration.

An experimental setup was designed to produce the interaction of a bubble, in its terminal state conditions, with an inclined wall in a viscous fluid. The bubble shape and motion were observed with a high speed camera. The PIV technique was used to quantify to the flow field generated in the fluid during the interaction. Experiments were conducted for a wide range of liquid-bubble properties and a wall inclination angle ranging from 5° to 80°. Accordingly, an extended range of dimensionless numbers was obtained. The numerical code JADIM was used to also study the interaction process in a 2D geometry. The JADIM code used for the

thesis is based on a second order space and time finite volume method. The simulations were conducted using a fixed non uniform Cartesian mesh system. Considering a fine mesh refinement close to the wall, the interaction between the bubble interface and the pressure film was reproduced accurately.

When the bubble interacts with the inclined wall at a terminal state conditions, it eventually reaches a new steady state. This steady motion depends exclusively on the wall inclination and the bubble-liquid properties. Based on the wide range of experimental conditions considered here, a criteria for the transition between the sliding motion and the collisional mode motion is proposed. Considering a simple force balance on the sliding bubble, the wake induced lift force is balanced with the normal buoyancy in the normal direction. Hence, the transition of behavior occurs when this lift force is higher than the buoyancy force. Two regimes of transition were found according to the bubble deformation. For small deformations, the drag force is scaled by a viscous law. As a result, a linear relation between the tangential Reynolds number and the cotangent of the inclination angle defines the limit of regimes of motion. Conversely, when a large deformation of the bubble is observed, the drag force is scaled with an inertial law. Hence, a constant inclination angle is predicted for the transition. Both conditions were validated with the experiments. The same force balance was applied along the tangential direction for the study of the sliding motion. Again, two behaviors were found depending on whether the viscous or inertial regimes controlled the bubble motion. A new definition of the aspect ratio is introduced to discern the two regimes of motion. This wall aspect ratio is calculated using the bubble axes perpendicular and parallel to the wall instead of the major and minor axes respectively. Accordingly, when the shape of the sliding bubble is associated to wall aspect ratio smaller than one, a viscous law scales the drag force. Conversely, an inertial drag force is used in the force balance when the wall aspect ratio is larger than a unity. For the viscous regime of motion, the force balance proposed by Aussillous and Quéré (2002) is applied and a linear relation between the wall capillary number and the tangential Bond number is obtained. In view of the ex-

perimental conditions, the results differed from the theory because of the bubble interface contamination and the bubble deformation. Considering corrections for the bubble velocity based on the expressions of Schiller and Naumann (1933) and Moore (1965) respectively, the corrected velocities agreed well with the theoretical expression. Based on the viscous nature of the drag force, a model of the drag coefficient based on the additive contribution of the potential-flow correction and the drag correction due to the vorticity production at the wall is proposed. For the inertial regime of motion, the force balance shows a constant tangential Froude number associated to the sliding motion. Accordingly, a constant drag coefficient is observed. The same inertial behavior was observed for the bouncing motion of the bubble. A detailed analysis of the tangential velocity showed that its time evolution is controlled by the lift, drag and buoyancy forces. Regarding the bouncing motion, the inertial force balance is considered. However, the bouncing motion of the bubble is explored for contaminated and strongly deformed bubbles. Therefore, the associated corrections have to be applied to the experimental results to obtain a constant drag coefficient.

The process of collision of a bubble, in its terminal state conditions, with an inclined wall is also studied. First, a careful analysis of the different phases of the process was proposed considering the high speed camera visualizations. Before the bubble impacts the wall, its velocity begins to decrease under the inertial liquid film drainage effect. Once the bubble impacts the wall, the lubrication film is formed. After a certain time, and while the bubble is rotating, its shape evolves toward a spherical shape. Once the major axis of the bubble aligns with the wall direction the restore phase begins. During this phase, the bubble is pushed normally and rotates in the opposite direction. This second rotation results in a decrease of the lubrication film size. The wall impulse stops when the major axis of the bubble is aligned with the normal direction. Due to the normal and tangential velocities evolutions during these phases, the beginning of the liquid film inertial drainage and the end of the wall impulse are chosen as initial and final times for the oblique collision process. Because of the wall inclination and the 2D and 3D bubble trajectories before the collision, a normal

and a tangential coefficient of restitutions have to be considered. The normal coefficient of restitution, based on the normal velocity evolution scaled with Ca_{norm}/St^*_{norm} matching the results of Zenit and Legendre (2009). A model, based on a mass spring system, was established for the normal collision of a bubble with a horizontal wall. The tangential coefficient of restitution is an indirect measure of the energetic dissipation from the competition between the bubble inertia and its surface energy. Thus, the tangential Weber number is the correct dimensionless number to characterize the tangential coefficient of restitution. Despite the experimental uncertainty, a constant tangential coefficient of restitution was observed.

Finally, in the last part of the thesis the capacity of 2D numerical simulation to reproduce the bubble-inclined wall interaction was tested. The 2D simulation of the interaction was conducted in equivalent conditions as the experimental data. Excellent reproductions of the sliding motion and the collision process were obtained. The simulation parameters were chosen in such a way that the viscous regime controls the sliding motion. On the other hand, the 2D simulations were not able to completely reproduce the condition of transition and the bouncing motion. One problem resulted from the limits of the mesh size and the second was attributed to the periodic boundary condition. First the dimension of the area did not allow the wake to develop completely and the simulation reproduced a 2D bubble line configuration. Provided a new mesh system adapted to the problem, the 2D simulation are expected to reproduce the bubble-inclined wall interaction correctly.

9.2 Perspectives

The problem on the transition of behavior addressed by Tsao and Koch (1997) has been satisfactorily answered. However, as it happens for almost all research project, the resolution of one problem lead to many new questions. In particular, one major phenomenon that remains unexplained is the composed bouncing motion. Already reported by De Vries et al. (2002), this strange bubble motion is likely to be explained using numerical simulations. We foresee

the wake configuration to be the key to answer that problem. The transition from sliding to bouncing, as well as their respective motions, have each been characterised depending on whether the viscous or inertial regime controlled the bubble motion. Accordingly, a new problem is to determine which regime the bubble belongs to. Though the mean tangential behavior of the sliding bubbles have been explained, the collisional modes have hardly been solved. Data of collision frequency, bounce amplitudes or coefficient of restitution for example still have to be studied in detail. A wider range of dimensionless parameters has to be considered, numerically or experimentally, to complete the study of the phenomenon. The oblique collision study is only a first step toward the formulation of a theoretical model for the tangential coefficient of restitution. 3D Numerical simulations will be the key to measure the flow details not accessible in experiments. Finally, the inertial liquid film drainage theory of Zenit and Legendre (2009) could be extended to also account for the tangential motion of the bubble.

Nomenclature

α_k	Runge Kutta scheme coefficient
β	Angle between the bubble major axis and the wall direction
β_k	Runge Kutta scheme coefficient
χ_{term}	Free rising bubble aspect ratio
χ_{wall}	Steady bubble-wall aspect ratio
$\Delta x_{i,j}$	Horizontal dimension of the mesh i,j
$\Delta y_{i,j}$	Vertical dimension of the mesh i,j
ϵ_{norm}	Coefficient of restitution based on the normal velocity
ϵ_{wall}	Coefficient of restitution based on the tangential velocity
η	Normal deformation of the bubble during the collision
γ_k	Runge Kutta scheme coefficient
κ^{-1}	Capillary length
λ	Length of the curved part of the sliding bubble interface
μ	Dynamic viscosity
ν	Kinematic viscosity

ν_b Bubble volume

ω Fluid vorticity

ϕ Potential solution of the Poisson equation

ρ Liquid Density

ρ_S Solid particle density

σ Surface tension

$\Sigma_{i,j}$ Viscous stress tensor

$\tau_{i,j}$ Stress tensor

θ Inclination angle of the wall with respect to the horizontal direction

θ_{trans} Inclination angle of transition of regime of steady-state bubble motion

φ Level set function

ξ_i Physical coordinates

ζ_k Runge Kutta scheme coefficient

C_{AM} Added mass coefficient

Ca_{term} Free rising bubble Capillary number

Ca_{term} Steady bubble-wall Capillary number

Cd_{term} Free rising bubble drag coefficient

Cd_{wall} Steady bubble-wall drag coefficient

D_{eq} Bubble equivalent diameter based on a sphere with the same volume

d_{ma} Bubble equivalent ellipsoid major axis

d_{mi} Bubble equivalent ellipsoid minor axis

$E_{\Delta,S}$ Bubble surface energy

E_D Bubble dissipated energy

E_k Bubble kinetic energy

$F_{\sigma,S}$ Numerical Capillary force

h_{film} Thickness of the lubrication film

H_j Numerical terms of curvature

k_d Empirical correction coefficient for the drag coefficient of a bubble due to interface contamination

l_{film} Length of the contact between the liquid and the bubble interface

m^* Total mass involved by the collision of a bubble/drop

Re_{term} Free rising bubble Reynolds number

Re_{wall} Steady bubble-wall Reynolds number

St^*_{norm} Modified Stokes number based on the normal velocity

St^*_{wall} Modified Stokes number based on the tangential velocity

V_{bounce} Bubble velocity after impacting the wall

$V_{contact}$ Bubble velocity before impacting the wall

V_{norm} Bubble velocity in the direction normal to the wall

V_{term} Free rising Bubble velocity

V_{wall} Bubble velocity in the direction tangential to the wall

We_{term} Free rising bubble Webber number

We_{wall} Steady Bubble-wall Webber number

n Normal Vector

t Tangential vector

A Bubble interface area

Bo Bond Number

C VoF function, volume fraction

G Moore correction coefficient for the drag coefficient of a bubble due to its deformation

g Gravity acceleration

h Distance between the bubble centroid and the wall

Mo Morton number

p Pressure

t Time

W Interface velocity

List of Figures

List of Tables

Bibliography

Abadie, T. (2013). *Hydrodynamics of gas-liquid Taylor flow in microchannels*. PhD thesis, Institut National Polytechnique de Toulouse.

Abadie, T., Aubin, J., and Legendre, D. (2015). On the combined effects of surface tension force calculation and interface advection on spurious currents within volume of fluid and level set frameworks. *J. Comp. Phys.*, 297:611–636.

Aussillous, P. and Quéré, D. (2002). Bubbles creeping in a viscous liquid along a slightly inclined plane. *Europhysics Letters*, 59:370–376.

Barnocky, G. and Davis, R. H. (1988). Elastohydrodynamic collision and rebound of spheres: experimental verification. *Phys. Fluids*, 31:1324–1329.

Calmet, I. (1995). *Analyse par simulation des grandes échelles des mouvements turbulents et du transfert de masse sous une interface plane*. PhD thesis, Institut National Polytechnique de Toulouse.

Calmet, I. and Magnaudet, J. (1997). Large eddy simulation of high-schmidt-number mass transfer in a turbulent channel flow. *Phys. Fluids*, 9:438–455.

Canuto, C., Hussaini, M., Quarteroni, A., and Zang, T. (1988). *Spectral method in Fluid Dynamics*. Springer Series in Computational Physics, Springer-Verlag.

Clift, R., Grace, J., and Weber, M. (1978). *Bubbles, Drops, and particles*. Academic Press.

De Vries, A., Biesheuvel, A., and Van Wijngaarden, L. (2002). Notes on the path and wake of a gas bubble rising in pure water. *J. Multiphase Flow.*, 28:1823–1835.

Ellingsen, K. and Risso, F. (2001). On the rise of an ellipsoidal bubble in water: oscillatory paths and liquid-induced velocity. *J. Fluid Mech.*, 440:235.

Figueroa-Espinoza, B., Zenit, R., and Legendre, D. (2008). The effect of confinement on the motion of a single clean bubble. *J. Fluid Mech.*, 616:419–443.

Hallez, J. and Legendre, D. (2011). Interaction between two spherical bubbles rising in a viscous liquid. *J. Fluid Mech.*, 673:406– 431.

Harlow, F. and Welch, J. (1965). Numerical calculation of time-dependent viscous incompressible flow of fluid with free surface. *Phys. Fluids*, 8:2182–2189.

Hestroni, G., Haber, S., and Wacholder, E. (1997). The flow fields in and around a droplet moving axially within a tube. *Phys. Fluids*, 9:44.

Jeong, H. and Hyungmin, P. (2015). Near-wall rising behaviour of a deformable bubbl at high reynolds number. *J. Fluid Mech.*, 771:564–594.

Joseph, G., Zenit, R., Hunt, L., and Rosenwinkel, M. (2001). Particule-wall collisions in a viscous fluid. *J. Fluid Mech.*, 433:329–346.

Klaseboer, E., Chevallier, J.-P., Mate, A., Masbernat, O., and Gourdon, C. (2001). Model and experiments of a drop impinging on an immersed wall. *Phys. Fluids.*, 13:45.

Kok, J. (1993). Dynamics of a pair of gas bubbles moving through liquid. part i. theory. *Eur. J. Mech. Fluids*, 12:515–540.

Krasowska, M. and Malysa, K. (2007). Wetting films in attachement of the colliding bubble. *Adv. Colloid Interface*, 138:134–135.

Legendre, D. (2007). On the relation between the drag and the vorticity produced on clean bubble. *Phys. Fluids*, 19:018102.

Legendre, D., Daniel, C., and Guiraud, P. (2005). study of a drop bouncing on a wall in a liquid. *Phys. Fluids*, 17:097105.

Legendre, D., Magnaudet, J., and Mougin, G. (2003). Hydrodynamic interactions between two spherical bubbles rising side by side in a viscous liquid. *J. Fluid Mech.*, 497:133166.

Legendre, D., Zenit, R., and Velez-Cordero, J. R. (2012). On the deformation of gas bubbles in liquids. *Phys. Fluids*, 24:043303.

Magnaudet, J. and Eames, I. (2000). The motion of high-reynolds-number bubbles in inhomogeneous flows. *Annu. Rev. Fluid Mech.*, 32:659–708.

Magnaudet, J., Rivero, M., and Fabre, J. (1995). Accelerated flows past a rigid sphere or a spherical bubble. part 1 : Steady straining flow. *J. Fluid Mech.*, 284:97–135.

Magnaudet, J., Takagi, S., and Legendre, D. (2003). Drag, deformation and lateral migration of a buoyant drop moving near a wall. *J. Fluids Mech.*, 476:115–117.

Maslyiah, J., Jauhari, R., and Gray, M. (1994). Drag coefficient for air bubbles rising along an inclined surface. *Chemical Engineering Science*, 49:1905–1911.

Maxworthy, T., Gnann, C., Kürten, M., and Durst, F. (1996). Experiments on the rise of air bubbles in clean viscous liquids. *J. Fluid Mech.*, 19:18.

Milne-Thomson, L. (1968). *Theoretical Hydrodynamics*. MacMillan.

Moctezuma, M., Lima-Ochoterena, R., and Zenit, R. (2005). Velocity fluctuations resulting from the interaction of a bubble with a vertical wall. *Phys. Fluids*, 17:098106.

Moore, D. (1965). The velocity of rise of distorted gas bubbles in a liquid of small viscosity. *J. Fluid Mech.*, 23:749–766.

Norman, C. and Miksis, M. (2005). Dynamics of a gas bubble rising in an inclined channel at finite reynolds number. *Phys. Fluids*, 17:022102.

Pelletier, E., Béguin, C., and Étienne, S. (2015). Experiments of air bubbles impacting a rigid wall in tap water. *Phys. Fluids.*, 27:123302.

Podvin, B., Khoja, S., Moraga, F., and Attinger, D. (2008). Model and experimental visualizations of the interaction of a bubble with an inclined wall. *Chem. Eng. Sc.*, 63:1914–1928.

Rivero, M. (1991). *Etude par simulation numérique des forces exercées sur une inclusion sphérique par un écoulement accéléré.* PhD thesis, Institut National Polytechnique de Toulouse.

Schiller, L. and Naumann, A. Z. (1933). A drag coefficient correlation. *J. Fluid Mech.*, 23:749.

Sussman, M., Smereka, P., and Osher, S. (1994). A level set approach for computing solutions in incompressible two-phase flow. *J. Comput. Phys.*, 114:146159.

Takemura, F. and Magnaudet, J. (2003). The transverse force on clean and contaminated bubbles rising near a vertical wall at moderate reynolds number. *J. Fluid Mech.*, 495:235–253.

Tsao, H. and Koch, D. (1994). Collisions of slightly deformable, high reynolds number bubbles with short-range repulsive forces. *Phys. Fluids*, 6:2591.

Tsao, H. and Koch, D. (1997). Observation of high reynolds number bubbles interacting with a rigid wall. *J. Fluid Mech.*, 41:689–705.

Vasseur, P. and Cox, R. G. (1977). The lateral migration of spherical particles sedimenting in a stagnant bounded fluid. *J. Fluid Mech.*, 80:561–591.

Zawala, J., Krasowska, M., Dabros, T., and Malysa, K. (2007). Influence of bubble kinetic energy on its bouncing during collisions with various interfaces. *Can. J. Chem. Eng.*, 5(85):669.

Zenit, R. and Legendre, D. (2009). The coefficient of restitution for air bubbles colliding against solid walls in viscous liquids. *Phys. Fluids*, 8(21):083306.

Zenit, R. and Magnaudet, J. (2008). Path instability of rising spheroidal air bubbles: A shape-controlled process. *Phys. Fluids.*, 20:061702.